ALMA MATER STUDIORUM
UNIVERSITÀ DEGLI STUDI DI BOLOGNA

SCUOLA DI SCIENZE
Dipartimento di Fisica e Astronomia
Corso di Laurea Magistrale in Astrofisica e Cosmologia

Tesi di Laurea Magistrale

On the dust and gas content of high-redshift galaxies hosting obscured AGN in the CDF–S

Presentata da:
Quirino D'Amato

Relatore:
Chiar.mo Prof.
Cristian Vignali

Co–relatori:
Dott. Roberto Gilli
Dott. Marcella Massardi

Sessione II
Anno Accademico 2017-2018

Abstract

Submillimeter Galaxies (SMGs) at high redshift are among the best targets to investigate the early evolutionary phases in the lifetime of massive systems, in which a central Super Massive Black Hole (SMBH) is heavily obscured and the total emission is dominated by the host galaxy light. How such structures form and evolve is still a debated issue; different paradigms have been proposed to describe the co–evolution between the Active Galactic Nuclei (AGN) and their host galaxies, and investigate the role of AGN and stellar feedback in regulating the Star Formation Rate (SFR) and BH accretion. The early stages of such evolution are characterized by the presence of large gas and dust reservoirs that sustain (and obscure) a starburst phase during which galaxies behave as bright SMGs, hosting hidden Quasi–Stellar Objects (QSOs).

The main purpose of this work is to investigate the contribution of the Inter–Stellar Medium (ISM) to the obscuration of QSOs in distant SMGs, and unveil the morphological and kinematics properties of these objects. The analysis is based on new ALMA band 4 (1.8–2.4 mm) data of six galaxies at redshift > 2.5 in the Chandra Deep Field South (CDF–S). These objects are included in the 7–Ms Chandra exposure which allows an accurate determination of their nuclear properties; they have been selected by their high column density ($\log N_H > 23$), secure spectroscopic redshift and good far–infrared data coverage, resulting in a unique sample with such characteristics. Through the detection of their continuum (i.e., dust–reprocessed) emission at ~ 2.1 mm and of one high–J CO transition per source, we aim at measuring the luminosity and size of dust and molecular gas of these objects to derive their masses and (under simple geometrical assumptions) the ISM column densities.

We found that these galaxies are massive ($M_{H_2} \gtrsim 10^{10}\ M_\odot$) and compact (diameter lower than 3 kpc) systems and that the column densities associated with the ISM are of the order of 10^{23-24} cm^{-2} for all the assumed geometries. This suggests that the galaxy ISM can substantially contribute to the AGN obscuration. In addition, we found that one of the sources presents unambiguous features of a rotating system, and another one can probably be described by the same morphological structure. We also found indications that a third source is possibly undergoing a merger.

This thesis work is structured as follows:

- In Chapter 1 we initially provide a brief description of the astronomical objects that are the subjects of this work and we illustrate the scientific context and justification behind it. We define our scientific objectives and the methodologies used to achieve them. We describe the criteria adopted to select the targets and their main emission and physical properties collected in the available literature.
- In Chapter 2 we describe the targets of our analysis and the data reduction process, including the ALMA pipeline calibration and visibility inspection.
- In Chapter 3 we perform imaging of both continuum and line emission; we also perform image, spectrum and visibility fitting in order to obtain the required observable and physical quantities such as flux density, size and line shape.
- In Chapter 4 we use the values obtained in the previous chapter to derive the mass and size of both dust and molecular gas of the sources, as their column densities for different geometrical models, and compare them with those measured from the X–ray spectrum.
- In Chapter 5 we summarize and discuss the results and future perspectives.

Sommario

Le Galassie sub–millimetriche (SMGs) ad alto redshift sono una classe di oggetti molto importante per investigare le proprietà dei sistemi massivi nelle prime fasi della loro evoluzione, in cui si trova un Buco Nero Supermassivo (SMBH) fortemente oscurato e l'emissione totale è dominata dalla galassia ospite. La formazione ed evoluzione di queste strutture è ancora una questione aperta; nel tempo sono stati proposti diversi paradigmi per descrivere la co–evoluzione tra i Nuclei Galattici Attivi (AGN) e le loro galassie ospiti, investigando il ruolo che il feedback dell'AGN e della formazione stellare possono avere nel regolare il Tasso di Formazione Stellare (SFR) e l'accrescimento del BH centrale. Le prime fasi di questa evoluzione sono caratterizzate dalla presenza di una grande quantità di gas e polvere che sostengono (ed oscurano) una fase di starburst durante la quale le sorgenti appaiono come SMGs, all'interno delle quali è nascosto un Quasar.

Lo scopo principale di questo lavoro è di valutare il contributo del Mezzo Interstellare (ISM) all'oscuramento del Quasar in SMGs distanti, e di caratterizzare le loro proprietà cinematiche e morfologiche. L'analisi riguarda nuovi dati raccolti da ALMA in banda 4 (1.4–2.8 mm) su sei galassie a redshift > 2.5 nel Chandra Deep Field South (CDF–S). Questi oggetti sono inclusi nella mappa di 7–Ms di tempo di esposizione di Chandra, cosa che permette un'accurata determinazione delle proprietà del nucleo. Queste sorgenti sono state selezionate per la loro alta densità di colonna ($\log N_H > 23$), redshift spettroscopico sicuro e buona copertura nella banda infrarossa; risulta quindi un campione unico con queste caratteristiche. Attraverso la detezione della loro emissione nel continuo (ovvero, luce riprocessata da polvere) a $\sim$2.1 mm e di una riga di alta eccitazione del CO per ogni sorgente, miriamo a misurare la luminosità e la dimensione sia della componente di polvere sia della componente di gas, in modo da ricavare (in base a semplici assunzioni geometriche) la densità di colonna dell'ISM.

Uno dei risultati conseguiti in questo lavoro di tesi è stato trovare che questi oggetti sono sistemi massivi ($M_{H_2} \gtrsim 10^{10}\ M_\odot$) e compatti (diametro minore di 3 kpc) e che la loro densità di colonna è dell'ordine di 10^{23-24} cm^{-2} indipendentemente dalle assunzioni geometriche utilizzate. Questo risultato suggerisce che l'ISM della galassia ospite può significativamente contribuire all'oscuramento dell'AGN. Inoltre, abbiamo trovato che una di queste sorgenti presenta chiare indicazioni di una struttura rotante, mentre un'altra può

essere probabilmente descritta da una morfologia simile. Una terza sorgente ha delle caratteristiche che suggeriscono la possibilà che stia attraversando una fase di merger.

Questa tesi è strutturata nel seguente modo:

- Nel Capitolo 1 descriviamo brevemente gli oggetti astronomici soggetti di questo lavoro, illustrandone il contesto e le problematiche scientifiche. Determiniamo gli obiettivi del lavoro e le metodologie adoperate per raggiungerli. Descriviamo inoltre i criteri adottati per selezionare le sorgenti e le loro principali proprietà in termini di emissione e caratteristiche fisiche, sulla base della letteratura disponibile.
- Nel Capitolo 2 descriviamo le sorgenti della nostra analisi e la riduzione dei dati, compresa la pipeline di ALMA e l'ispezione delle visibilità.
- Nel Capitolo 3 eseguiamo l'imaging del continuo e delle righe di emissione, per poi fittare le immagini, le visibilità e gli spettri in modo da ottenere le quantità necessarie all'analisi, come la densità di flusso, le dimensioni angolari e la forma spettrale.
- Nel Capitolo 4 usiamo i valori ricavati nel capitolo precedente per ottenere le masse e le dimensioni sia della polvere che del gas, in modo da derivare le densità di colonna (sotto determinate assunzioni geometriche) e compararle con quelle ricavate dagli spettri X.
- Nel Capitolo 5 riassumiamo e discutiamo i risultati ottenuti e le prospettive future.

Contents

Chapter 1

Introduction

1.1 Active Galactic Nuclei

Active Galactic Nuclei (AGN) are among the most powerful and complex systems in the universe. They can produce a huge amount of energy generated in the inner compact region constituted by various components that play different roles in the galaxy physics, evolution and feedback. Their activity is characterized by accretion onto Super Massive Black Holes (SMBH) in the galaxy center that powers their emission over twenty decades in frequency. This emission is too intense to be ascribed only to the processes of stellar, gas and dust components. Other AGN features are the presence of emission lines from high excitation levels in their spectra, and time variability.

Such powerful nuclear activity is observed in approximately 1% – 10% of all galaxies. AGN emission may be not dominant in the bolometric luminosity, but their emission can be prevalent at specific wavelengths, showing different features depending on the spectral band in which they are observed (§ 1.1.3). During the past decades this variety led to the classification of these objects in a wide series of classes, based on the intensity in a given band, selection criteria, morphology or line characteristics.

1.1.1 Main AGN components

The AGN structure is made by several components, mostly concentrated within a region of few tens of parsec scale that cannot be probed directly because of current observational limits. Thus, there is not an unique model that perfectly describe the central engine and BH feeding in all its physical and observational aspects. However, the most widely accepted paradigm predicts at least the presence of the following components:

– **SMBH**: it is the central engine on which the matter falls from the surrounding accretion disk. Its mass typically ranges from 10^6 and $10^9 M_\odot$

concentrated within a region defined by the Gravitational radius r_g which is directly proportional to the BH mass M_{BH}: $r_g = GM_{BH}/c^2$ where G is the Gravitational constant and c is the speed of light. The other two quantities that characterize the BH are the charge (usually set equal to zero) and the angular momentum J given by the adimensional parameter spin $a = Jc/GM_{BH}^2$. The accretion onto the BH converts the gravitational energy into radiation heating the material in a dissipative accretion disk. From the equilibrium between the gravitational and radiation force it is possible to define a limit of the luminosity above which the radiation pressure overwhelms gravity, called Eddington luminosity: $L_{Edd} \simeq 1.5 \times 10^{38}(M_{BH}/M_\odot)$ erg s^{-1}, corresponding to the Eddington accretion rate $\dot{M}_{Edd} = L_{Edd}/\eta c^2$, where η is the efficiency of energy conversion, usually of the order of $\sim$10% (it also depends on the spin of the BH).

– **Accretion disk**: it forms in the nearest regions of the BH and consists in rotating material around the central BH engine under its gravitational influence at distances of 10^{-6} pc $\leq r \leq 10^{-3}$ pc. Angular momentum dissipates through gas viscosity, converting the lost energy into electromagnetic radiation. The disk can be either optically thin or thick, depending on the gas density, ionization level and accretion rate. The most commonly assumed model consists of optically thick (geometrically thin) objects with a high efficiency in converting the potential energy of the gas accreted onto the SMBH (Shakura and Sunyaev, 1973); in this case the disk can be approximated with a series of concentric rings with density and temperatures rising from the outer to the inner regions. Each ring emits as a Black Body at its own temperature. The resulting emission is a power law $S_\nu \propto \nu^{1/3}$, responsible for the most of emission in the UV and soft X–ray band. Another optically thick accretion disk model predicts that the disk reaches a distance from the central BH larger than that reached by the thin disk and results in a poorly efficient, less luminous accretion process, due to the creation of a highly–ionized, optically thin gas region between the disk and the AGN (advection–dominated accretion flow, ADAF Ichimaru, 1977). The dominance of one or the other disk type is probably related to the presence or absence of the jets of the AGN.

– **Hot corona**: it is thought to be a very hot ($T \sim 10^{8-9}$ K), dense $n \sim 10^8$ cm^{-3}) and highly ionized gas region extended from a few to $\sim$10 gravitational radii around the accretion disk (Fabian et al., 2015). Its formation mechanism is still unknown, and different scenarios have been proposed: it may result from strong vertical gradient of the density of the disk that causes the expansion of its outer layers (Netzer, 2013) or from instabilities in weakly magnetize accretion flows

(Di Matteo et al., 2000). One of the open issues about the hot corona is its geometry: the simplest model predicts an optically thin corona distributed above the disk, heated by the accretion power, probably with a clumpy structure.

– **Broad Line Region (BLR)**: characterized by the emission of permitted lines with a Doppler broadened Full Width Half Maximum (FWHM) of $\Delta v = 10^{3-4}$ km/s (Peterson, 1997), this region is composed by warm ($T \sim 10^4$ K), extremely dense ($n \sim 10^{9-10}$ cm^{-3}) clouds located adjacent (0.1 – 1 pc) to the central engine. Given the high temperature in this region the dust cannot co–exist with the gas due to the sublimation.

– **Narrow Line Region (NLR)**: it is the largest scale structure (few hundreds of parsecs) in which the radiation from the innermost region can still ionize and excite the medium. It is defined by the narrow FHWM of the line originated in its medium ($\sim \Delta v = 10^2$ km/s) and is composed by gas with lower density ($n \sim 10^4$ cm^{-3}) than the BLR, which allows forbidden transition to happen. Since the ionizing radiation comes from the center with anisotropic direction (due to the torus geometry), the NLR often presents an axisymmetrical double opposite cones distribution with respect to the central nucleus (Peterson, 1997). The lower temperature with respect to BLR allows the dust to co–exist with the gas.

– **Torus**: this region starts in proximity of the accretion disk (may be the continuation of it) that extends to few tens of parsec outwards. It contains atomic and molecular gas ($n \sim 10^{4-7}$ cm^{-3}) rotating at velocity of $\sim 10^3$ km/s) and dust, approximately distributed in large, almost round, structure. One of the most debated issue about torus is its internal spatial distribution; the simplest models depict a torus smoothly filled in all its volume, in which the dust temperature is a function of the distance from the galactic center (Pier and Krolik, 1992, 1993). In the last years, due to studies on time variability (Risaliti, 2008), SED fitting (Haas, 2003) and high resolution mid–infrared observations (e.g. Burtscher et al., 2013), a more complex modeling of the torus has been arising, describing a clumpy structure in which the matter is distributed in clouds of variable size. Torus plays a major role in the obscuration of the central engine, in particular in the optical and X–ray bands, whose reprocessed light is thermally re–emitted in the infrared (IR) band (peaks at ∼10–20 μm for a typical torus temperature of 400 K, § 1.1.3). The torus obscuration is considered to be responsible of the Type I/Type II dichotomy in the Unified Model frame, explained in terms of inclination angle with respect to the line of sigh (§ 1.1.2). In case the torus structure is clumpy, the probability

to observe an obscured source increases with the inclination angle but it is still finite, since the light has always the chance to escape between the clouds. The formation mechanism of the torus is still unknown: it may result from outflowing materials from the inner accretion disk (Gallagher et al., 2013) or from the inflows of gas provided by exploding stars from nuclear clusters (Schartmann et al., 2009).

– **Jets**: they are the largest structures directly associated to AGN activity. They originate in the very inner region of the nucleus and extend up to host galaxy (the weakest ones) or even Mpc (the strongest ones) scale. Its (still unclear) formation mechanism is probably related to the intense magnetic activity in the innermost regions that accelerates and pushes away the gas (magnetic tower model, Lynden–Bell's, 1996). The jets are composed by relativistic particles that mostly emit through synchrotron emission peaking in radio–band, and eventually re–emit trough Inverse–Compton (IC) emssion up to γ–rays. The jets interact with the host galaxy inter–stellar medium (ISM) creating sites of intense emission called hot spots, which correspond to the shocks fronts at the end of the jets. In the wake of the hot spots, regions of strong radio emission (called lobes) form. Radio lobes radiation (due to synchrotron) usually dominates the luminosity of the AGN at radio wavelengths.

1.1.2 The AGN family

Historically, AGN have been classified in a large number of classes according to their properties in the different bands of the spectrum. In fact, this classification is only partially related to physical differences of the AGN, as it mainly results from the method by which they have been selected. However, a dual classification arose in the past decades leading to the standard Unified Model (Antonucci, 1993), which divides AGN in two main categories, named Type I and Type II, and postulates that the observed differences between them are due to orientation effects with respect to the line of sight. The key role in this classification is played by the obscuring medium, which is believed to be adssociated with the torus. However, in the last few years a new scenario has arisen from many results showing that a more complex modeling of the obscuring material distribution is required (Bianchi et al., 2012). In particular, the physical properties of the heavily obscured objects at high redshift remain unconstrained, questioning whether (and to what extent) the Unified Model succeeds in describing the AGN population to the early stages of their evolution, or the obscuration can be considered as a result of an evolutionary process (§ 1.1.4).

In the following we report the main AGN classes, while in Figure 1.1 we show a schematic view of the Unified Model.

– **Radio galaxies**: The first classification of AGN is based on the so–called radio–loudness, parameter defined as the ratio between the radio and another band (typically optical) flux (e.g., $F_{5\mathrm{GHz}}/F_B > 10$ Kellermann et al., 1989). This classification results in the subdivision into the Radio–Loud (RL) (typically the 10% of the population) and Radio–Quiet (RQ) (the remaining 90%) categories. Padovani et al. (2017) suggest that since the major physical difference between these objects is the presence of strong relativistic jets, RL and RQ should be referred as "jetted" and "non–jetted" sources. Among RL a further subdivision based on the radio luminosity at 178 kHz is commonly applied: low–power RL have $L_{178kHz} < 10^{25} W/Hz$, while high–power RL have $L_{178kHz} > 10^{25} W/Hz$. These sources are respectively associated with the FR I and FR II classification (Fanaroff and Riley, 1974). In addition to the emission power, FR galaxies differ also in the morphology: FRIIs (also referred as jet–dominated) show the presence of strong relativistic jets that reach the maximum luminosity in the so–called hot spots. The emission of these jets is often affected by relativistic boosting, i.e. the jet which is coming towards the observer is much more luminous that that proceeding in the opposite direction (counter–jet). FRIs (named core–dominated) instead show fainter jets with irregular shape, absence of hot spots and a peak of luminosity in the inner region, suggesting a different intrinsic mechanism in jet formation and jet–ISM interaction with respect to FRIIs. In terms of the optical spectra and Type I/II frame, among RL galaxies we recognized two main classes, perfectly comparable to the Seyfert classification for the RQ: the Broad-line radio galaxies (BLRGs) and the Narrow-line radio galaxies (NLRGs).

– **Blazars**: These are the most powerful classes of objects, characterized by a double–peaked spectrum that extends from the radio to γ–rays band. These sources are identified as AGN whose jet points directly in the direction of the observer. A peculiar property of Blazars is the short time–scale variability (hours/days). Blazars are divided in two main sub–classes:: BL Lacs, with weak or absent broad emission lines, and Flat Spectrum Radio Quasars (FSRQ), with strong broad emission lines. The two sub–classes are thought to be intrinsically different objects and are associated with FRI (BL–Lac) and FRII (FSRQ) radio sources. One of the main evidences of this separation arises from the the correlation between optical and radio luminosity (Chiaberge et al., 2000) of the BL–Lac/FRI objects with respect to FSRQ/FRII, for which the emissions in these two bands do not correlate. This correlation for the BL–Lac is explained in terms of lack of a dusty component (i.e., the torus) which would absorb the optical emission. In addition, FSRQs and BL Lacs share the same γ–ray luminosity and this is ex-

plained by a intrinsic difference of the black hole masses (Ghisellini, 2016).

- **Seyfert galaxies**: based on an original classification made by Seyfert (1943), these objects are recognized by the presence of strong, high-ionization emission lines. According to the Type I/II dichotomy, these galaxies are divided in Seyfert 1, characterized by narrow and broad permitted emission lines in the optical spectrum, and Seyfert 2 which show narrow lines only. There are also sources classified as intermediate cases. In addition, the continuum of Seyfert 2 is more depressed with respect to Seyfert 1, especially at short wavelengths, due to the extinction by the circumnuclear medium (e.g, torus). Seyfert galaxies are lower-luminosity AGN with respect to Quasars, but they have the same physical engine. Historically, the separation between these two classes mainly involves the optical magnitude, despite a division value has never been properly defined.

- **Quasars (QSO)**: Initially they appeared as radio faint point-like objects with unusual optical emission spectra: hence the definition of Quasi-stellar radio sources (Hazard et al., 1963). QSO are referred to be the more luminous counterpart of Seyfert and share with them the Type I and Type II classification with analogous spectral features. However, the shape of the nonstellar continuum in the spectral energy distribution of QSO presents a steepening at high frequencies compared to Seyfert galaxies.

A particularly interesting sub–class of objects is made up by Luminous Infra–Red Galaxies (**LIRGs)**, characterized for having more energy in the infrared portion of the spectrum than in all other wavelengths combined. Their infrared luminosity is typically above 10^{11} $L_{\odot}$: if this exceed 10^{12} $L_{\odot}$ or 10^{13} $L_{\odot}$ they are classified as Ultra-LIRGs (ULIRGs) or as Hyper-LIRGs (HyLIRGs) respectively. These objects are particularly gas and dust–rich galaxies in a starburst phase (star formation rate, SFR, up to 1000 $M_{\odot}$/yr), in which the material absorbs a significant amount of the light from stars and re-emits it in the infrared. From optical observation it results that most of these objects turned out to be merging or interacting galaxies, suggesting that the reason of their high SFR (and related infrared luminosity) was that the merger of two gas–rich spiral galaxies had induced it and, in many cases, drove gas toward the SMBH, activating the central engine. In this frame, the obscuration is no longer explained by the Unified Model in terms of inclination angle, but rather it is the result of an evolutionary stage of the galaxy. Most of their observations are limited to $z \lesssim 1$ (Padovani et al., 2017). Their possible high–redshift counterpart are the Sub–millimetre Galaxies, which share with them many properties and that we illustrate in Section 1.2.

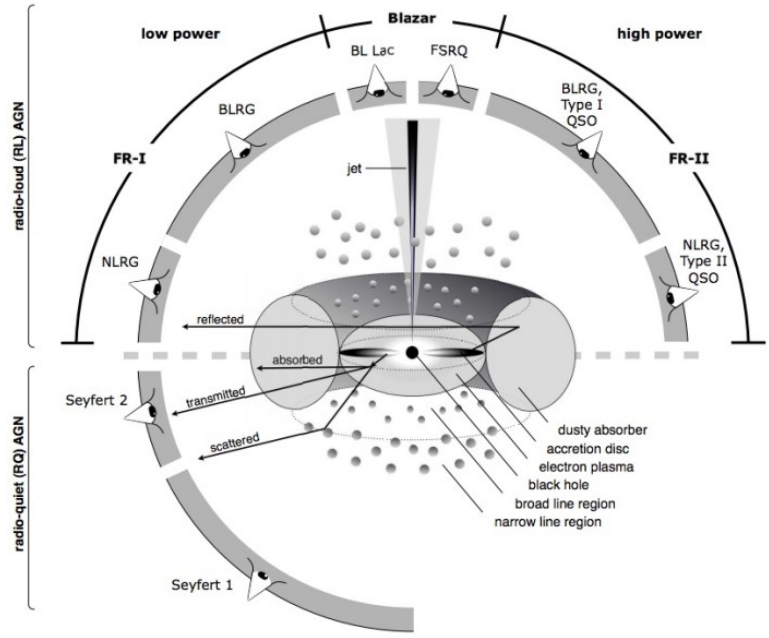

Figure 1.1: Schematic representation of the Unified Model. The various types of AGN can be understood as the result of different orientation angles with respect to the line of sight, as well as intrinsic differences between high–power Radio Loud, low–power Radio Loud and Radio Quiet. The principal components of the AGN are also indicated. Image adapted from Beckmann and Shrader (2012).

1.1.3 Broad–band properties of AGN

The emission of AGN spreads all over the frequency spectrum from the radio to the γ–rays. Its shape can differ significantly depending on intrinsic source characteristics and orientation that affect the column density and thus the obscuration. A schematic of the spectral energy distribution (SED) is reported in Figure 1.2, showing the total emission of non–jetted (with all its components), high synchrotron peaked jetted (HSP) and low synchrotron peaked (LSP) AGN.

In the following we report a brief description of the spectral properties in each band, focusing on the X-rays and IR emission that are particularly interesting for the purposes of this work.

– **Radio**: depending on whether the object is RL or RQ, these sources show a strong emission that extends from the infra–red to the radio band (RL) or rapidly decreases in the millimetre band (RQ). The emission is due to synchrotron from charged particles accelerated in a strong magnetic field, and it spatially extends from the inner region where the jet becomes optically thin to the jet lobes where the particles interact with the galaxy components. Often in jetted sources the radio emission

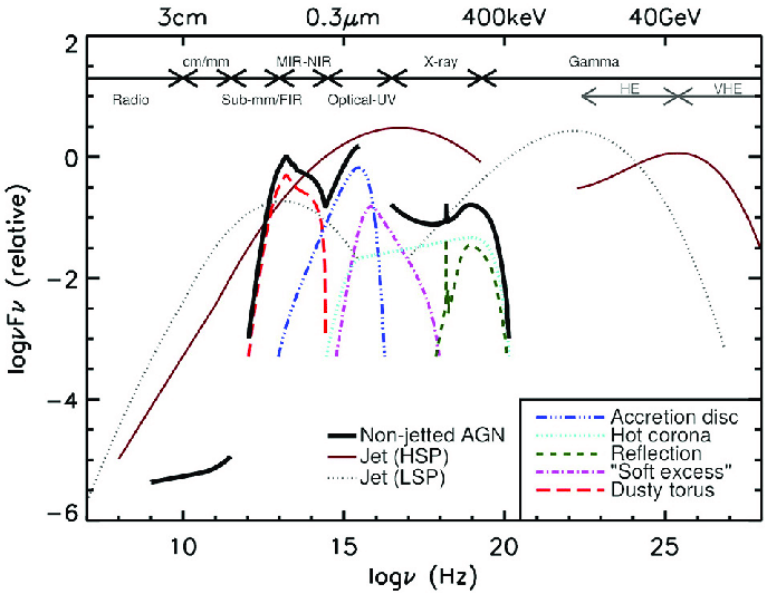

Figure 1.2: A schematic view of the spectral energy distribution (SED) of an AGN, showing the emission of the various components reported in the text (corresponding to the colored dashed and dash–dotted curves). The black solid curve represents the total emission. The jet SED is also shown for a high synchrotron peaked blazar (HSP) and a low synchrotron peaked blazar (LSP). From Padovani et al. (2017), adapted from Harrison (2014).

overwhelms that at higher frequencies.

– **Optical and UV**: it is principally ascribed to the thermal emission of the disk and is the main responsible for the Big Blue Bump (BBB) and the Soft Excess features in the total AGN SED. In non–jetted Type I sources, the BBB represents the brightest feature all over the frequency, while in Type II the reprocessed mid–IR light becomes prominent. The optical spectrum is characterized by the presence of emission lines whose width depends on whether the BLR is visible (Type I) or not (Type II), making this band the classical one to estimate the source redshift.

– **γ–rays**: the emission mechanisms dominating in this band are synchrotron and Self Synchrotron Compton (SSC). The photons produced via synchrotron by the charged particles move them via IC to higher energy at which they re–emit photons. Blazars emission is featured by a "double–peak": the peak at lower energy is due to the synchrotron, whereas the peak at higher energy to the SSC. In BL–lac sources the peaks are comparable and shifted to higher energy (high synchrotron peaked blazar, HSP) with respect to FSRQ (low synchrotron peaked blazar, LSP), in which the SSC peak is more prominent with respect

to the synchrotron peak. This is due to IC effect that becomes more efficient at lower frequencies.

X–rays

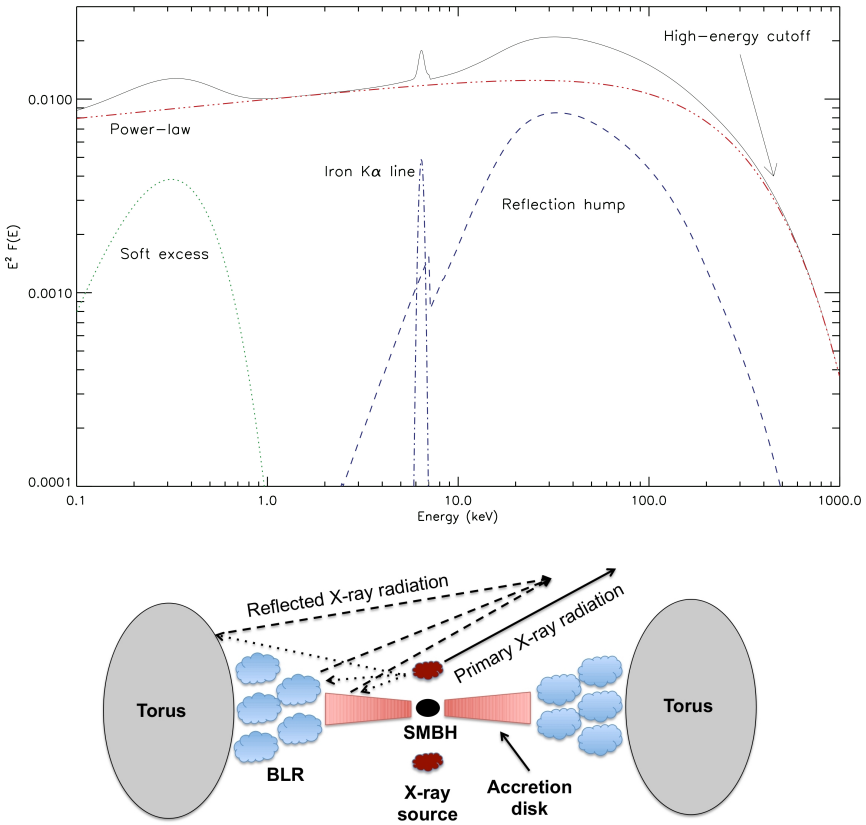

Figure 1.3: Total X-rays spectrum of a AGN (top panel) and a cartoon showing the various emitting region of the different spectrum components (bottom panel, not in scale). In the spectrum the components are indicate as follow: primary emission power–law (red dash–dotted line), soft excess (green dotted line), iron Kα (blue dash–dotted line), reflection hump (blue dashed line) and total emission (black solid line). Image taken from http://www.isdc.unige.ch/~ricci/Website/AGN_in_the_X-ray_band.html.

X–ray band is fundamental to probe the innermost regions of the central engine. A schematic view of the X–ray spectrum components and the corresponding emitting regions is shown in Figure 1.3.

The primary direct emission is believed to be produced by thermal Comptonization of the optical/UV disk photons by the electrons of the hot corona, and the energy photon distribution is well described by a power–law $N(E) = N_0 E^{-\Gamma}$, where Γ is the photon index usually comprised between 1.8 and 2.0.

This feature is directly related to the physical conditions of the hot plasma of electrons and can be used to derive its properties such as temperature and optical depth. The second (fainter) direct emission which affects the soft range (0.2 – 2 keV) of the X–ray band is the so–called soft excess, possibly ascribed to the higher energy component of the thermal emission from the accretion disk.

The X–ray band is also strongly affected by an indirect emission component (called reflection) thought to be originated by the reprocessing of the primary emission by the disk and molecular torus. Half of the photons from the hot corona is directed back to the disk and reprocessed by the medium. This component peaks around ∼20–30 keV and is characterized by a low energy (∼4–5 keV) and a high–energy (∼200 keV) cutoff. The former results from photoelectric absorption of the lower energy incident radiation, whereas the latter is due to the reduction of the cross–section of the gas that allows the photons to penetrate through it. The resulting shape of this component is the so–called reflection hump. Another important feature arising from the primary emission reprocessing is the iron Kα line at the rest–frame energy of 6.4 keV. This emission line occurs from the fluorescence effect when one electron of the K–shell ($n = 1$) of an iron atom is ejected due to photoelectric absorption of photons from the hot corona. The iron line emission is prominent with respect to the other metals because of its the higher relative abundance, higher equivalent width and because the probability of the fluorescence is higher than Auger de–excitation. The energy threshold for the absorption is 7.1 keV, that produces a drop of the reflection component called absorption edge. The ionization degree of the iron atoms affects the energy of both the line and the edge shifting them to higher energies, since the lower number of electrons is less able to screen the K–shell electrons from the nuclear charge. If the emitting region belongs to the inner part of the disk, the iron Kα shape may be affected by Doppler effect, relativistic Doppler boosting and gravitational red–shift, making this feature crucial to investigate the physical properties and size–scales of the innermost part of an AGN. The iron Kα line is often observed as the superposition of two components: while the first (broad) component described above arises from the reflection by the inner part of the accretion disk, the second (narrow) component is likely produced by material located further away, i.e. the BLR or torus (e.g. Risaliti and Elvis, 2004).

The obscuration affects the X–ray band by the metals photoelectric absorption which dominates at low energies (<10 keV, depending on the column density) and Compton scattering at higher energy (>10 keV). The obscuration determines to which extent the direct emission can escape through the medium and is a function of both column density N_H and metallicity: the more they increase the more the photoelectric absorption reduces the amount of the direct light that reaches the observer, making the reflected component

the only one that is observed. At higher energy multiple Compton scattering occurs lowering the photons energy until the metals can absorb them via photoelectric effect. Thus, as N_H increases the spectrum is absorbed towards higher and higher energies. The X–ray spectra of AGN with different levels of obscuration are reported in Figure 1.4.

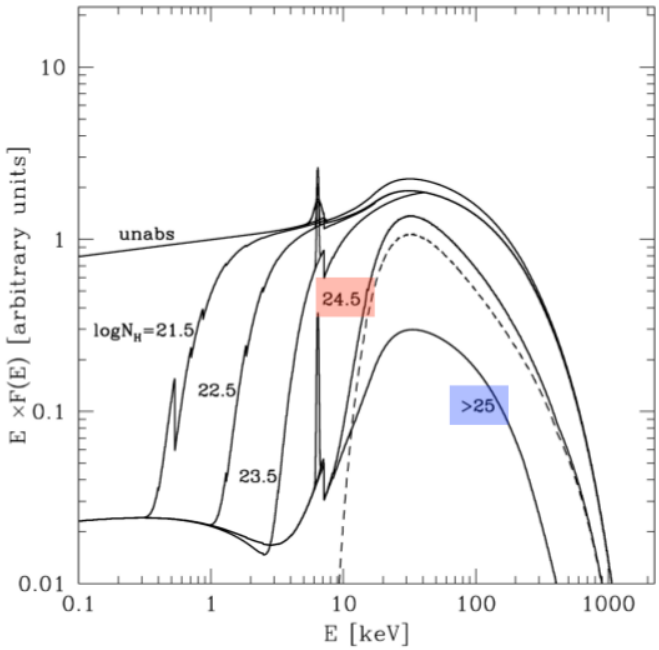

Figure 1.4: X-rays spectra of AGN with different levels of obscuration increasing from top to bottom. The dashed line indicates the transmitted component of the emission with $\log N_H = 24.5$. From Gilli et al. (2007).

According to the measured column density, the obscuration of the AGN can be generally classified as follows:

- **Unabsorbed**: $\log N_H < 21$;
- **Compton thin**: $21 < \log N_H < 24$;
- **Mildly Compton thick**: $\log N_H \sim 24 - 25$;
- **Heavily Compton thick**: $\log N_H > 25$.

A prominent signature of obscuration in the X–ray spectrum is the iron Kα line Equivalent Width (EW), defined as the line intensity against the (absorbed) continuum emission, that increases as a function of column density. Indeed, since the narrow iron Kα line component is generated by reflection of cold gas distributed in regions far from the central engine, it is unaffected by obscuration.

Infrared

Studies on the IR band had a fundamental role in understanding the AGN structure and evolution. Systems hosting AGN and nuclear starburst activity buried in a dusty environment are especially challenging to study, since the complexity in distinguishing the stellar versus accretion–related activity. A realistic modeling of these sources should include at least three components:

- **Stellar populations**: The single stars in distant galaxies are not resolved, thus the stellar emission is often treated as a superimposition of model populations which have the same age and different metallicity and mass, called Simple Stellar Populations (SSPs). One of the main uncertainty to this modeling comes from the assumption on the initial mass function (IMF), which describes the distribution in mass of a stellar population. The simplest modeling of a star population concerns the presence of at least two components: one consisting of old and less massive stars emitting mainly in the IR–optical band and one of young more massive and luminous stars that are predominant in the UV-optical range, especially if the galaxy is in a starburst phase. However, in a dusty environment the UV emission from the young massive stars is absorbed (and reprocessed) by the Interstellar Medium (ISM) and the only surviving direct star–light component comes from the older populations. Usually this component dominates the Near–IR emission peaking at $\sim$1.6 μm, where the AGN has a local minimum between the dropping accretion disk contribution and the rising of dust emission.

- **AGN**: The IR radiation range of the AGN is dominated by the dusty torus, picking at $\sim$10–20 μm, that reprocesses the UV–optical emission of the accretion disk into the IR band. Such a paradigm has been quite successful in describing the emission of a large variety of AGN, both Type I and Type II. However, there is a significant debate whether the dust is smoothly distributed in the torus or formed by optically and geometrically clouds (i.e., clumpy) as suggested by ground–based interferometric observation in the Mid–IR band (Jaffe et al., 2004; Burtscher et al., 2013). Furthermore, a more complex modeling predicts that the real distribution could be a combination of the two (Stalevski et al., 2012). For what concerns the IR SED description, the main difference between the two models rises in characterizing the temperature of the dust: in a simple smooth distribution the temperature is just a function of the distance from the central engine, whereas in the clumpy model we can find clouds at very different temperatures at the same distance from the center, since their heating depends on whether they are directly illuminated or not. Moreover, in the smooth model the torus obscuration is simply a function of the inclination angle, whereas in a clumpy distribution the column density depends on the amounts

and size of clouds that the light encounters along the line of sight. Finally, the torus emission could be not the only AGN component that affects the IR band: a significant contribution can also come from the scattered and direct light of the AGN, as shown by Ciesla et al. (2015) (Figure 1.5), which may differ between Type I and Type II objects.

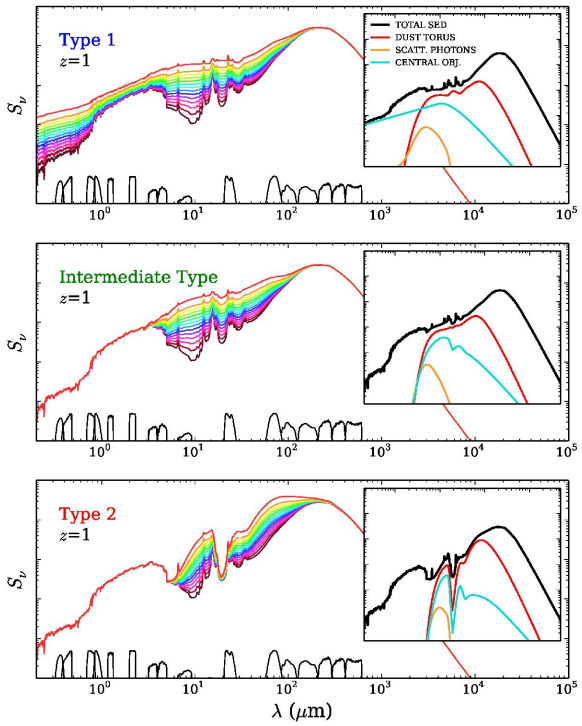

Figure 1.5: SEDs generated by CIGALE (a fast galaxy SED-fitting model) using a particular star formation history (SFH) extracted from GALFORM (a semi-analytic model to calculate the formation and evolution of galaxies) and added to different AGN templates with different normalizations relative to the galaxy light, at observerd z=1 frame. The three panels correspond (from top to bottom) to Type I, intermediate and Type II objects. The SEDs of each panel are coulored according to the contribution of the AGN to the total IR luminosity, while the black solid lines at the bottom are the transmission curves of UV to far–IR filters of current instrumentaition. In each panel the box on the right reports the contribution to the SEDs of the different components. Image taken from Ciesla et al. (2015).

– **Host galaxy ISM**: The ISM constitutes ∼10% of the total mass of the galaxy and is composed of (atomic and molecular) gas and dust particles. The gas component makes up most of the ISM, mainly composed by atomic and molecular hydrogen. The atomic gas absorbs the radiation in the UV range (thus becoming more and more important in active star–forming galaxies) and re–emits light into strong emission lines. The molecular component, due to the low filling factor in the galaxies volume, has a contribution to the bolometric luminosity

usually negligible in normal galaxies. However, in particularly dense and obscured objects, its reprocessed emission by the stellar radiation significantly increases, mostly in the near–IR band. Among all the molecules, the carbon oxide CO is particularly noticeable. It is the most abundant molecule after H_2, but unlike this one the CO is diatomic making dipole transitions allowed. In addition its high dissociation energy of 11.1 eV makes this molecule quite stable even in heated environments. Owing to these characteristics the CO molecule is the best tracer of molecular gas and its principal transition is the CO(1→0) at 115.27 GHz (∼2.6 mm). However the critical density of CO(1→0) is $\sim 10^3$ cm^{-3}, thus for denser objects higher transition are required for the observations.

Despite the dust component represents only a small fraction of the ISM its reprocessed thermal emission dominates the far–IR SED of many AGN in which a significant star formation is ongoing. It plays a major role in the extinction of the UV–optical light through scattering and absorption of the light, characterized respectively by the adimensional efficiency coefficients $Q_{sca} = \sigma_{sca}/(\pi a^2)$ and $Q_{abs} = \sigma_{abs}/(\pi a^2)$ where σ_{sca} and σ_{abs} are the cross–sections of the two processes and a is the size of the grain. A complete classical theory was independently developed by Mie (1908) and Debye (1909) for homogeneous sphere with isotropic refractive index, in which the total extinction efficiency $Q = Q(m, x)$ is a function of the refractive index m and the adimensional size $x = 2\pi a/\lambda$ which depends on the wavelength λ of the incident radiation. The refractive index can be expressed by the complex quantity $m = n + ik$ where n and k are the so–called optical constants. In the limit case of a dielectric material $k \approx 0$, as opposed to metals where $k \approx n$. If we consider the grain sizes much smaller than the incident wavelength ($a << \lambda$) the approximation $Q_{sca} \propto \lambda^{-4}$ (Rayleigh scattering) and $Q_{abs} \propto \lambda^{-1}$ yields for the extinction, described by the so–called extinction curve $k(\lambda)$ which affects the intrinsic flux $F_{0,\lambda}$ as

$$F_{obs,\lambda} = F_{0,\lambda} \cdot 10^{-0.4\ k(\lambda)\ E(B-V)}$$

where $E(B-V)$ is the color excess, defined as the difference between the observed and intrinsic color index $(B-V)$, that can be derived by the ratio of the emission line fluxes or SED fitting techniques. Figure 1.6 shows several extinction curves for different reddening laws.

The dust grain composition and size may considerably vary depending on the physical conditions of the environment. They are mainly composed by graphitic carbon grains, silicate grains and polycyclic aromatic hydrocarbons (PAHs), but also large complex structures, ices,

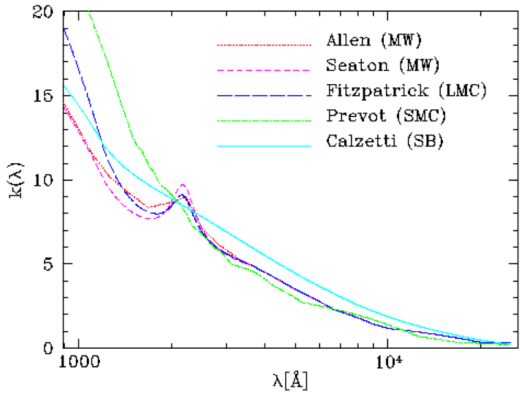

Figure 1.6: Extinction curve $k(\lambda)$ for different reddening laws: MW stands for Milky Way, LMC and SMC stands for Large and Small Magellanic Clouds, while SB refers to Starburst galaxies. It is clearly visible the bump feature at 2175 Å generated by the absorption of the graphite. (from Hyperz User's Manual, http://webast.ast.obs-mip.fr/hyperz/).

diamonds and organic molecules can be found. The grain size distribution is described by a power law following the theory developed by Mathis, Rumpl and Nordsieck (MNR) (Mathis et al., 1977):

$$\frac{\mathrm{d}n_a}{\mathrm{d}a} = A\ n_H\ a^{-3.5}$$

where n_a is the density of grains with size comprised between a and $a + \mathrm{d}a$ and A is a coefficient that describes the dust abundance in term of fraction of the hydrogen density n_H. Thus, MNR theory favorites the presence of small grains with respect to larger grain. Typically, the dust size is $0.005\ \mu\mathrm{m} < a < 0.25\ \mu\mathrm{m}$.

PAH molecules produce emission features in the mid–IR at specific wavelengths (mostly in the ∼3–13 μm wavelength range), as a result of the absorption of UV/optical photons which produce vibrational transitions, while silicate produce a strong absorption feature at 9.7 μm, called silicate–break. The radiation absorbed by the dust is thermally re–emitted in the far–IR, peaking at ∼100 μm. Assuming the local thermal equilibrium (LTE), the balance between heating and cooling of the dust grains can be written as the equilibrium between the absorbed and re–emitted flux:

$$\int S_{\nu,i}\ Q_{abs}(a,\nu)\ \mathrm{d}\nu = \int B_\nu(T)\ Q_{em}\ \mathrm{d}\nu$$

where $S_{\nu,i}$ is the incident flux density at a given frequency ν, $Q_{abs}(a,\nu)$ is the efficiency coefficient of absorption, $B_\nu(T)$ is the black body

Planck function and Q_{em} is the efficiency coefficient of emission. This coefficient is equal to 1 for a perfect black body and equal to 0 for a dielectric material. In the realistic case, the dust emission is modeled as a grey body and $Q_{em} = 1 - e^{-\tau}$, where τ is the optical depth which depends on the frequency: $\tau \propto \nu^{\beta}$, with β index value spanning between 1 for amorphic grains and ∼2 for metals and crystals. Thus, the dust flux density can be approximated by a grey body emission model written as $S_\nu \propto B_\nu(T_{dust})(1 - e^{-\tau})$. In Section 4.4 we will examine the optically thin regime in order to derive the dust mass from the continuum emission.

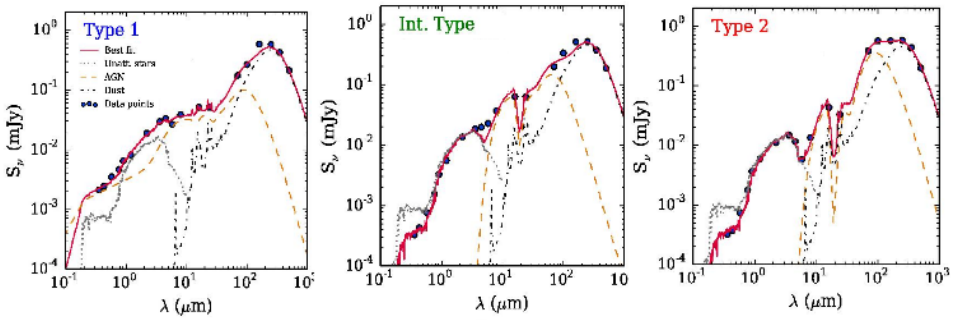

Figure 1.7: Examples of SEDs for mock galaxies associated with a given SFH. The three panels (from left to right) correspond to Type I, intermediate and Type II AGN, respectively. Blue points are the flux densities of the mock galaxies while the red lines are the best fits obtained by CIGALE. The three components that contribute to the SED are reported: the unattenuated stellar emission is indicated with black a dotted line, the dust emission as a black dashed-dotted line, and the total emission from the AGN as an orange dashed line. Adapted from an image of Ciesla et al. (2015).

In Figure 1.7 total IR SEDs for different AGN types are shown. Note that, on the other hand, for Type I objects the emission features in the mid–IR are more prominent with respect to the Type II, since they come from the inner hotter region. On the other hand the silicate–break and the other absorption features increase from Type I to Type II, since they depend on the column density, i.e. the obscuration.

1.1.4 AGN Evolution

One of the major issues in modern astronomy is galaxy evolution. Galaxies are complex systems and their structure significantly varies with morphology and composition, but almost all of them are thought to host a central SMBH which has passed (and possibly will pass) through active accretion phases during the galaxy life. Actually, there are increasingly evidences to support the paradigm of a strict co–evolution between the different component of the galaxies, connecting the properties of the largest structures to the innermost

regions activity. One of the most known relations firstly constructed for a sample of nearby sources by Magorrian et al. (1998) links the mass of the black hole to the stellar velocity dispersion (and thus the dynamical mass) of the bulge in early–type galaxies, suggesting a connection between the star formation history and the black hole accretion. Indeed, many studies (e.g. Gruppioni et al., 2011) have shown that the star formation rate and the accretion rate onto the black hole follow the same trend over the cosmic time, peaking at z∼2 (Figure 1.8).

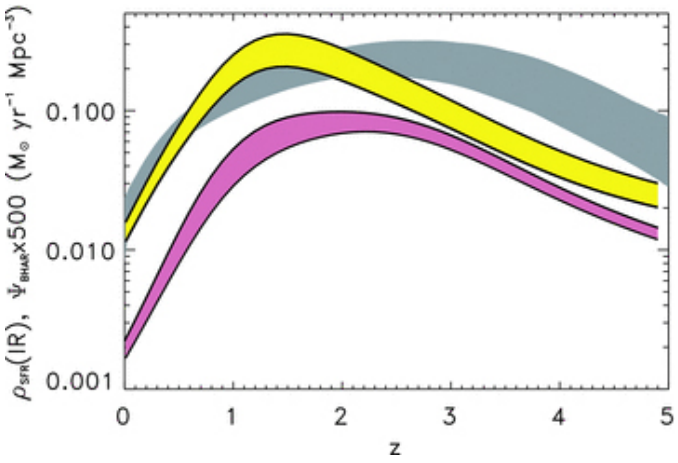

Figure 1.8: Star formation rate density (ρ_{SFR}, yellow–shaded area) and black hole accretion rate density ($\Phi_{BHAR} \times 500$, pink-shaded area) over cosmic time as estimated from IR SED fitting by Gruppioni et al. (2011). The gray shaded area corresponds to star formation rate density derived from optical/UV data by Hopkins and Beacom (2006).

Another interesting issue regarding AGN and galaxy evolution results from studying the luminosity and number density over cosmic time, which shows that the distribution of objects with lower BH accretion–related luminosity and star formation rate peaks at lower redshift, suggesting that the most of massive galaxies and BHs at their center formed earlier. This problem, referred as "downsizing", is in contrast with hierarchical formation of the structures and is one of the most debated issues in astronomy. In addition, these results require the SHBHs accreted the majority of their mass in a very short time–scale, implying a very efficient accretion mechanism onto a BH seed, the nature of which is still unclear.

Which are the physical interactions behind the co–evolution between the BH and its host galaxy is an open question. Likely, there is not only one process involved but rather different oneswhose individual contribution to the overall galaxy evolution may vary with system size, luminosity and cosmic epoch. Rosario et al. (2012) (Figure 1.9) have shown that luminosity of bright AGN ($L_X \gtrsim 10^{44}$ erg/s) correlates with the L_{IR} associated to the star–formation activity of their host. AGN with $L_X \lesssim 10^{44}$ erg/s, instead, do not show such a correlation, with SFR nearly constant at different L_X. This

discrepancy leads to the suggestion that different trigger mechanisms for the BH activity are involved: the higher luminosity AGN (10% of the population) are triggered by merger events that cause also a dramatically increase of the star formation, while the lower luminosity population is probably related to secular processes.

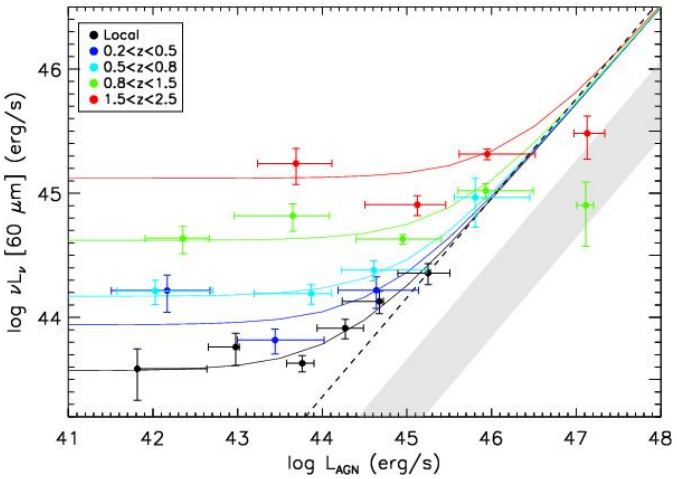

Figure 1.9: Mean νL_ν at 60 μm vs. bolometric L_{AGN} of X-ray selected AGN in 5 different redshift bins from the local Universe to z = 2.5, from Rosario et al. (2012). The colored data points are combinations of mean measurements in GOODS-N, GOODS-S and COSMOS, while the black data points come from the analysis of the SWIFT-BAT sample. The solid colored lines are the best fits for each bin. The dashed line is the correlation line shown by AGN-dominated systems in Netzer (2009), while the shaded region corresponds to the approximate 1σ range exhibited by empirical pure-AGN SEDs.

Despite these results seem to depict a scenario in which bright AGN are mainly triggered by different forms of galaxies interaction, it is still unclear if this is the major mechanism especially at high redshift. Vito et al. (2018) have shown how the fraction of obscured AGN is constant with the luminosity at z$\gtrsim$3, in contrast with the local universe where the obscured fraction decreases with the luminosity of the AGN. Moreover, the obscured fraction at high redshift is higher than that at low redshift. This suggests that in the earlier ages of the universe the galaxy formation happened in a very dusty and gas–rich environment (visible also in Figure 1.9, where L_{IR} increases with redshift); likely, the AGN feedback played a major role in the depletion of the medium. We now present two widely–known models for galaxy–AGN evolution, that mainly differ in describing the trigger of the AGN and star formation in the galaxies.

Merger–driven model

The most powerful quasars probably require galaxy mergers in order to trigger the high gas inflow rates, necessary to overcome the angular mo-

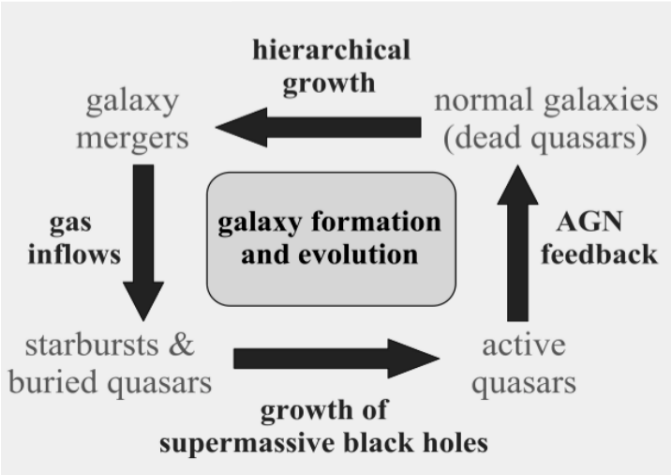

Figure 1.10: Schematic of the cosmic cycle that the galaxies may undergo after a major merger during their evolution (Hopkins, 2008).

mentum of the system in dynamical equilibrium. High accretion rates ($\gtrsim$ 1000 $M_\odot$/yr) can be hardily produced by secular or stand–alone galaxy processes, which likely regulate the evolution of low luminosity AGN.

One of the most known models, a schematic of which is reported in Figure 1.10, was firstly proposed by Sanders et al. (1988). In this scenario, the merger of two gas–rich systems forms a luminous infrared galaxy that gets more luminous as the merger progresses. Simultaneously, the central BH is being fed by infalling gas and obscured in a dust–enshrouded environment, until the gas reservoir is exhausted and/or driven out by the AGN feedback, unveiling the central nucleus. At this time, the infrared luminosity decreases and we observe such a system as a QSO. Progressively, as the consequence of the gas depletion by the BH feedback, the accretion rapidly ($\sim 10^8$ yr) quenches.

BH–galaxy Co–evolution model

In the co-evolutionary scenario (e.g. Lapi et al., 2014) the BH growth and star formation happen in absence of major mergers or interaction events, but rather result as a pure evolutionary phase of the system. The basic mechanisms that are though to connect the star formation and SMBH accretion lie in the inner galactic regions and are believed to be responsible both for feeding of the BH accretion and star formation, until quenching them in a short time-scale through the feedback. The formation of the system starts when dark matter halo undergoes the collapse constituted by an early fast phase in which most of the mass of the central region is accreted, followed by slower accretion phase that mainly affects the outskirts of the halo. The fast collapse is inhomogeneous resulting in the formation of clumps where

the star formation takes place. In these clumps also secular processes occur, that dissipate the angular momentum in a time–scale comparable with that of the starburst phase Δt_{burst}. The star formation rate is assumed constant for nearly 80% of Δt_{burst}; this implies that the reservoir of the cold gas should maintain the same mass over all the star formation phase, requiring equilibrium between gas accretion and consumption, i.e. between positive (condensation rate of the inflows of hot gas and metal–enriched gas returned to the medium by exploding stars) and negative (star formation rate, stellar and AGN activity) feedback. The gas collected in the reservoir sustain the AGN accretion until the final phase, in which strong winds form and deplete the gas, quenching the star formation and BH accretion. In this phase the QSO reaches its maximum luminosity, which later begins to decrease. A schematic of the evolution of the mass for the various components is reported in Figure 1.11.

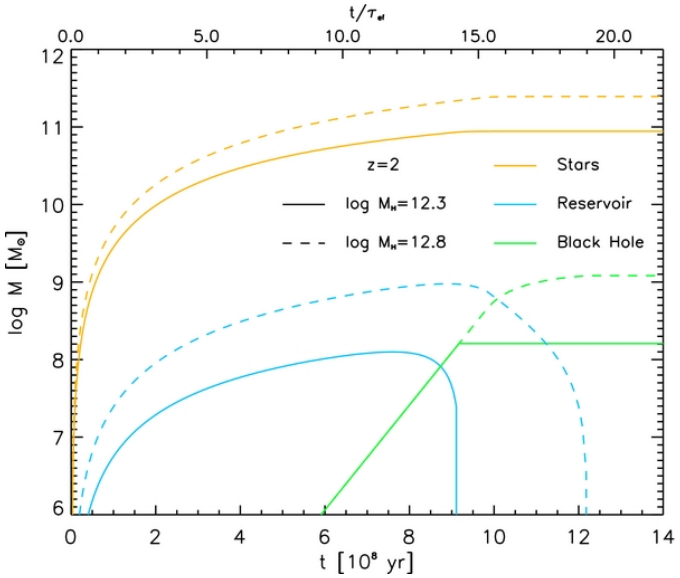

Figure 1.11: Evolution of the mass of the stars, reservoir and black hole for different initial dark matter halo masses (dashed and solid lines). The curves are plotted as a function of galactic age in units of 10^8 yr (lower scale) and of the e–folding time $\tau_{ef} \approx 6\times10^7$ yr (upper scale). Note that as the accretion mechanism of the BH becomes efficient, the reservoir is depleted by the feedback in $\sim 2 \times 10^8$ yr. Image taken from Lapi et al. (2014).

1.2 Sub–Millimetre Galaxies

Sub–Millimetre Galaxies (SMGs) are a class of ULIRGs that represent one of the most important population in the redshift range 2–4 (Blain et al., 2002); indeed, despite the distance of the sources, observations at mm/sub–mm

wavelengths take advance of a strong negative K–correction that balances the cosmological dimming, making observations nearly independent of redshift for z ∼0.5 – 10. They constitute a various galaxy population that spans from extreme infrared luminosities of 10^{13} $L_{\odot}$ and relatively warm dust components, to fainter objects (a few times $10^{12} L_{\odot}$) and containing colder dust (Magnelli et al., 2012). These sources are among the most studied targets given their extreme physical conditions and the role that they may have played in the evolution of star formation rate density and black hole accretion over the cosmic time.

SMGs were discovered in the late 1990s by the Submillimetre Common-User Bolometer Array mounted on the James Clerk Maxwell Telescope (e.g Smail et al., 1997; Hughes et al., 1998; Barger et al., 1998). Before the ALMA epoch, the identification of these sources was challenging owing to the low resolution of the instruments (e.g., ∼15 FWHM arcsec at 850 μm for Submillimetre Common-User Bolometer Array, SCUBA, on the James Clerk Maxwell Telescope); however, since they are often also powerful radio-sources, the resolution of radio–interferomenters allowed precise optical identifications that lead Chapman et al. (2005) to derived a peak redshift of z∼2.2 for the SMGs distribution. These results were lately confirmed by Simpson et al. (2014) (z = 2.3 ± 0.1) which present the first photometric redshift distribution with robust identifications based on observations with ALMA (Figure 1.12) carried out on a large sample of SMGs selected at 870 μm in the LABOCA Extended CDF–S (ECDF–S) Submm Survey (LESS), an extragalactic submillimetre survey performed by the Large Apex BOlometer CAmera (LABOCA) on the Apex Telescope. In addition, Zavala et al. (2014) have shown that the redshift distributions of SMGs, selected at different sub–mm/mm wavelengths, which were previously reported to be statistically different, are consistent with a parent distribution of the same population of galaxies, and the differences can be explained through selection effects.

The extreme infrared luminosity of some SMGs implies very high SFR (10^{2-3} $M_{\odot}\mathrm{yr}^{-1}$) (Chapman et al., 2005; Wardlow et al., 2011; Simpson et al., 2014). These objects feature stellar masses of 10^{10-11} $M_{\odot}$ (Hainline et al., 2011; Michałowski et al., 2012; Simpson et al., 2014). Indeed, exploiting the first self-consistent UV-to-radio spectral energy distribution fits of 76 SMGs Michałowski et al. (2010) found that in the redshift range 2–4 approximately 20% of the cosmic star formation rate density takes place in SMGs brighter than 0.1 mJy, and about ∼30–50% of stellar mass density is contained in SMGs (Figure 1.13).

ALMA provided an unprecedented boost to the study of SMGs. Given its capability to make extremely deep and high–resolution images of high–redshift galaxies, ALMA is an excellent and unique instrument for observing these sources, tracing the dust mass and temperature, the dusty star formation activity, and also the mass of the ISM. For example, exploiting the high resolution of ALMA, Karim et al. (2013) showed that the brightest

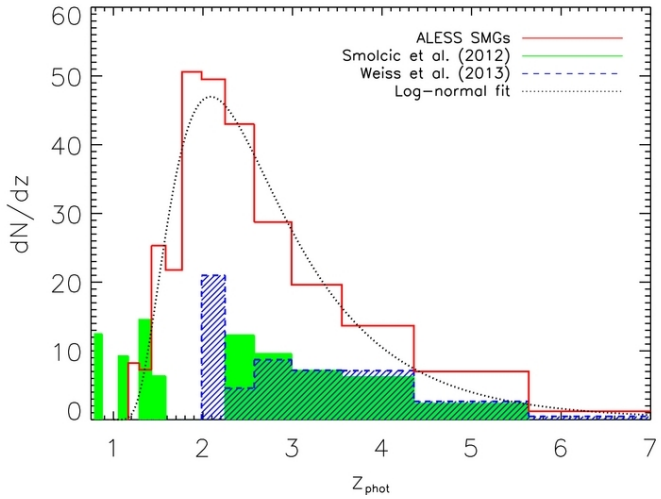

Figure 1.12: Photometric redshift distribution of the ALESS SMGs, binned uniformly in time, and normalized by the width of each bin (red solid line). For comparison, spectroscopic and photometric redshift distribution of 28 SMGs from Smail et al. (2012) (green shaded area) and spectroscopic redshift distribution of 25 lensed SMGs from Weiß et al. (2013) (blue dashed area) are reported. The black dotted line is a log–normal fit of the redshift distribution. From Simpson et al. (2014).

sources in the original LESS sample actually comprise emission from multiple fainter SMGs. Dunlop et al. (2017) conducted a deep submillimetre continuum survey of the Hubble Ultra Deep Field called ALMA SPECtroscopic Survey (ASPECS), finding that ∼85% star formation at z ≈ 2 occurs in a dusty obscured environment in high-mass galaxies (10^{10-11} $M_{\odot}$), for which the average obscured/unobscured SF ratio is ∼200. Nagao et al. (2012) observed the [NII] and [CII] atomic lines for one source (XID 403 of Xue et al., 2011, one of the sources included in this work), inferring from their flux ratio that the metallicity is consistent with solar; this implies that the chemical evolution has progressed very rapidly in high–z SMGs. Swinbank et al. (2014), exploiting 870 μm ALMA observations of LESS SMGs derived a median temperature of the dust component of $T_d = 32 \pm 1$ K, that is 3–5 K lower than that of comparably luminous local galaxies, reflecting the more extended star formation in these systems. They also derived an average dust masses of $M_d = (3.6 \pm 0.3) \times 10^8\, M_{\odot}$. Adopting a gas-to-dust ratio of $M_{H_2}/M_d = 90 \pm 25$ (as appropriate for metal rich galaxies, Carilli and Walter, 2013), the dust mass led to a typical molecular gas mass of $M_{H_2} = (4.2 \pm 0.4) \times 10^{10}\, M_{\odot}$ for SMGs. Thus, using the information about SFR and total H_2 mass, they inferred an average gas depletion time–scales of the gas $\tau = M_{H_2}/SFR = 130 \pm 15$ Myr. In addition, the first spatially resolved CO gas kinematics in SMGs (Tacconi et al., 2008) revealed that these source may have multiple morphologies with complex gas motions and that the star–forming gas can lie in compact, rotating disk structures. This pos-

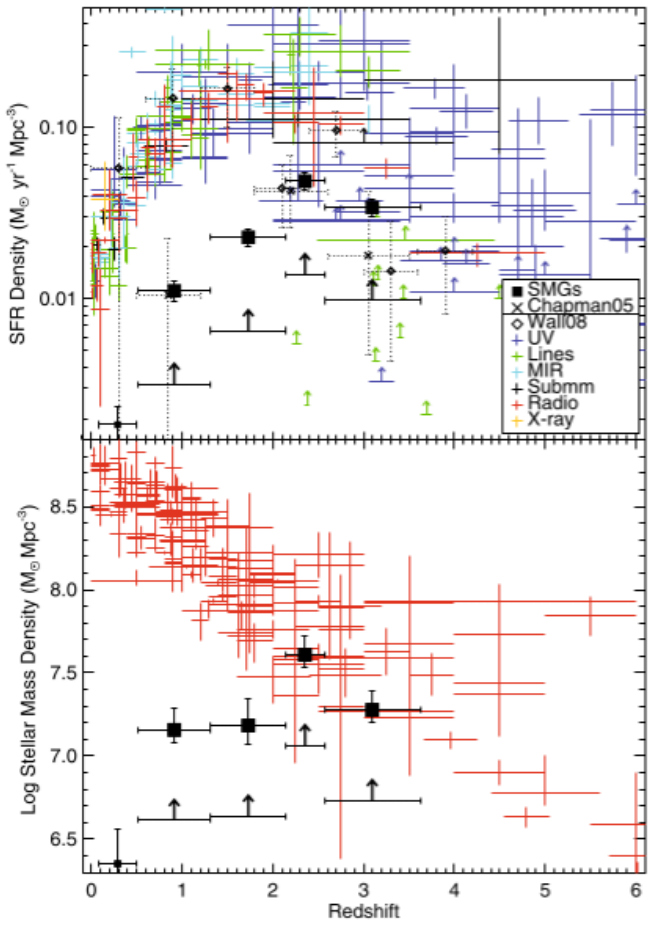

Figure 1.13: Cosmic star formation rate density (top panel) and cosmic stellar mass density (bottom panel) for a sample of 76 SMGs devided in four bins of redshift, indicated by the filled black squares. The black arrows indicate the SMG data without incompleteness sample correction and correspond to a lower limit to their SFR density and stellar mass density. In the top panel the colored symbols refer to other works or values derived from other bands and reported in the box. In the bottom panel the red points with error bars are the values of cosmic stellar mass density from the available literature. From Michałowski et al. (2010).

sibility was lately confirmed by many observations (e.g. Hodge et al., 2012; Ivison et al., 2013; De Breuck et al., 2014). As to SMGs size, high–resolution observations in the far–IR/(sub)mm band have shown that star formation occurs in clumps distributed in compact dusty regions over few kpc scale (Ikarashi et al., 2015; Barro et al., 2014; Massardi et al., 2018). Lapi et al. (2018) derived analytic estimates of the galaxy sizes over their evolution, relying on numerical simulations and basic physics arguments, finding results in agreement with the aforementioned observations. The morphology of these objects appears extremely various and hard to characterize: rest-frame opti-

cal emission, from HST data, shows a wide range of morphologies including discs, apparent spheroids and irregular systems (e.g Swinbank et al., 2010; Wiklind et al., 2014; Chen et al., 2015).

Despite SMGs are primarily powered by star formation, a considerable fraction of them hosts an AGN whose contribute to the bolometric emission is often not negligible (up to 20%, Alexander et al., 2005). Ueda et al. (2018) investigated the X–ray properties of AGN hosted in SMG detected by ALMA in the Great Observatory Origins Deep Survey South field (GOODS–S). They found that the AGN fraction in the redshift range 1.5 –3 is 90^{+8}_{-19}% for the SMGs with $L_{IR} = 10^{12-12.8} L_{\odot}$ and 50^{+23}_{-25}% for those with $L_{IR} = 10^{11.5-12} L_{\odot}$. However, they also report that the majority of them ($\sim 2/3$) are dominated by star formation, since the ratio between their X–ray and IR luminosities, L_X/L_{IR}, is lower than what is expected from the local BH to stellar mass relation $M_{BH} - M_*$, derived from $\dot{M}_{BH}$/SFR, assuming $\dot{M}_{BH} \propto L_X$ and SFR $\propto L_{IR}$. This would imply a very inefficient accretion rate (Eddington ratio $\sim$0.01) for such sources, contradicting what most evolutionary models predict. This discrepancy is solved assuming that the BH has a mass $\sim$10 times smaller than what is expected from the local $M_{BH} - M_*$ relation. This implies that these systems may be young galaxies at the early stages of their evolution, hosting an "evolved" SMBH.

The values of the SFR, high metallicity, large masses and high gas fractions of SMGs are all suggestive of a close link to the formation phase of the most massive spheroids (e.g Smail et al., 2004). Clustering analyses have shown that SMGs typically reside in overdense regions (Hickox et al., 2012; Simpson et al., 2014; Hodge et al., 2016), suggesting that physical interactions such as merger processes may play a key role in the galaxy evolution. Indeed, in a sample of 14 SMGs, Wardlow et al. (2018) found that 36 ± 18% of submillimetre sources that appeared blended in low–resolution maps are actually composed of multiple SMGs components that are physically associated, confirming that the SMGs inhabit overdense regions. However, they concluded that only 21 ± 12% of the sources have a confirmed companion at small enough spatial and spectral separations ($\sim$8–150 kpc and 300 km/s) to be able to trigger their star-formation by interactions, leaving open the issue of what may account for the starbursts in the remaining $\sim$80% of SMGs. One of the most recent versions of the semi-analytic model of galaxy formation, GALFORM (Cowley et al., 2015; Lacey et al., 2016), and some hydrodynamical simulations (e.g Davé et al., 2010; Hayward et al., 2011; Narayanan et al., 2015) predict that bright SMGs typically represent isolated, gas-rich systems undergoing self–regulated evolution processes.

1.3 Scientific rationale and objectives

The fraction of luminous ($L_X > 10^{44}$ erg/s) heavily obscured (namely, $\log N_H > 23$) AGN increases up to 60% at z∼4, as shown by the study of the hard X–ray luminosity function evolution performed by of the Vito et al. (2014); they also shown that the obscured luminous AGN fraction is overall higher than the value in the local Universe, suggesting an evolution these objects. Whether the host galaxies give a significant contribution to the obscuration or not is currently unknown, but given that the gas fraction increases with redshift (Carilli and Walter, 2013) and the average size of objects decreases (van der Wel et al., 2014), it is very likely that the host galaxies play an important role in obscuring the central engine.

Moreover, SMGs are among the best candidates as progenitor of compact quiescent galaxies (cQGs, Cimatti et al., 2008), a class constituted by quiescent galaxies (of which they represent a substantial fraction at z > 1) that are considerably smaller and denser than local galaxies of similar mass, showing stellar half–light radii of $\sim 0.5 - 2$ kpc and typical masses of $\sim 10^{10} M_{\odot}$ (Cassata et al., 2011). The formation mechanism of cGQs is still debated: Barro et al. (2013) identified a population of compact star forming galaxies (cSFGs) as the likely progenitor of cQGs at redshift range 1 – 2.

The observations subject of this work (described in Chapter 2) aimed at detecting of continuum (at $\sim 2.1mm$) and CO emission in a sample of six SMG hosting an obscured AGN at redshift >2.5. The main objectives are:

- measure the angular size and flux of both continuum and line emission, in order to obtain the masses and physical sizes for the dust and molecular gas content of the sources.
- derive their ISM densities and evaluate its contribution to the absorption measured from the X–ray spectra, usually ascribed to the parsec–scale torus surrounding the central engine, assuming different geometries for the objects.
- study the morphology and kinematics of the objects in order to possibly individuate indications of mergers; in addition, these information coupled to the other physical derived quantities such as SFR and stellar mass would reveal whether these objects are the likely progenitors of cQGs.

1.4 Target selection and description

The Chandra Deep Field South (CDF–S, 16 × 16 arcmin) provides the best X–ray spectral information currently available, thanks to its 7–Ms exposure

time (limit flux within 1 arcmin from the center of the field: $F_{0.5-7keV} \approx 2 \cdot 10^{-17}$ erg s^{-1} cm^{-2}). In addition, this field features an exceptional multi-wavelength coverage that allows the characterization of the overall spectral properties of the sources with extraordinary accuracy. In particular, the optical–IR band is especially well covered thanks to the coordination of the observations carried out with different observatories such as HST, Herschel, Spitzer. Moreover, many observations in the submillimetre band were taken with instruments such as SCUBA and LABOCA on the Apex telescope. The central area of the CDF–S is covered by the GOODS–S, in which the Cosmic Near–IR Deep Extragalactic Legacy Survey (CANDELS), a powerful imaging survey of the distant universe, has been carried out with HST. CANDELS consists of two different areas and depth portions, the deeper and smaller CANDELS/Deep and the more shallow and extended CANDELS/Wide. Moreover, the CDF–S was observed by the the Galaxy Evolution from Morphology and SEDs (GEMS) survey; GEMS is a large-area (800 arcmin^2) two-color (F606W and F850LP) imaging survey with the Advanced Camera for Surveys (ACS) on the HST.

For the purposes of this work the sample from Vito et al. (2013), consisting in 34 X–ray selected AGN at $z > 3$ in the 4–Ms CDF–S, was combined with the 8 heavily obscured QSOs in a redshift range 1.1–3.7, selected in the 1–Ms exposure in CDF–S by Rigopoulou et al. (2009) and observed at 850 μm with SCUBA. In this combined sample the target selection has been carried trough the following criteria:

- Secure spectroscopic redshift (errors $<$ 300 km/s) > 2.5, in order to avoid the large error related to the photometric redshift that would propagated in the derived fundamental quantities for our study (such the intrinsic luminosity) and properly choose the lines to target in the observations. The redshift threshold at z = 2.5 was chosen in order to study the cosmic epoch in which the distribution of SMGs peaks (Figure 1.12) and most of the SF and BH accretion happen (Figures 1.8, 1.13).

- Column density $\log N_H > 23$ in order to include only heavily obscured objects and trace the evolutionary stage in which the AGN is still deeply buried and the SF is high.

- Detection at $\lambda_{obs} > 100$ μm in order to obtain important quantities such as SFR and stellar mass from a well constrained SED fitting.

The selection resulted in a total of six matching sources spanning from z$\sim$2.5 (cosmic time[1] $t \sim 2.6$ Gyr) and z$\sim$4.8 ($t \sim 1.2$ Gyr), whose position are shown in Figure 1.14 and reported in Table 1.1. Despite the small number

[1]adopting a ΛCDM cosmology: $H_0 = 69.6$, $\Omega_M = 0.286$, $\Omega_\Lambda = 0.714$ (Wright, 2006).

of sources (owing to the stringent selection criteria), this sample represents a complete and unique collection of objects: they are characterized by a relatively high number of counts (from ∼260 to ∼2000 in the 7–Ms exposure) in the X–ray band which would allow to test complex emission models, and by an excellent IR coverage lacking in precedent studied samples (e.g. Vito et al., 2014, 2016), from which derive well constrained physical quantities such as SFR and stellar mass from the SED fitting. All the sources are included in CANDELS/Deep area, except for XID 403 that lies in CANDELS/Wide and XID 34 that is outside CANDELS covered field, but it is included in the GEMS catalog and in the Multiwavelength Survey by Yale-Chile (MUSYC) catalog, consisting of deep optical medium-band and broadband optical and near-IR imaging of the CFDF–S.

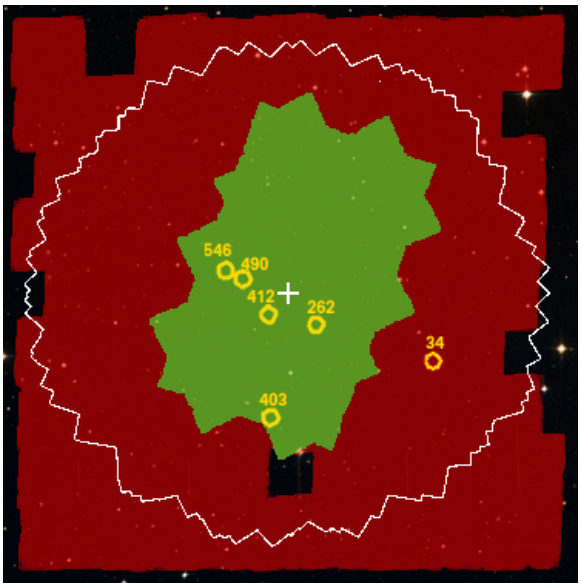

Figure 1.14: Sources position superimposed on a Digitized Sky Survey (DSS) image ($\sim 28' \times 28'$) centered on the CDF–S (white cross). The white contour corresponds to the CDF–S coverage of the 7–Ms exposure, while the red shade is the GEMS covered field that includes GOODS–S CANDELS (green shade). The only source outside CANDELS is XID 34.

Circosta et al. (in prep.) have performed an in–depth analysis of these sources, modeling the X–ray spectrum and the optical–IR SED in order to derive their fundamental physical properties.

The X–ray spectra have been firstly fitted by means of phenomenological models, one that is transmission dominated (including a primary emission power–law, intrinsic photoelectric absorption, a Gaussian line and an unabsorbed power–law for the soft emission), and one that is reflection dominated (characterized only by a reflection component and a Gaussian line). Then a more complex physical model has been tested, in which the transmission,

reflection and line components are auto–consistently included; this model is named MYTorus (Murphy and Yaqoob, 2009, based on a toroidal geometry with an opening angle of 60° and cold, neutral and uniform reprocessing material).

Photometric data used for the SED fitting were taken from the Rainbow Cosmological Surveys Database (https://rainbowx.fis.ucm.es/Rainbow_Database/Home.html), which combines all the measurements from the available surveys. The data were modeled using the SED fitting code originally presented by Fritz et al. (2006) and improved by Feltre et al. (2012). The code fits the data simultaneously accounting for three different components (described in § 1.1.3): stellar emission (modeled by means of SSPs) that peaks in the near–IR, reprocessed emission from the dusty torus surrounding the AGN that peaks in the mid–IR, and emission by the cold dust of the host galaxy that is heated by starburst activity and peaks in the far–IR.

As an example we show the fits of the X–ray spectrum and the IR SED of XID 490 (at z=2.578) in Figure B.1 and Figure B.2, respectively (Appendix B). The ID from the Xue et al. (2011) 4–Ms catalog, the ID from Luo et al. (2017) 7–Ms catalog, the CANDELS ID, the position, the redshift, the CO transition, and the physical quantities derived from the fits by Circosta et al. (in prep.) are reported in Table 1.1. In particular, the X–ray luminosity and column density were obtained from the X–ray spectral fitting. Results for MYTorus have not been reported for the sources XID 34 and XID 403 as the poor quality of the data did not allow a well–constrained data fitting. XID 546 is the brightest X–ray source among the sample and the only without a detected iron Kα line, thus the reflection dominated model has not been tested. The IR luminosity, the fractional AGN contribution to IR luminosity, the SFR and the stellar mass correspond to the best fit parameters of the optical–IR SED. Additionally, from the relation between $L_{850\mu m}$ and CO luminosity found by Scoville et al. (2016) and assuming a ratio between molecular and atomic mass $M_{H_2}/M_{gas} \approx 5$ (Calura et al., 2014), the total gas mass was derived for each source.

All the tested models for the X–ray emission return a similar N_H value, within 1σ. Thus, as the simplest model is the transmission dominated, we will compare the column density that we will derive in this work (measuring the CO luminosity and the physical sizes of the sources) with the column density relative to this model.

All targets are massive, strong star–forming and very luminous galaxies. Three of them are well known heavily obscured AGN: XID 262 was firstly detected in the early 1–Ms CDF–S exposure and classified as a type II QSO object in the spectroscopic follow–up (Szokoly et al., 2004). This result was later confirmed by Mainieri et al. (2005) who also reported the first submillimetre detection at 850μm using SCUBA. XID 412 was the first type II AGN ever detected in the CDF–S 1–Ms exposure at z>3 (Norman et al., 2002). Comastri et al. (2011) have confirmed its Compton–thick nature

			Observation				Optical–IR SED					X–ray spectrum			
XID	XID	CID	RA	Dec	z_{spec}	CO	L_{IR} (10^{12} $L_\odot$)	f_{AGN}	SFR ($M_\odot$/yr)	M_* (10^{11} $M_\odot$)	M_{gas} (10^{10} $M_\odot$)	Model	$L_{[2-10\ \mathrm{keV}]}$ (10^{44} erg/s)	N_H (10^{23} cm^{-2})	
(1)	(2)	(3)	(4)	(5)	(6)	(7)	(8)	(9)	(10)	(11)	(12)	(13)	(14)	(15)	
262	337	5479	03:32:18.8	-27:51:35.5	3.660	6–5	3.2	0.14	470 ± 100	3.0	1.0 ± 0.3	Trasmission	$2.43^{+0.60}_{-0.46}$	$14.9^{+5.6}_{-3.6}$	
												Reflection	$0.24^{+0.02}_{-0.02}$	–	
												MYTorus	$3.97^{+2.92}_{-1.17}$	$14.8^{+7.7}_{-3.7}$	
412	551	6294	03:32:29.8	-27:51:05.8	3.700	6–5	2.6	0.08	410 ± 80	1.9	0.9 ± 0.3	Trasmission	$2.85^{+0.42}_{-0.39}$	$9.9^{+2.5}_{-2.0}$	
												Reflection	$0.33^{+0.04}_{-0.04}$	–	
												MYTorus	$3.67^{+0.87}_{-0.68}$	$9.0^{+2.1}_{-1.7}$	
34	42	326[1]	03:31:51.9	-27:53:27.1	2.940[2]	5–4	7.3	0.04	1210 ± 240	0.96	3.7 ± 1.1	Trasmission	$1.96^{+1.04}_{-0.67}$	$2.0^{+1.3}_{-1.0}$	
												Reflection	$0.81^{+0.07}_{-0.07}$	–	
403	539	273	03:32:29.3	-27:56:19.5	4.755	7–6	6.2	0.01	930 ± 190	1.7	4.9 ± 1.5	Trasmission	$2.97^{+2.16}_{-1.37}$	$14.8^{+9.6}_{-5.8}$	
												Reflection	$0.29^{+0.05}_{-0.05}$	–	
546	746	10578	03:32:39.7	-27:48:50.6	3.064	5–4	2.8	0.06	450 ± 90	4.1	4.6 ± 1.4	Trasmission	$3.83^{+1.65}_{-1.06}$	$4.4^{+0.8}_{-0.7}$	
												MYTorus	$6.07^{+0.60}_{-0.55}$	$5.4^{+0.6}_{-0.5}$	
490	666	9834	03:32:35.7	-27:49:16.0	2.578	4–3	5.2	0.21	700 ± 140	4.0	3.3 ± 1.0	Trasmission	$0.93^{+0.10}_{-0.20}$	$29.0^{+30.7}_{-14.4}$	
												Reflection	$0.63^{+0.07}_{-0.06}$	–	
												MYTorus	$1.06^{+1.88}_{-0.08}$	> 34	

Table 1.1: Summary of the targets observational characteristics (left columns) and physical properties as derived by Circosta et al. (in prep.) from optical–IR SEDs (central columns) and X–ray spectra (right columns) fitting. Sub-columns are enumerated from left to right as follow: (1) X–ray ID in Xue et al. (2011) catalog (4–Ms). (2) X–ray ID in Luo et al. (2017) catalog (7–Ms). (3) CANDELS ID. (4),(5) Right Ascension and Declination. (6) Spectroscopic redshift derived from optical spectra as reported in the catalog. (7) The CO transition targeted in this work. (8) IR luminosity integrated in the 8 – 1000 μm range. (9) Fraction of the AGN contribution to the total IR luminosity. (10) Star Formation Rate. (11) Stellar mass. (12) Total mass of the gas calculated as $M_{gas} = M_{H_2} + M_{HI}$. (13) Model used to fit the X–ray spectrum. (14) X–ray absorption corrected luminosity integrated in the 2 – 10 keV rest–frame range. (15) Intrinsic column density of the source.
Errors on the $L_{[2-10\ \mathrm{keV}]}$ and N_H are given at the 90% confidence level, while errors on the quantities derived from the SED–fitting are given at 68% confidence level. Relative errors are ∼30% for the stellar mass and ∼20% for the IR luminosity.
[1]XID 34 was is not included in CANDELS, thus the ID from GEMS (Häussler et al., 2007) is reported.
[2]The redshift of XID 34 was found to be measured using Ly–α line, which is known to be challenging as redshift estimator. In Chapter 3 we derive it by mean of other lines in the optical spectrum, finding a better estimate of $z_{spec} = 2.937$.

performing an X-ray spectrum analysis using 3.3–Ms XMM-Newton survey data. XID 403 is one of the widely studied sources in the CDF–S. Gilli et al. (2014) have performed an in–depth analysis through an observation of the continuum in band 6 (∼1.3 mm) during Cycle 0, combining it with continuum observatios in band 7 from ALESS and in band 6 from previous works (Nagao et al., 2012). They built a full SED including Herschel data and obtained dust temperature and size, and the SFR. This result has been confirmed by De Breuck et al. (2014), who also suggested that the gas kinematics is dominated by a rotating thin disk characterized by strong turbulence. XID 34, XID 546 and XID 490 are the less studied objects, which have been recognized as Type II QSO since the first 1–Ms exposure in the CDF–S. It is worth noting, for our purposes, that XID 34 has been targeted in several ALMA projects before: it was firstly observed in band 7 (∼850 μm) during Cycle 0 as part of ALMA LESS (ALESS) survey (Hodge et al., 2013) and included in the catalogue with the ID ALESS 057.1. Other observations in band 3 (∼3.1 mm) and band 4 (∼2.2mm) are available. However, their resolution and sensitivity were too poor for the objectives presented in this work.

In the following, we adopt the ID from Xue et al. (2011) to identify the sources.

Chapter 2

ALMA observations

In this chapter we present the observations of the sample described in the previous chapter, carried out with the Atacama Large Millimetre Array (ALMA) (ID: 2015.1.01205.S, PI: R. Gilli). The project was accepted with the lowest priority (i.e. *filler* status) and hence was only partially observed in September 2016 during ALMA observing Cycle 4, as detailed in the following. We present a general overview of the datasets and describe the reduction procedure and diagnostic analysis.

A comprehensive description of ALMA, its functioning and basis of interferometry are given in the ALMA Technical Handbook (https://almascience.nrao.edu/documents-and-tools/cycle5/alma-technical-handbook/view). Here we summarize in the text only the details useful for a better description and understanding of our analysis.

2.1 Data description

The instrumental setup was aimed at observing at least one CO transition for each of the targets. Given the source redshift distribution (see Table 1.1), a different CO transition has been selected for each of them: Band 4[1] (ranging between 125 and 163 GHz) offered the most convenient settings to minimize the observing time. Two spectral setups were used by centering the 2×4 GHz *sidebands* respectively at 139.5 and 127.5 GHz to observe the sources XID 490, XID 546 and XID 403, and at 135 and 147 GHz for the sources XID 34, XID 262 and XID 412 (Figure 2.1). All the pieces of information needed to the observation, including the source positions and instrumental setup, is stored in a command set known as *scheduling block*. Then two different sets of spectral parameters result in two distinct scheduling blocks within the same project, each containing the observational setting for three sources. One scheduling block is repeated as many times as needed to achieve

[1]The frequency range available to ALMA is divided into different receiver bands, spanning from band 3, starting at 84 GHz, to band 10, ending at ∼950 GHz.

the sensitivity required by the PI. Each scheduling block repetition (i.e. the actual observation) is called *execution block*; so one project might have several execution blocks for the same scheduling block.

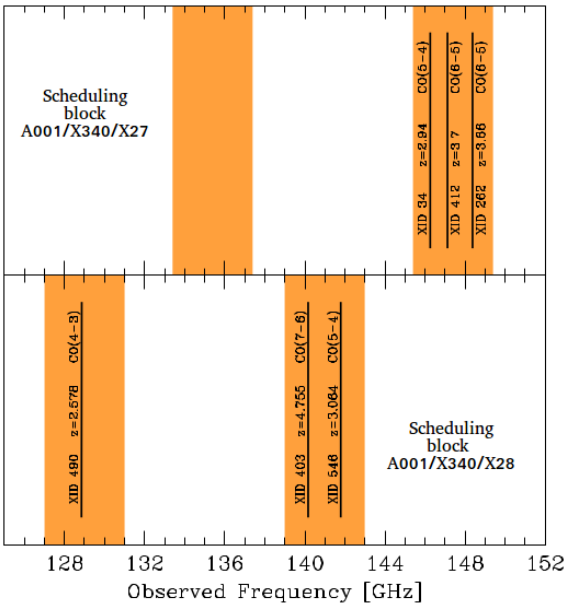

Figure 2.1: ALMA band 4. Orange shades are the sidebands, while the top and bottom panels correspond to the two scheduling blocks. The sidebands have been located in different spectral intervals in order to detect, along with the continuum emission, at least one line from a CO transition per source. Vertical black lines show which transition for each source is detected and the corresponding frequency.

The scheduling block concerning the observation of XID 490, XID 546 and XID 403 (named in the following as *SB–1*) was repeated twice, achieving the PI's requested sensitivity; the two execution blocks of SB–1 will be named *EB–1* and *EB–2*. Unfortunately, the scheduling block (*SB–2*) related to the other three sources XID 262, XID 412 and XID 34 has not been executed more than once (*EB–3*) before the end of the cycle. Table 2.1 reports a summary of the data structure briefly described above. The distribution of the 12 m–antennas array in a polar-logarithmic plot is shown in Figure 2.2.

Four *basebands*[2] were distributed within the sidebands, in each of which a 1875 MHz *spectral window*[3] (*spw*) was allocated, sampled in 240 channels of 7.812 MHz width corresponding, at the median frequency of the spws, to 17.46 km/s in velocity for SB–1 and to 16.64 km/s for SB–2. The spectral setup is reported in Table 2.2.

For both scheduling blocks, QSO J0334-4008 has been used to calibrate

[2]Within each sidebands, ALMA allows up to 2×1.875 GHz basebands.

[3]A spectral windows corresponds to the actually observed frequency range. Up to 4 spectral windows can be placed in each baseband.

PROJECT ID: 2015.1.01205.S

SCHED. BLOCK	A001/X340/X28 **(SB–1)**		A001/X340/X27 **(SB–2)**
EXEC. BLOCK	A002_Xb87877_X7151 **(EB–1)**	A002_Xb87877_X7efa **(EB–2)**	A002_Xb8cea2_X1d73 **(EB–3)**
Start time (UTC)	2016-09-23 06:12:10	2016-09-23 08:45:22	2016-09-29 05:59:33
End time (UTC)	2016-09-23 07:15:21	2016-09-23 09:48:51	2016-09-29 07:05:06
Time on source (min)	44	44	46
Number of Antennas	38	38	43
Baseline max (km)	3.1	3.1	3.1
Baseline min (m)	15.1	15.1	15.1
Angular Resolution	0.15"	0.15"	0.14"
Largest Angular Scale (LAS)	30.46"	30.46"	29.04"
Field of View (FoV)	38.32"	38.32"	36.53"

Table 2.1: Summary of ALMA observations used in this work. The science project is composed of two scheduling blocks: A001/X340/X28 and A001/X340/X27, each containing the observational information for respectively three sources: XID 490, XID 546, XID 403 and XID 262, XID 412, XID 34. The first scheduling block was repeated twice while the second just once. Time on source for each execution block is almost the same (∼45 min), so the three sources of the second scheduling block were observed for half of the time with respect to the sources in the first. Angular resolution, LAS and FoV refer to the median frequency for each scheduling block (see Table 2.2). For simplicity, in the rest of this thesis we will rename the scheduling blocks and execution blocks as reported in brackets besides their name.

SB	SB–1			SB–2		
SPW	Start (GHz)	Centre (GHz)	End (GHz)	Start (GHz)	Centre(GHz)	End (GHz)
0	138.56	139.50	140.44	147.06	148.00	148.93
1	140.46	141.40	142.33	145.17	146.11	147.04
2	126.56	127.50	128.44	135.06	136.00	136.93
3	128.45	129.40	130.33	133.07	134.00	134.94

Table 2.2: Spectral windows (SPW, first column) setup for each scheduling block (SB, first row). Each spectral window has a bandwidth of 1.875 GHz divided in 240 channels of 7.812 MHz width.

the flux and frequency trasmission (bandpass), while QSO J0348-2749 served as phase calibrator over the time. Table 2.3 reports the coordinates for both targets and calibrators.

The bandpass calibrator is a powerful (in order to have high signal–to–noise ratio, SNR, in a short time) point–like source placed at the center of the phases, hence we expect that its phase scatters around zero over all the frequencies. It has been observed just once for a ∼5 minutes *scan*[4] at the beginning of the observation, since variations of flux over frequency are not expected to be significant during the observation timescale. The phase calibrator is also a point–like source, so we expect that its amplitude maintains a constant value all over the observing time. The phase variation over time has to be monitored during all the observation, hence the phase calibrator is observed before and after each scan in which the scientific targets are observed; each phase calibrator solution will be then interpolated in order to derive the corrections to apply to the targets. In this project it has been pointed for ∼30 seconds every ∼10 minutes, that is the time interval in which

[4] A scan is the minimum time interval spent observing only one source. An observation is typically composed of several scans related to calibration and scientific intents.

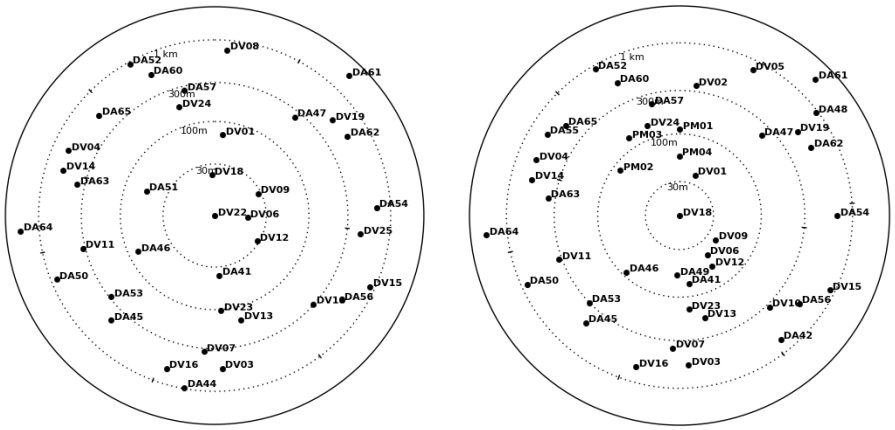

Figure 2.2: Polar-logarithmic plot of antenna positions for EB–1 (left panel) and EB–2 (right panel) used in this work. The solid external line corresponds to a distance of 3 km.

the targets have been observed. As an example, the EB–1 time–line of the observations of flux, bandpass and phase calibrator, along with the scientific targets, is reported in Figure 2.3.

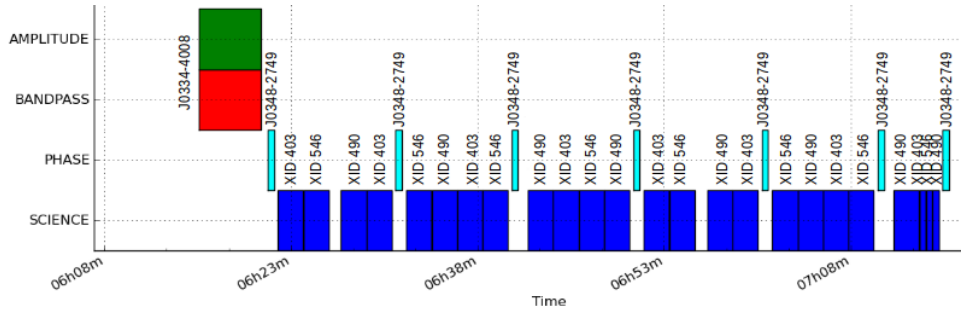

Figure 2.3: Scans of the observations for EB–1. Different colors correspond to different intents of the scan, reported on the vertical axis. On each scan the name of the target is reported. QSO J0334-4008 has been observed once at the beginning of the observation and served for both flux and bandpass calibration. The phase calibrator QSO J0348-2749 has been observed before and after each set of scientific target observations.

2.2 Data reduction

We have downloaded the raw data from the ALMA archive and processed them via the ALMA *pipeline* using CASA version 4.7.0–1. The pipeline procedure automatically flags bad data and performs the calibration; it also produces several diagnostic plots, accessible via the *weblog* interface, that are useful to identify possible calibration failures and discern additional needed flags; thus we have inspected both diagnostic plots and calibrated data in

TARGETS

SB A001/X340/X28			SB A001/X340/X27		
Source ID	RA	Dec	Source ID	RA	Dec
XID 403	03:32:29.290	-27:56:19.460	XID 262	03:32:18.831	-27:51:35.480
XID 546	03:32:39.670	-27:48:50.640	XID 412	03:32:29.850	-27:51:05.850
XID 490	03:32:35.720	-27:49:16.040	XID 34	03:31:51.920	-27:53:27.100

CALIBRATORS

Source ID	RA	Dec
J0334-4008	03:34:13.654	-40:08:25.398
J0348-2749	03:48:38.145	-27:49:13.566

Table 2.3: Coordinates of the observations, divided in scientific targets (top) and calibrators (bottom). Scientific targets are divided in two execution blocks (see text for details), whereas calibrators are common for all observations; J0334-4008 served as flux and bandpass calibrator while J0348-2749 has been used to calibrate the phases.

order to assess if the calibration was successful. After the inspection (detailed in the following), the pipeline calibration results to be satisfying, and we proceed to data analysis (Chapter 3).

We recall that the visibilities sample the Fourier Transform (FT) of the brightness distribution domain; the plane where the visibilities are represented is called the u–v plane. The visibilities are complex numbers and can be written as:

$$V = Ae^{i\phi} = A(\cos\phi + i\sin\phi) = Re + iIm$$

where A is the amplitude, ϕ is the phase, $Re = A\cos\phi$ is the real part and $Im = A\sin\phi$ is the imaginary part.

2.2.1 System Temperature

The System Temperature[5] (T_{SYS}) is measured in four spws with low resolution ($\sim$ 128 channels) centered at the same frequency of those reported in Table 2.2 where the scientific data were collected; we have inspected the T_{SYS} before and after the flagging process in order to check that the pipeline has properly flagged those antennas which display anomalies with respect to the expected trend; in particular, we expect almost the same behavior for all antennas in each spw for both polarizations, whereas too high spikes and periodic signals over frequency imply that additional flags with respect to pipeline are needed. However, too strict flagging criteria would result in

[5]The System Temperature is a measure of the noise introduced by both the receiver and the atmosphere (which is prevalent at millimeter wavelengths). It is defined as the temperature of a resistor emitting (as black body) a signal equal to the sum of all the contributions to the noise, placed above the atmosphere.

a possible significant loss of signal that would reduce the SNR, thus the trade–off between the data quality and SNR should be carefully taken in account.

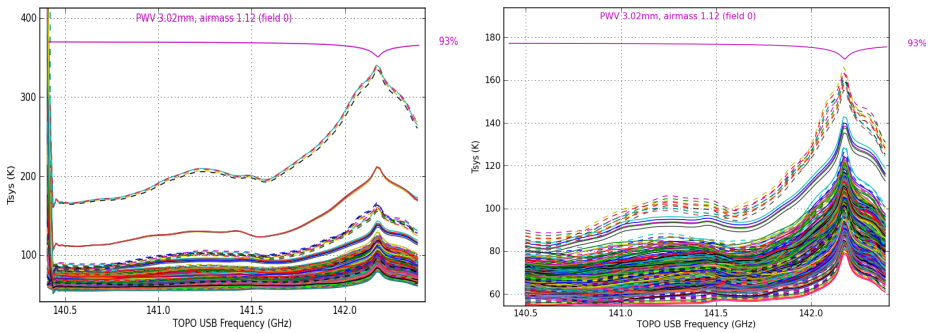

Figure 2.4: T_{SYS} for EB–1 referred to the flux calibrator field in the spw corresponding in frequency to spw 1 in Table 2.2, averaged by time and colored by antenna. Solid and dashed lines refer respectively to XX and YY polarizations, while the horizontal magenta line is the atmospheric transmittance expressed in percentage of transmitted signal. Left and right panel are before and after flagging, respectively. Note how the pipeline has correctly flagged the antennas which present anomalies: the most evident case is that of antenna DV51, whose signal is far above the others for each polarizations. Also the edge channels have been properly flagged.

Figure 2.4 shows an example of T_{SYS} diagnostic plot before (left panel) and after (right panel) flag application, referred to the flux calibrator field in an energy range centered in scientific spw 1 for EB–1. Solid and dashed lines represent the two polarizations. On the top of the figures the atmosphere transmittance (horizontal magenta lines) is reported as percentage of transmitted signal. At ∼142.2 GHz there is a clear feature associated with an atmospheric emission line, that induces a decline in the transmittance function at the same frequency. This is considered a normal behavior that will be corrected during T_{SYS} calibration phase and no flag is needed. However, in the left panel it is visible that for both polarizations of one antenna the signal is far above the others; this antenna was found to be DV51 that has been correctly flagged (right panel) in this spw (actually, this antenna was flagged in all the execution blocks because preserves this anomaly for all spws and scans). Also the edge channels, which are known to have a bad response (visible in the left corner of the left panel in Figure 2.4), have been properly flagged.

T_{SYS} calibration essentially applies a correction for the instrumental and atmospheric contribution to the noise, which is largely dominated by the latter in the (sub)mm band. However, such a correction results in a further scatter of visibilities since it introduces statistical noise that is proportional to the perturbation that is needed to be corrected. As an example, in the left panel of Figure 2.5 the amplitude versus frequency for XID 403 in EB–1 is

displayed; at ∼142.2 GHz there is a significant increase of scattering, which exactly corresponds to the atmospheric emission line shown in Figure 2.4.

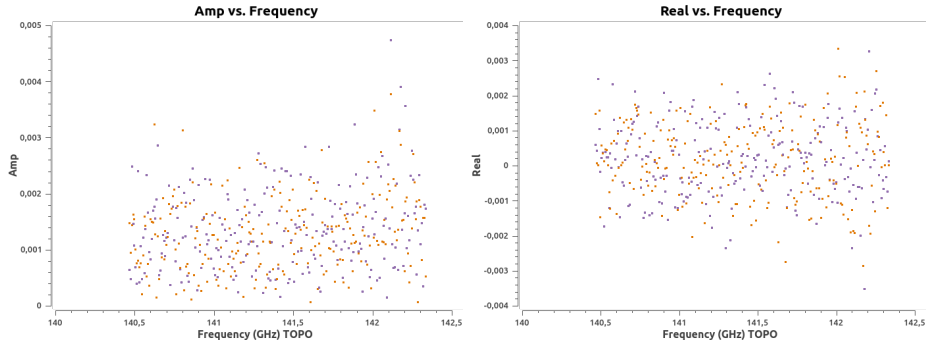

Figure 2.5: Amplitude (left panel) and real part (right panel) of the signal over frequency for XID 403 in spw 1(EB–1), averaged for time, scans and baselines and colored by polarization, expressed in Jy. In both panel the increase of scatter at the frequency corresponding to the atmospheric feature (shown in Figure 2.4) is displayed.

Without previous T_{SYS} inspection, one may confuse this scattering for an intrinsic data feature, such an emission line; this is also the case of less evident T_{SYS} perturbations that may be missed during the inspection but still produce an increase of scattering which leads to an ambiguous interpretation of the data. A simple way to understand if a feature is physical or not is to inspect the real part of the signal versus frequency. Since a visibility V is a complex number, its amplitude is always positive by definition, whereas the real part can be both positive or negative; thus, for a noise feature we expect that the real part just scatters symmetrically with respect to zero, because statistically there are the same chances to be positive or negative. For an intrinsic data feature related to a point–like source (i.e. $\phi \sim 0 \rightarrow Re \sim A,\ Im \sim 0$) we expect that the real part is asymmetrically shifted towards positive values. In right panel of Figure 2.5 we can see that at the frequency corresponding to the hypothetical feature in the amplitude (visible in the left panel), the real part scattering is just increased but perfectly symmetrical; then, even if such an element would have been missed during T_{SYS} inspection, we can securely conclude that it is noise.

2.2.2 Source detection and size in the Fourier space

A first evaluation of source detection can be performed directly in the visibilities space by exploiting the properties of complex numbers discussed above. If a source is nearly point–like its flux is almost totally distributed in the real part of the visibility, while the imaginary part tends to be null; thus, if we plot the complex plane for a point–source, we expect that the imaginary part always scatters around zero irrespectively of whether the source is detected or not; the real part instead would be positively shifted in case the source

flux is above the sensitivity threshold, while it would scatter around zero if the noise dominates (i.e. the source is undetected). As an example, Figure 2.6 shows the complex plane colored by polarization for the flux calibrator J0334-4008 (left panel) and for XID 403 (right panel) in EB–1, which has the highest continuum flux among all the detected targets (Section 3.4).

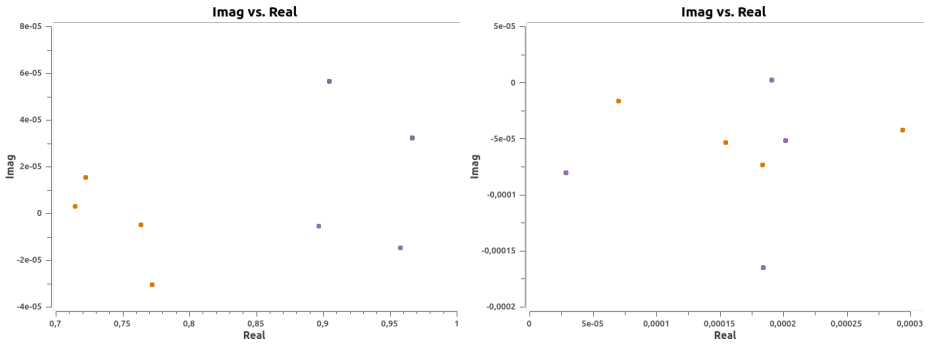

Figure 2.6: Complex plane of the flux calibrator J0334-4008 (left panel) and of XID 403 (right panel) averaged by time, scan, channels and baselines, colored by polarization (EB–1). The reported values are expressed in Jy. Note that the calibrator is clearly detected due to the high real part value, while for the target the real part is only slightly above the zero–level. In addition the different values of the two polarization signals of the calibrator indicates that its emission is polarized.

The flux calibrator is a bright QSO and the real part is far above the zero–level (note that the flux of the two polarizations is quite different, meaning that the emission is polarized, as often observed for synchrotron sources). Despite the strong averaging (in order to increase the SNR as much as possible) the signal of XID 403 is barely shifted towards positive real part values, thus the detection cannot be certainly claimed only on the basis of this plot.

The size and shape of a source influence the intensity of the signal over the baselines length. The FT of a point–like source (such as the calibrators) is a constant function, so we expect that the visibilities have all the same amplitude for all the baseline lengths. For a nearly Gaussian source instead, we expect that the signal decreases toward the longest baseline with a Gaussian trend. In Figure 2.7 we report an example of amplitude versus u–v distance using the flux calibrator (left panel) and XID 403 (right panel), colored by polarization (EB–1).

The calibrator is a point–like source and its polarized emission is constant all over the u–v distance range. The target source instead, presents a more complex trend in which a Gaussian shape is barely recognizable.

2.2.3 Coverage of the *u-v* plane

Since the images of the observed sky regions are reconstructed starting from the visibilities, it is useful to inspect their distribution in the u–v plane

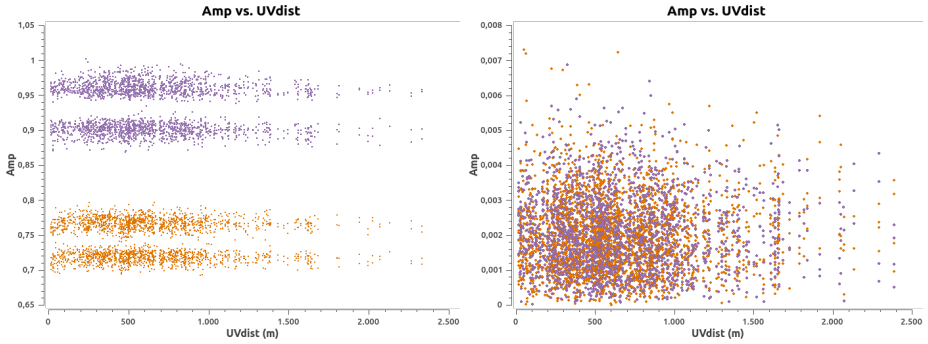

Figure 2.7: Amplitude in Jy versus u–v distance of flux calibrator (left panel) and XID 403 (right panel) averaged for time, scan and channels, colored by polarization (EB–1). Calibrator is a point–like source and its signal is constant over the baseline length range; its emission is polarized (different intensity for the two polarizations) and, since it follows a power–law, for each polarization there are two levels of signal because of the different emission in the two sidebands. In the XID 403 plot the Gaussian source trend cannot be unambiguously distinguished from a simple noise pattern, so we will perform a Gaussian fit in the following, in order to assess if the source is detected and resolved. Note that the visibility density decreases towards the longest baseline, i.e. the longer distances in the u–v plane are less sampled than the shorter.

because we expect that any trend of the visibilities will be reflected in the final image. Thus, if in an image there is an unexpected recognizable pattern such as periodic features, one must check if there is a corresponding signature in the u–v plane, in order to exclude that such a feature is generated by some antennas that should be flagged. In Figure 2.8 an example of u–v plane coverage (left panel) and a corresponding sub–region in the continuum image (right panel) of the phase calibrator J0348–2749 are reported. The visibility distribution results in a partial coverage of the u–v plane with a recognizable pattern; in addition, it is denser in the central region, as we expected from Figure 2.7. This distribution is responsible for the periodic features visible in the image plane, which clearly resembles the visibilities pattern in the u–v plane. Therefore, we can exclude that the periodic features in the image are due to bad signal from one or more antennas that the pipeline procedure did not properly flagged.

2.2.4 Phase and bandpass calibration

In order to assess if the calibration over time and frequency was successful, we have inspected the following diagnostic plots for each execution block:

- Amplitude versus frequency for the bandpass calibrator J0334-4008;
- Phase versus frequency for the bandpass calibrator J0334-4008;
- Amplitude versus time for the phase calibrator J0348-2749;

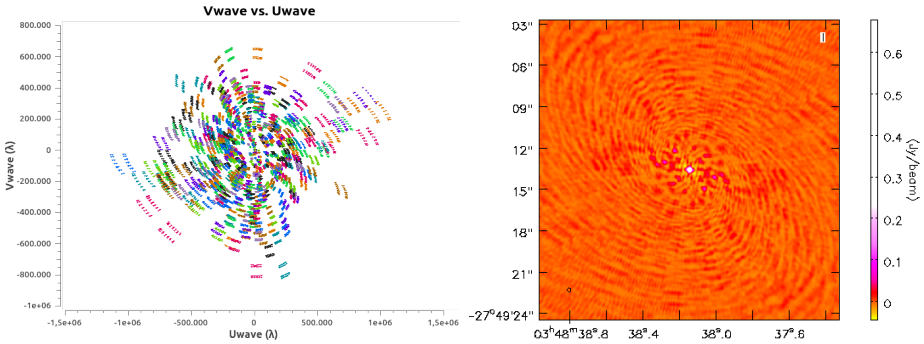

Figure 2.8: Comparison for phase calibrator J0348–2749 between baselines distribution in the u–v plane (in unit of observed wavelength λ), colored by baseline and averaged channels (left panel) and a $\sim$ 30 arcsec^2 squared region in the continuum image (right panel). In the image plane it is recognizable a pattern of the *rms* fluctuations, that resembles the visibilities distribution in the u–v plane.

- Phase versus time for the phase calibrator J0348-2749.

In these plots we looked for possible deviations from the expected behavior described at the end of 2.1. In particular:

- The bandpass calibrator J0334-4008 is expected to have constant amplitude all over the observed frequency range; the only deviation from this trend is a slight slope due to its emission nature (synchrotron) which follows a power–law. In addition, being a point–like source at the center of the phases, we expect that its phase scatters around zero over all the frequencies.

- The phase calibrator J0348-2749 is expected to have constant amplitude all over the observation time, as well as its phase that should scatter around zero.

As an example, in Figure 2.9 the amplitude and phase of the bandpass and phase calibrator are reported, respectively over frequency (top panels) and time (bottom panels), for EB–1, colorized by polarization. After inspection of these plots, we decided that the results were satisfying and no re–calibration was required. The only substantial deviation from the expected trend was an increase of the scatter of the amplitude and phase in frequency towards the edge channels of the spws. This is a well known behavior that would require to cut these channels in order to be corrected, in addition to those already flagged by pipeline; however, this would also result in a loss of signal, so this additional cut should be properly evaluated in cases of poor sensitivity such as ours.

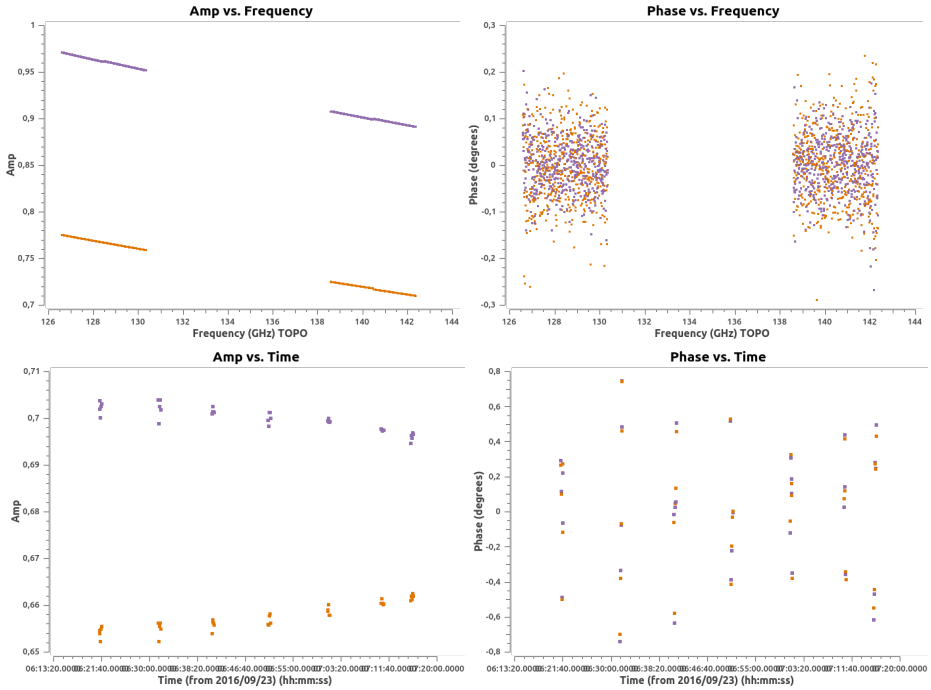

Figure 2.9: Amplitude in Jy and phase vs. frequency for the bandpass calibrator J0334-4008 (top–left and top–right panels) averaged by time, scans and baselines. Amplitude and phase vs. time for the phase calibrator J0348-2749 (bottom–left and bottom–right panels) averaged for channels, spw and baselines. All plots refer to EB–1 and are colored by polarization.
The emission is characterized by different intensities between the two polarizations. As expected for point–like bright sources, the amplitude is nearly constant both in frequency and time; the emission of J0334-4008 presents an overall slope in frequency due to its power–law nature. The emission of J0348-2749 shows a slight intrinsic variability from the start to the end of the observation. The phase scatters around zero both in frequency and time.

2.2.5 Flux calibration

The flux calibration relies on the accuracy of the input parameters used to model the calibrator emission. In our case J0334-4008 is a point–like source so its model is simple and consists of two input parameters: the phase is set equal to zero and a constant value of flux is assumed. This value is based on periodically measured flux of the calibrator in all the ALMA bands, since the emission is expected to change over the cycle observation time–scale, due to intrinsic variability of the source. We found that an observation of J0334-4008 was performed in Band 3 on 2016-09-22, one day before the SB–1 observations and few days before SB–2. Thus, we extrapolated the flux for Band 4 from these measures and compared it with the value used by the pipeline during our flux calibration.

There are two available measures for the flux of J0334-4008 from the

Band 3 observations performed in September 22$^{\text{th}}$ 2016:

- $S_1 = 1.07$ Jy at $\nu_1 = 91.5$ GHz
- $S_2 = 1.01$ Jy at $\nu_2 = 103.5$ GHz

Since the emission comes from synchrotron processes, it is described by a power–law $S \propto \nu^{\alpha}$, where α is the spectral index that can be derived from the ratio of the two measured fluxes:

$$\frac{S_1}{S_2} = \left(\frac{\nu_1}{\nu_2}\right)^{\alpha} \Rightarrow \alpha = \frac{\log\left(\frac{S_1}{S_2}\right)}{\log\left(\frac{\nu_1}{\nu_2}\right)}$$

We found a spectral index $\alpha = -0.47$; we can simply calculate any flux S_0 at a given ν_0:

$$S_0 = S_1 \left(\frac{\nu_0}{\nu_1}\right)^{\alpha}$$

We have considered the central frequencies of the two SBs and compared the derived flux with the input flux used by the pipeline; as central frequencies we assumed the mean of those of all spws, whereas S_{in} is the mean value of the four input parameters (one for each spw) used in the model:

SB–1: $S_0 = 0.894$ Jy at $\nu_0 = 134.45$ GHz; $S_{in} = 0.837$ Jy

SB–2: $S_0 = 0.873$ Jy at $\nu_0 = 141.03$ GHz; $S_{in} = 0.808$ Jy

The discrepancy between S_0 and S_{in} at both frequencies is $\lesssim 8\%$, so we decided that the data do not need to be re–calibrated. A conservative 10% of calibration error will be added quadratically to the rms of our flux density measurements to hold for flux density calibration uncertainties.

Chapter 3

Data analysis

In this chapter I will present the analysis of the ALMA data presented in Chapter 2. We initially perform *imaging* for both line and continuum emission, then we fit the images in order to derive the flux densities and angular sizes of the sources, separately for the molecular gas and dust component.

Since the reconstructed images depend on the deconvolution algorithm and its input values, they do not provide an unique and direct representation of the data but rather a non–linear mapping from the Fourier domain into the sky plane. Hence, we will use the values obtained from the images just as starting input parameters to perform the fits directly on the visibilities, which are unaffected by the reconstruction algorithm and pixel correlation as images are. In addition, if the sources are not or barely spatially resolved, the visibility fitting provides a better estimate of their angular than the fit performed on the images.

We will use these measurements and images in Chapter 4 to derive dust and gas masses, physical sizes and densities, and then we will discuss their morphology and kinematics.

3.1 Imaging

The imaging algorithm reconstructs the image from the visibilities. During an observation we actually sample the u–v plane at discrete points (Figure 2.8, left panel), so the observed visibilities can be written as:

$$V_{obs}(u,v) = S(u,v) \cdot V_{real}(u,v)$$

where $S(u,v)$ is called *sampling function* and it is equal to 1 where visibilities are measured and 0 elsewhere, so that $V_{obs}(u,v) = V_{real}(u,v)$ only at the points where data are actually taken. Applying the convolution theorem the FT of the sampled visibilities (i.e. the measured sky brightness) is equal to the true sky brightness convolved with the FT of the sampling function (called *dirty beam*):

$$B_{obs}(x, y) = D(x, y) \otimes B_{real}(x, y)$$

In order to derive the true brightness of a source we need to deconvolve the FT of the sampled visibilities (called *dirty image)* by the dirty beam. This process is called *cleaning* and consists in the following steps:

- perform a Fast Fourier Transform (FFT) in the Fourier domain to obtain an initial image called *dirty image* and initialize it as the first *residual map.*
- Generate a *cleaning list* in which the pixel corresponding to the maximum intensity is added.
- The value added to the cleaning list is convolved with the dirty beam and subtracted from the residual image, generating a new residual image.
- The previous two steps are iterated finding each time the pixel corresponding to the peak of intensity, until a given number of steps, a threshold (usually set equal to the theoretical noise level or to one of its multiplies) or a gain between two consecutive peaks of intensity are reached.
- The components of the cleaning list are multiplied by a Gaussian fit of the dirty beam, called *clean beam*, and added to the residual map obtaining the *clean image.*

Finally, since the response of the antenna (*primary beam*) is not constant all over the FoV (in particular it decreases towards the outskirts of the field), the clean image needs to be corrected as a function of the angle from the main axis.

The cleaning task has various operative modes, among which there is one used for continuum emission called multi–frequency synthesis (*mfs*) and one for lines. The first mode returns a single image in which each pixel has a brightness value averaged over the native visibility channels spanning the observed frequency range; it is also possible an averaging over the binned image channels which are no longer independent each other, but that option has not been used in this work. The second mode results in a datacube, whose channels are given in frequency or velocity that can be binned with respect to the native 7.812 MHz value (Section 2.1) to increase the SNR per channel. In each channel the pixel value corresponds to the averaged signal over the channel width. The brightness is given in Jy/beam, since every pixel is convolved with the beam. A graphical representation of the datacube is shown in Figure 3.1.

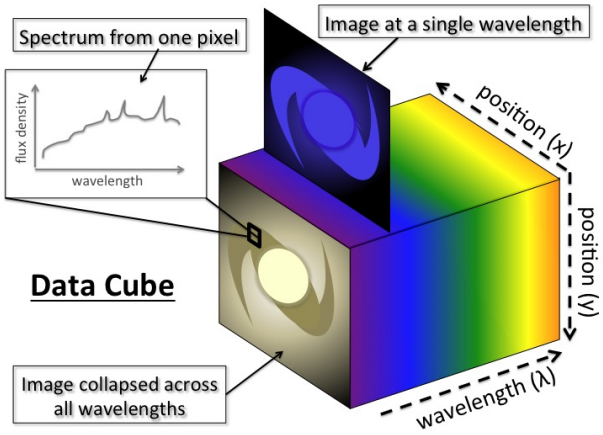

Figure 3.1: Graphical representation of the datacube derived from imaging in frequency/velocity mode. For each pixel the intensity is a function of wavelength and there is an image for each channel, whose width determines the spectral resolution and the rms (see text for details).

In order to produce an image we need to assign a proper angular scale to the pixels. The angular resolution of an interferometer is given by $\theta_{res} = \frac{\lambda_{obs}}{B_{max}}$ where λ_{obs} is the observed wavelength and B_{max} is the maximum baseline. In order to properly reconstruct the image we oversample the resolution by a factor of 4, choosing a pixel scale equal to $\theta_{res}/4$. In addition we need to set an image size in pixels. The FoV is given by $\frac{\lambda_{obs}}{D}$ where D is the single dish size (equal to 12 m for the ALMA extended array) and the image size is equal to the ratio between the FoV and the pixel scale. Usually this value is approximated to the closest power of 2 which makes the FFT algorithm to work considerably faster; we chose 512 pixels as image size for all the following images.

The theoretical noise level of an image in terms of root mean square (rms) can be written as:

$$rms = \frac{2k_B\ T_{SYS}}{A_{eff}\sqrt{\Delta t\ \Delta\nu\ n_p\ N_{ant}(N_{ant}-1)}}$$

where k_B is the Boltzmann constant, A_{eff} is the effective area (calculated multiplying the geometrical area by the aperture and instrumental efficiency[1]), N_{ant} is the number of antennas, Δt is the total time of observation on source, $\Delta\nu$ is frequency bandwidth and n_p is the number of polarizations; note that for a continuum image $\Delta\nu$ corresponds to the sum of total bandwidth (1.875 GHz) of each imaged spw, while for the line emission (datacube) $\Delta\nu$ is equal to the spectral range corresponding to the single image of the cube, i.e. the

[1]The aperture efficiency is given by the Ruze equation: $\eta_{eff} = R_0 \exp(-\frac{16\pi^2\sigma^2}{\lambda^2})$ where $R_0 = 0.72$, σ is the rms surface accuracy of the antenna and λ is the observed wavelength. The instrumental efficiency for ALMA is 0.845 (Asayama et al., 2017).

channel width. Thus we expect that for the CO the theoretical noise will be larger than for the continuum. The expected rms can be easily calculated using the sensitivity calculator tool[2] and set as a threshold parameter during the cleaning procedure as described above. If the cleaning algorithm does not converge one may increase the threshold to a larger value usually set equal to a multiple of the rms.

A crucial criterion in data imaging is the *weighting* $W(u, v)$, i.e. which weight to assign to each baseline. The different weightings are:

- Natural: $W(u, v) = 1/\sigma^2$, where σ is the baselines variance in the u–v plane. Since the central region of the u–v plane is more populated than the outskirts (Figure 2.8), this specification assigns a larger weight to the shortest baselines with respect to the longest. Hence, this choice increases the sensitivity but minimizes the angular resolution.

- Uniform: $W(u, v) = 1/\delta$ where δ is the space density of the baselines in a symmetric region of the u–v plane. The uniform weighing assigns the same weight to the longest and the shortest baselines, resulting in the best angular resolution, at the cost of the sensitivity.

- Briggs: this weight, developed by Briggs (1995), represents a compromise between natural and uniform. It relies on a so–called *robust* parameter that spans from -2 (corresponding to uniform weighting) to 2 (corresponding to natural weighting).

An additional weighting during imaging can be performed using *tapering*: in this procedure the weight of the visibilities is multiplied by a Gaussian function, resulting in a further increase of the weight associated with either the shortest (outer tapering) or the longest (inner tapering) baselines. In the case of outer tapering (used in this work) the effect is a smoothing of the image with a significant improvement of the sensitivity and degradation of resolution.

The task of CASA that performs the imaging is named *clean*; In the following a brief description of the used task parameters is reported.

- **vis**: name of input visibility file.

- **imagename**: name of the output image.

- **mode**: type of imaging. For the continuum it is set equal to 'mfs', whereas for the line the available keys are 'channel', 'velocity' or 'frequency', depending on which is the chosen unit for the third axis of the datacube.

[2] https://almascience.eso.org/proposing/sensitivity-calculator

- **outframe**: spectral reference frame of the output image. We always set it equal to 'BARY' for a barycentric frame.

- **interactive**: if this parameters is set to 'True', the cleaning task allows to draw a region in the dirty image in which the task will search for the peaks; this procedure helps the algorithm in finding the peaks in a region properly chosen to contain the source and eventually improves the final result. Then it runs for a number of iterations given by the **niter** parameter before offering the possibility to reset the region and rerun the cleaning, or to just end it up. If it is set to 'False' the cleaning task runs until the lower flux limit given by the **threshold** parameter is reached. This threshold is set equal to the expected rms, and if the algorithm does not converge it is increased to a larger value, usually 3 or 5 times the rms.

- **weighting**: available keys are 'natural', 'uniform' and 'briggs' as described above.

- **uvtaper**: it allows to perform tapering as described above. It takes as input the FWHM of the Gaussian function.

- **spw**: indicates which spectral windows in the dataset have to be taken into account during imaging. For each spw it is also possible to consider only a subset of visibility channels.

- **cell**: pixel size in arcseconds.

- **imsize**: image size in pixels. We chose a size of 512 pixels for all the images of this work.

- **restfreq**: available only for line imaging modes. It sets the rest frequrency of the line in order to properly individuate the zero–velocity channel.

- **width**: available only for line imaging modes. It sets the width in velocity/frequency of each channel of the datacube.

Finally, we apply the primary beam correction to the produced image by means of *impbcor* task, which takes as input the following keys:

- **imagename**: name of the input image.

- **pbimage**: name of the primary beam file to apply, generated during imaging.

- **outfile**: name of the output image corrected for the primary beam.

From the datacube it is possible to extract the maps of moments of the pixels. (Figure 3.2). The so–called moment maps result from collapsing the datacube in a single image and calculating for each pixel the moments of its distribution, that contain information about gas emission and kinematics. The main available moments are described in the following, in the case the channels of the image were derived in velocity mode such as in this work. An analogous definition can be adopted if the datacube third axis is given in channels or frequency.

- Moment 0:

$$S = \int S_v \, \mathrm{d}v$$

  where S_v is the flux density per channel. It corresponds to the total line emission integrated over a specified velocity range and is expressed in Jy km s^{-1}.

- Moment 1:

$$< v >= \frac{\int S_v \; v \; \mathrm{d}v}{\int S_v \; \mathrm{d}v}$$

  where v is the velocity of each channel. Moment 1 is the velocity field and each pixel value is expressed in km s^{-1}.

- Moment 2:

$$< v^2 >^{\frac{1}{2}} = \sqrt{\frac{\int S_v (v - < v >)^2 \mathrm{d}v}{\int S_v \mathrm{d}v}}$$

  is the velocity dispersion field, reported in km s^{-1}.

The moments are extracted from the datacube running the *immoments* task which takes the following parameters:

- **imagename**: name of the image datacube from which the moments are extracted.

- **outfile**: name of output moment file.

- **moments**: moment(s) type to extract.

- **includepix**: this key allows the definition of a range of the flux density to consider during moment extraction. It is useful to set a lower (and eventually upper) threshold to a given significance level, usually set equal to a multiple of the rms.

- **chans**: channels of the datacube to take into account.

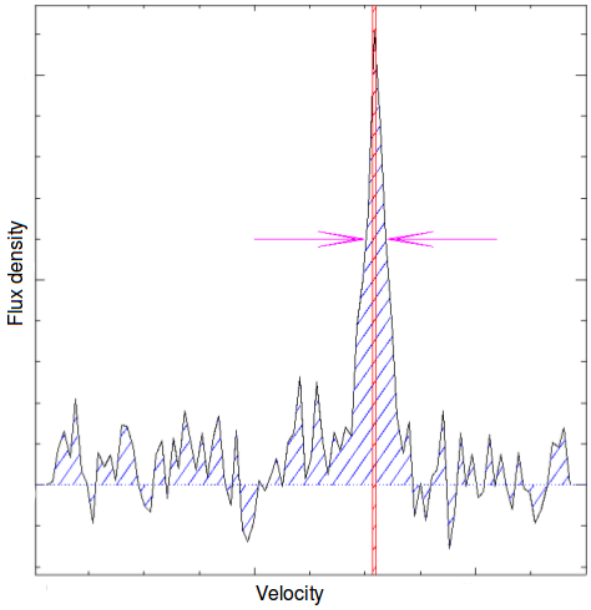

Figure 3.2: Graphical representation of the three moments calculated in this work: the area filled with blue solid lines is the Moment 0 and is equal to the integrated flux, the red vertical bar corresponding to the peak of the line is the Moment 1 and the magenta arrows indicates the line width, i.e. Moment 2.

If the line is not clearly visible from the visibilities inspection, we cannot unambiguously assess the channels containing it, thus we cannot a priori exclude them when we image the continuum emission. In such cases it is better to image separately the spw containing the line and the other spws, in order to avoid a possible contamination of the line in the continuum image.

To image a line we firstly need to subtract the continuum from the dataset. The procedure performs a polynomial fitting of the continuum level and then subtracts it from the data. As stated above we do not know exactly the channels corresponding to the line, so we decide to not consider the entire spw containing it, and fit only the other spws. The calculated continuum level will be then subtracted to all spws, including that with the line. This procedure excludes the possibility to overestimate the continuum level, that would result, after the subtraction, in a loss of signal of the line. The task used to subtract the continuum is *uvcontsub* set by the input key:

- **vis**: name of input visibility file.

- **fitspw**: spws to fit in the dataset.

- **combine**: if this key is set to 'spw' all the specified spws are combined to perform the fitting.

- **fitorder**: the polynomial order to fit. In this work it is always set to 1, i.e. we perform a linear fitting.

In the following Table 3.1 we report the spws containing the line for each source, as well as the line rest–frame and observed frequencies. Since there are four spws for each scheduling block (Table 2.2), the spws used for continuum fitting and subtraction are the three not mentioned in this table.

XID	CO line	$\nu_{rest}(GHz)$	$\nu_{obs}(GHz)$	spw
262	6-5	691.47	148.38	0
412	6-5	691.47	147.12	0
34	5-4	576.27	146.37	1
403	7-6	806.65	140.16	0
546	5-4	576.27	141.80	1
490	4-3	461.04	128.85	3

Table 3.1: CO line transition for each source with the corresponding rest–frame and observed frequency and the spw containing it.

3.2 Line imaging of the targets

We can now proceed to the line imaging. The best parameters set for each source, mainly regarding the best trade–off between sensitivity and angular resolution, is shown in Table 3.2, as well as the expected rms used as lower threshold. Different weighting can be used to improve either the sensitivity or the resolution and thus increase the significance of the detection or highlight some structural features of the sources. Note that for XID 262, XID 412 and XID 546 (the faintest sources in the sample) natural weighting and tapering have been applied to increase the sensitivity at its maximum and possibly achieve a significant detection. The table also reports both the theoretical rms value used to determine the threshold for the imaging algorithm, that has been set to 3σ for all the sources.

In Figure 3.3 the images corresponding to the peak channel of the datacubes are reported. For XID 262, XID 412 and XID 546 it was not possible to determine unambiguously a channel in which the brightness at the center of the field was clearly above the noise level, so we report the channel enclosing the rest–frame velocity, which is the most likely to contain the peak of the line emission, given the secure spectroscopic redshift. For XID 34, XID 490 and XID 403 it has been simple to identify the channel corresponding to the peak of emission. Note that only for XID 403 the velocity of the peak channel is consistent with zero (the channel central velocity is -111.6 km/s and its width is 120 km/s).

XID	Δv (km/s)	px size (")	weighting	robust	tapering (")	$\mathrm{rms_{th}}$ (mJy)
(1)	(2)	(3)	(4)	(5)	(6)	(7)
262	120	0.03	Natural	–	0.45	0.3
412	120	0.03	Natural	–	0.45	0.3
34	40	0.04	Briggs	0.5	–	0.3
403	120	0.03	Briggs	1	–	0.3
546	120	0.03	Natural	–	0.45	0.2
490	40	0.04	Briggs	1	–	0.5

Table 3.2: Imaging parameters for each source. Columns from left to right: (1) Source ID. (2) Channel width in velocity. (3) Pixel size in arcseconds, obtained by oversampling by a factor of 4 the theoretical angular resolution. (4) Weighting type. (5) Robust value for Briggs weighting. (6) FWHM of the Gaussian function used for tapering, expressed in arcseconds. (7) Theoretical noise per channel used to set the imaging threshold to 3σ.

XID 490 has two peaks shifted respectively by ∼-200 km/s and ∼150 km/s; we will discuss later the double–peaked feature (see Figure 3.4) centered on the rest–frame velocity, that is interpreted as a rotating structure signature.

The peak of XID 34 is shifted by ∼500 km/s with respect to the rest–frame velocity. No clear features of rotation can be identified from the spectrum. Given this velocity shift we checked if the redshift estimate of z=2.940 (Vito et al., 2013) derived from the optical spectrum was actually correct. This redshift was derived from the Ly–α line, which is known to be challenging as exact redshift estimator due to the extinction that affects the bluer part of the line. We therefore used the CIV, HeII and NV lines, that are present in the UV spectrum and derived and average redshift of z=2.937. This correction cannot explain by itself a velocity shifting as the one observed. We will discuss in Chapter 4 the possible causes of this shift and its implications for the nature of the source. The reported image and spectrum have been derived after correcting the source redshift.

We calculate the SNR of the line detection as the ratio between the brightness value of the maximum pixel (approximately corresponding to the centroid of the region in which the spectra were extracted, highlighted by the blue ellipses in Figure 3.3) and the rms, which has been derived averaging the rms measured in four regions placed in the corners of the image of the peak channels. The measured values are reported in Table 3.3. For XID 412 and XID 546 we do not report a maximum pixel since there are no pixels above the 3σ level that are reasonably close (within ∼1.5") to the center of the field. We still report their rms that can be used to derive an upper limit to their flux density.

We detect XID 34, XID 403 and XID 490 with a SNR > 4: in addition, see the central position of the peak in the images (offset < 0.5", Figure 3.3) and the line feature in the spectra visible in Figure 3.4 (note the double peak of XID 490). Although XID 262 has a high SNR there are several indications

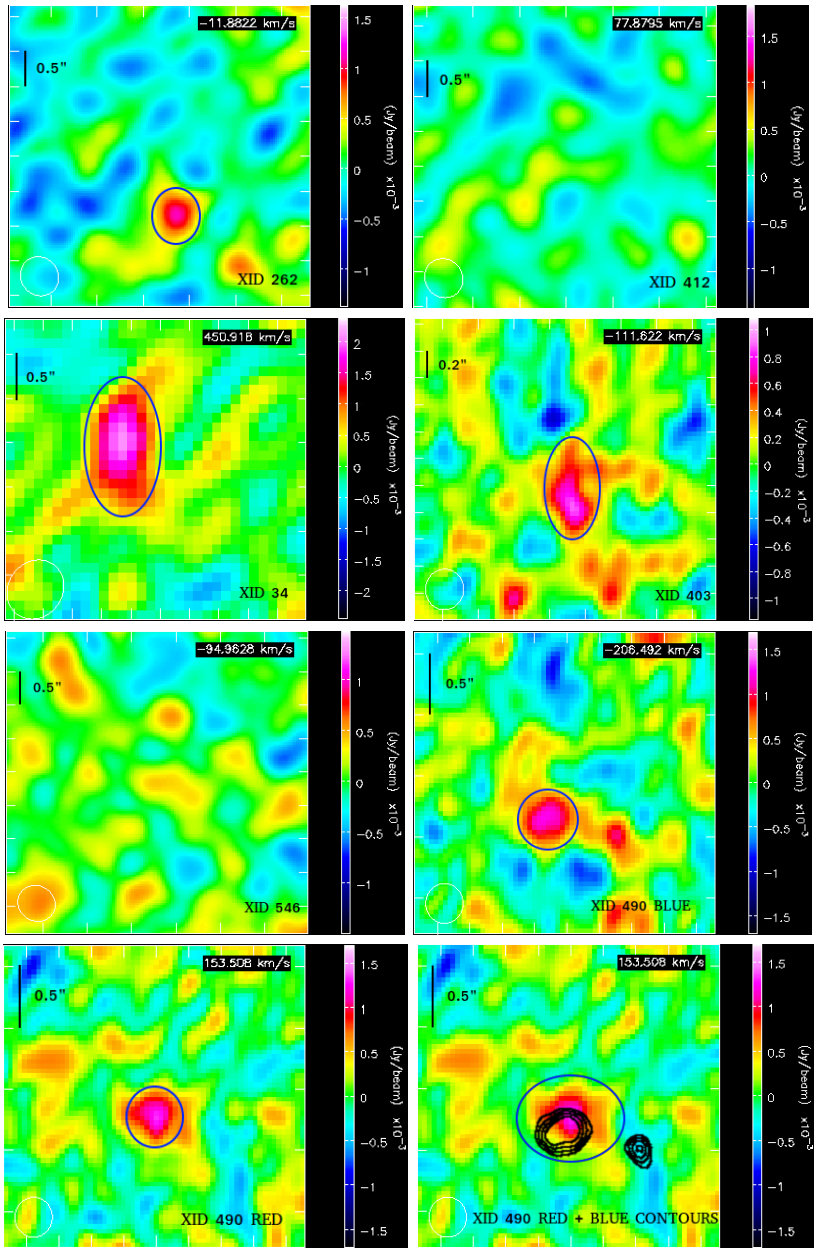

Figure 3.3: Peak channel of the datacube for each source. Angular scale, source ID and velocity corresponding to the center of the channel are reported on the images. The white ellipse in the left bottom corner represents the clean beam. The blue ellipses are the regions from which the spectra in Figure 3.4 were extracted. Note that for XID 490 three images are shown: those labeled as XID 490 BLUE and XID 490 RED correspond to the blue and red–shifted peaks respectively, while the third one shows the blue–shifted contours (black solid lines) over the red–shifted peak channel.

that it is just a fluctuation of the noise: the closest emission peak is shifted by

XID	Max pixel (mJy/beam)	rms (mJy/beam)	SNR
262	1.11	0.27	4.1
412	–	0.26	–
34	2.10	0.34	6.2
403	0.89	0.19	4.7
546	–	0.28	–
490_B	1.21	0.31	4.0
490_R	1.33	0.27	4.9

Table 3.3: For each source the maximum brightness (measured on the maximum pixel value in the peak channel), the rms and the SNR are reported. XID 490_B and XID 490_R stand for the blue–shifted and the red–shifted peaks.

$>$ 1" from the field center and the value of its maximum pixel is comparable to (or even lower than) other pixels in the whole field of view, both in the same channel (see Figure A.1, Appendix A) and in the others. In addition, in its spectrum there is not a clear feature in the channel range around the peak indicating the presence of a line (Figure 3.4). We then conclude that for XID 262 there is not an unambiguous detection of the CO line.

3.2.1 Moments

We now proceed to compute the moments 0, 1, 2 for the detected sources. We firstly show the spectra of those sources with a clear line feature (i.e. XID 34, XID 403 and XID 490) and XID 262 to exclude the presence of a line as discussed above. The spectra are reported in Figure 3.4 and they were extracted in the regions indicated by the blue ellipses in Figure 3.3.

We report three spectra for XID 490, that has a double–peaked line. Indeed, since the two peaks also correspond to two spatially different regions, we decide to extract and plot the spectra separately in these two regions. Furthermore, we also extract the spectrum for the whole source in order to look at the total emission of the CO line and highlight its double–peaked nature.

To extract the moments (and later perform the fits on the images and visibilities), we firstly need to define a range in velocity that contains them. This range should include few channels aside the line in order to avoid the loss of signal from its wings. Hence, we perform a Gaussian fitting of the lines and derive their center v_0 and Full Width Half Maximum (FWHM); to calculate the moments we consider a velocity range given by $v_0 \pm \mathrm{FWHM}$.

The results of the fitting are reported in Table 3.4, while in Figure 3.5 we show the Gaussian fits superimposed to the spectra focused on the lines.

The two peaks of XID 490 are quite close and likely contaminated by each other. In order to estimate such contamination and derive the most

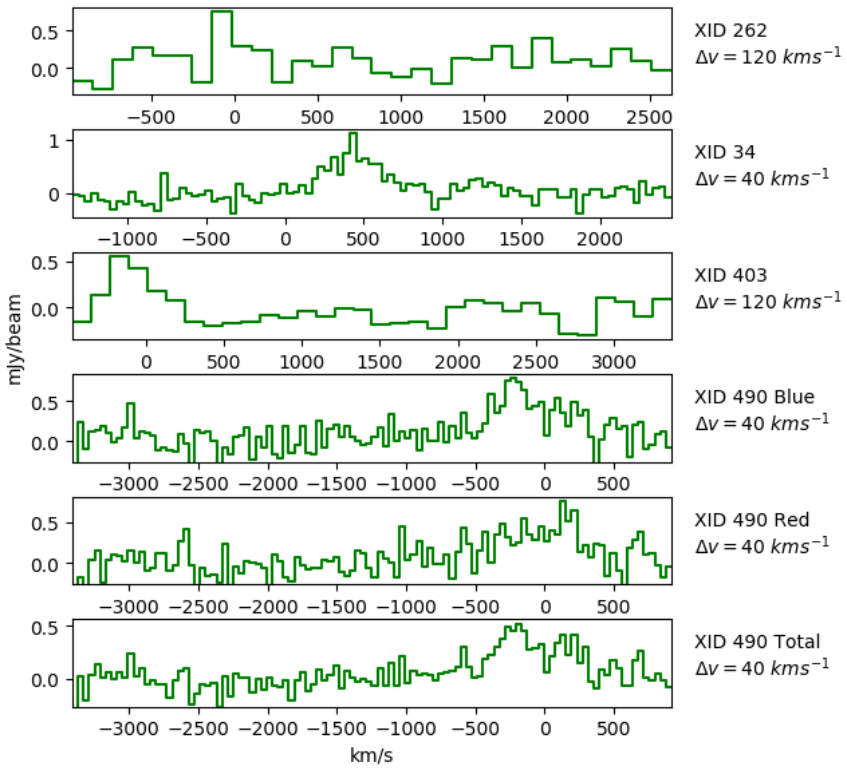

Figure 3.4: Spectrum of XID 262, XID 34, XID 403 and XID 490, extracted in the regions contained in the blue ellipses of Figure 3.3. For each source the channel width Δv is indicated on the right side. The brightness on the y–axis expressed in Jy/beam is the average within the extraction regions. For XID 490 three spectra have been extracted: XID 490 Blue refers to the blue–shifted peak region, XID 490 Red to the red–shifted one and XID Total to the whole source region.

accurate line width, we have performed fitting with a single Gaussian component on the spectra of the two spatially separated regions corresponding to the peaks, and another fit with two Gaussian components on the whole source region, then we compare them. This allows us to check the robustness of such values and their dependence upon the region of extraction. Both the line width and central velocity of the single blue and red shifted regions are fully consistent (within 1σ) with those of the two components derived from the entire source. In the following we will use the line width and central velocity derived from the two Gaussian components fitted on the whole region.

We are now ready to extract the moments using the *immoments* task described above. As a threshold we use a value of 3σ calculated by the measured rms reported in Table 3.3, as for the channel ranges, we use those reported in Table 3.4. For XID 490, to calculate the moments of the entire source, we consider the channel range spanning from the minimum of the blue

XID	v_0 (km/s)	FWHM (km/s)	Δv (km/s)	Δv (Channels)
34	498 ± 14	368 ± 32	100 – 836	36 – 56
403	-56 ± 33	308 ± 77	-364 – 252	1 – 6
490_B	-205 ± 28	403 ± 49	-608 – 198	70 – 90
490_R	174 ± 14	173 ± 39	-1 – 347	85 – 94
490(Blue c.)	-194 ± 26	474 ± 67	-668 – 280	68 – 92
490(Red c.)	187 ± 12	162 ± 27	25 – 349	86 – 94

Table 3.4: Results of the Gaussian line fitting performed on the spectrum of each source. From left to right: central velocity, FWHM, velocity range calculated as $v_0 \pm$ FWHM in km/s and the corresponding channel range. For XID 490 we report the fits resulting from the two separate line region (490_B for the blue–shifted and 490_R for the red–shifted) and the two components fitted simultaneously on the whole source region, that are named 490(Blue c.) and 490(Red c.).

component (68) to the maximum of the red component (94). In Chapter 4 we will also extract the moments separately for each shifted line to highlight the rotational structure of the source. Moments are reported in Figure 3.6.

3.3 Continuum imaging of the targets

For each source we have imaged all the spws but those containing the line reported in Table 3.1. We report the pixel size, weighting setup and theoretical rms in Table 3.5. Note that the theoretical rms is one order of magnitude lower than that of the line, due to the larger bandwidth that includes three spectral windows.

XID (1)	px size (") (2)	weighting (3)	robust (4)	tapering (") (5)	$\mathrm{rms_{th}}$ (mJy) (6)
262	0.03	Natural	–	0.45	0.03
412	0.03	Natural	–	0.45	0.03
34	0.04	Briggs	1	–	0.03
403	0.04	Briggs	1	–	0.02
546	0.04	Natural	–	0.45	0.03
490	0.04	Briggs	1	–	0.03

Table 3.5: Imaging parameters for each source. Columns from left to right: (1) Source ID. (2) Pixel size in arcseconds, obtained by oversampling by a factor of 4 the theoretical angular resolution. (3) Weighting type. (4) Robust value for Briggs weighting. (5) FWHM of the Gaussian function used for tapering, expressed in arcseconds. (6) Theoretical noise used to set the imaging threshold to 3σ.

We report the continuum images in Figure 3.7.

We measure the value of the maximum pixel and the rms similarly to what has been done for the line images, in order to estimate the SNR. These

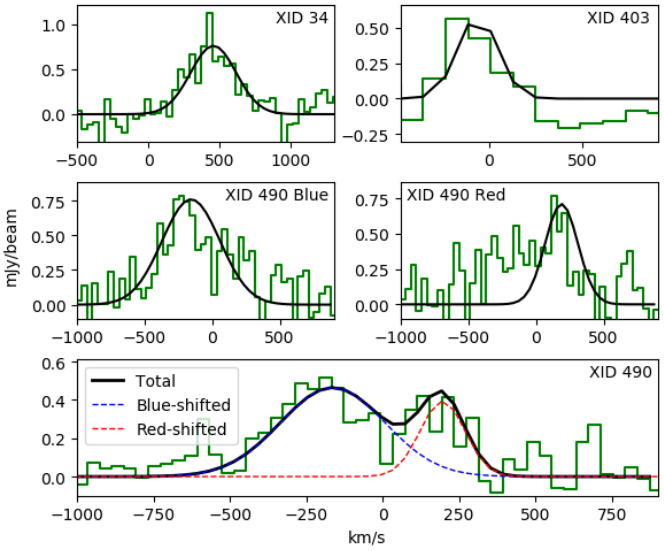

Figure 3.5: Gaussian line fitting (black solid line) for XID 34, XID 403 and XID 490, superimposed to their spectra (green solid histogram). We report three fits for XID 490: two single Gaussian components used separately in the blue–shifted and red–shifted peak regions (indicated respectively with XID 490 Blue and XID 490 Red), and one double component performed on the total source region (simply named XID 490). In this case the two components are represented by the blue and red dashed line.

values are reported in Table 3.6. For XID 412 and XID 546 we report only the rms since they are clearly undetected as evident from the images. XID 262 image shows a region with SNR > 5 at an offset $\sim$2" from the center field, but it is comparable to other features which are visible in outskirt of the image (see Figure A.2, Appendix A) and thus it is considered noise; therefore, we decide to report only the rms also for this source.

XID	Max pixel (mJy/beam)	rms (mJy/beam)	SNR
262	–	0.026	–
412	–	0.026	–
34	0.130	0.019	6.8
403	0.271	0.021	12.8
546	–	0.023	–
490	0.155	0.020	7.0

Table 3.6: Maximum pixel, rms and SNR for the detected sources XID 34, XID 403 and XID 490. For the other undetected sources only the rms is reported.

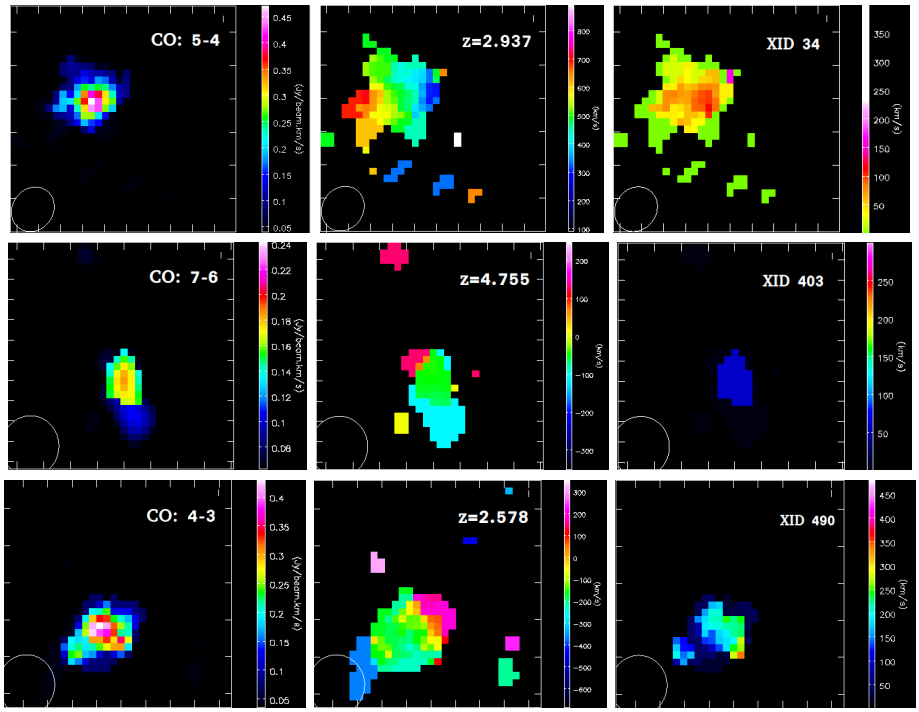

Figure 3.6: Moments 0, 1 and 2 (from left to right) extracted for XID 34, XID 403 and XID 490 (from top to bottom). In the image of moment 0 the CO transition is reported, while in the images of the moment 1 and moment 2 we have indicated the source redshift and ID respectively. Only the pixels that are three times the rms reported in Table 3.3 are shown. The size of each image is $\sim$ 2.7" on a side.

3.4 Data fitting

In this section we will finally perform data spatial fitting in order to extract the flux densities and angular sizes of the detected sources: XID 34, XID 403 and XID 490. We will initially perform fitting on the images and later use the obtained values to calculate the input parameters for the visibility fitting. To derive the information about the dust component we will fit the continuum image, while for the gas we will fit the moment 0 of the CO emission image since it represents the total integrated emission.

3.4.1 Image fitting

To estimate the flux density and size we will fit a spatial elliptical Gaussian 2–D function to the images using a task of CASA called *imfit* which relies on the algorithm developed by Condon (1997), that we briefly describe in the following.

The general equation of a 2–D elliptical Gaussian can be written as

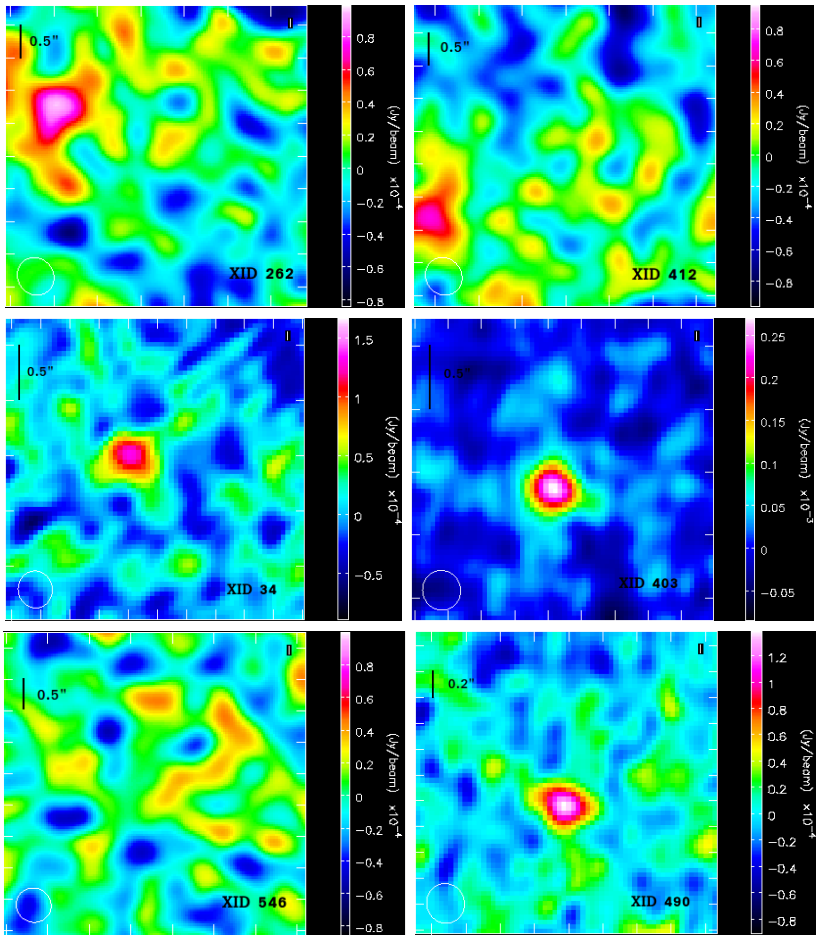

Figure 3.7: Continuum image for each source. Angular scale and source ID are reported on the images. The white ellipse in the left bottom corner is the clean beam.

$$G(x,y) = A \exp\left[-\frac{(x-x_0)^2}{2\sigma_x^2} - \frac{(y-y_0)^2}{2\sigma_y^2} - \frac{\beta(x-x_0)(y-y_0)}{\sigma_x\sigma_y}\right]$$

which depends on six p_i parameters: A is the peak amplitude (in our images expressed in Jy/beam for the continuum and Jy/beam $\cdot$ km/s for the moment 0 of the line), (x_0, y_0) is the central position, σ_x and σ_y are the rms length of the major and minor axes (that are related to the FWHMs by the relations $\theta_M = \sqrt{8\ln 2}\sigma_x$ for the major axis and $\theta_m = \sqrt{8\ln 2}\sigma_y$ for the minor axis) and β is an adimensional parameter measuring the position angle of the axes of the Gaussian with respect to the image pixel coordinates (x, y) axes.

Under the assumption that the image is composed by m independent amplitude a_k (i.e. each pixel value) having a Gaussian error distribution

with the same rms μ (we know that pixels are not independent each other and we will later account for their correlation) the maximum–likelihood fit is the one minimizing the χ^2 function

$$\chi^2 = \sum_{k=1}^{m} \frac{[a_k - G(x_k, y_k)]^2}{\mu^2}$$

where (x_k, y_k) are the coordinates of the $k-$th pixel with amplitude a_k. Note that the rms μ used during the fitting is crucial: if not specified the task takes automatically the rms inside the fitted region, which is typically above the rms that we measured in the outskirts of the field if it contains the source. Thus, during the fitting we will fix the rms values to those measured and reported in Table 3.3 for the line and Table 3.6 for the continuum. If the image plane is spatially sampled at points equally spaced (which, in our images, corresponds to the pixel size) it can be demonstrated that is possible to calculate the variance of any of the six parameters as a function of the others. However, to account for the pixel correlation, they need to be convolved with a smoothing function (actually, the clean beam), which leads the pixel area to be replaced with an effective pixel area. The smoothing function, for a nearly circular Gaussian, is specified by its FWHM θ_N. The relation between the θ_N and θ_M,θ_m sets the threshold above which the correlation between pixels can no longer be ignored: the more θ_N approaches θ_M,θ_n the more the assumption of uncorrelated noise breaks down. Hence, the value of θ_N is crucial to set whether the *imfit* task should consider correlated or uncorrelated noise. If a value is specified, the noise will be considered correlated if θ_N is larger than the pixel size. If it is not specified and a clean beam is present in the image dataset, its FWHM will be used as θ_N, otherwise uncorrelated noise will be assumed. Since in our images a clean beam is always present, we do not specify θ_N and let the task automatically take the clean beam FWHM as its input value.

The *imfit* takes the following parameters:

- **rms**: the rms used to compute the uncertainties of the fit. We set it equal to the measured values reported in Table 3.3 and Table 3.6.

- **includepix**: range of values of the pixels to be considered during the fit. We will use it to set a lower threshold equal to three times the rms during continuum fitting. We will not set it for the line emission, since we will fit directly the moment 0 that we have already extracted adopting a 3σ threshold.

- **region**: region within the image in which the fitting will be performed. It should be considerably larger than the source but not too much, otherwise other spikes or features not related to it will be included.

Whereas for the moment 0 this is not a issue because all the included pixels are above the 3σ significance level and are attributed to the source, for the continuum emission the chosen region can significantly affect the fit results. However, the high SNR of the detected sources in our case guarantees that if we set a 3σ threshold with **includepix** only the source will be fitted. Thus, we chose a region relatively large ($\sim$1.5" diameter) around the sources to include all their signal.

It is also possible to provide the fitting with values that will be used as a starting guess: peak expressed in Jy/beam for the continuum and in Jy/beam $\cdot$ km/s for the moment 0, x and y coordinates of the pixel corresponding to the peak, major axis, minor axis, and position angle. We provided the fit with the peaks intensity and position measured on the images.

The fits returns the celestial and pixel coordinates of the Gaussian peak and its value, the major and minor axis FWHM of the clean beam, the major and minor axis FWHM of both the convolved and deconvolved Gaussian fit, the position angle, the spatially integrated flux density expressed in Jy for the continuum and the spatially integrated flux in Jy $\cdot$ km/s for the moment 0. To derive the starting values for the visibilities fitting, we are interested in the flux density, deconvolved size, position angle and celestial position of the Gaussian fits. We report the position as the RA and Dec offset calculated with respect to the center of the field, since those are the parameters taken as input by the visibilities fitting algorithm. The fit results are shown in Table 3.7.

The large error associated with the position angle is due to the fact that the sources are barely resolved and the fits are nearly circular, so it is difficult to unambiguously derive an orientation of the 2–D Gaussian function. This large uncertainty is still present in the following visibilities fitting, and so the derived position angle is poorly constrained. However, this does not affect our analysis since we are interested in the size of the sources and not in their orientation with respect to the celestial axes.

3.4.2 Fitting in the visibility plane

We now proceed to fit directly the visibilities. These are not affected by correlation as image pixels do and their fitting algorithm is simpler than that of the images. To fit a sky model to the visibilities plane, the Fourier transform of the intensity distribution of such a model (weighted by a Gaussian approximation of the antenna primary beam) is computed at the u and v coordinates of the baselines. These coordinates are given in units of the observing wavelength. The values of the Fourier transform, computed for each baseline, time, and frequency channel, are taken as the model visibilities V_{mod}, which are then compared to the measured visibilities V_{mod} minimizing

CO line

XID	Flux (kJy · m/s)	East offset (arcsec)	North offset (arcsec)	Major axis (arcsec)	Minor axis (arcsec)	Position angle (deg)
(1)	(2)	(3)	(4)	(5)	(6)	(7)
34	1.17 ± 0.25	0.19 ± 0.03	0.12 ± 0.02	0.32 ± 0.11	0.20 ± 0.13	-51 ± 26
403	0.20 ± 0.09	< 0.01	-0.17 ± 0.3	0.42 ± 0.23	0.22 ± 0.07	58 ± 37
490	1.35 ± 0.12	0.09 ± 0.02	-0.26 ± 0.01	0.37 ± 0.07	0.26 ± 0.03	-37 ± 19

Dust continuum

XID	Flux density (mJy)	East offset (arcsec)	North offset (arcsec)	Major axis (arcsec)	Minor axis (arcsec)	Position angle (deg)
(1)	(2)	(3)	(4)	(5)	(6)	(7)
34	0.25 ± 0.05	0.24 ± 0.01	0.09 ± 0.02	0.38 ± 0.16	0.23 ± 0.13	-73 ± 37
403	0.43 ± 0.06	0.09 ± 0.02	-0.17 ± 0.03	0.29 ± 0.07	0.21 ± 0.08	-72 ± 32
490[1]	0.21 ± 0.05	0.05 ± 0.01	-0.21 ± 0.02	0.32 ± 0.05	0.26 ± 0.03	-63 ± 22

Table 3.7: Image fitting results for line (top panel) and continuum (bottom panel) emission. Columns from left to right: (1) Source ID. (2) Integrated flux for the line (because the fit has been performed on the moment 0 image) and flux density for the continuum. (3, 4) East and north offset of the center of the fitted Gaussian function with respect to the center of the field. (5,6) FWHM of the fitted Gaussian major and minor axes. (7) Position angle defined as the angle between the major axis of the fit and the north–south axis of the field. It spans from 0° to ±180° and it is positive if clockwise and negative if counterclockwise.
[1]XID 490 could not be spatially resolved during fitting, so we reported values of its size convoluted with the clean beam.

the χ^2 function:

$$\chi^2 = \sum_{k=1}^{m} \left| \frac{V_{obs}^k - V_{mod}^k}{\sigma_k} \right|^2$$

where k runs over baselines, times and frequency channels; σ_k is the uncertainty of $k-$th visibility.

The task that performs such a fitting is *uvmodelfit*, whose input/output parameters are: the flux density, east offset, north offset, major axis, axial ratio (defined as the ratio between the minor and major axes, thus it is always < 1) and position angle. The keys of this task are the following:

- **vis**: name of input visibility file.
- **comptype**: the model to fit to the visibilities. Point source, elliptical Gaussian and disk are available. We chose the Gaussian model for our sources since we are interested in their sizes in the sky plane.
- **niter**: number of iterations to perform during fitting. The recommended value is 5.
- **spw**: the spws to fit, in which a range of channels can be specified. We fit the line in the channels corresponding to the image channels

$v_0 \pm$ FWHM as derived from the spectral fitting and reported in Table 3.4. We will fit the continuum in the remaining channels of the line spw plus the other spws.

- **sourcepar**: the initial values from which the fit starts. The fit is very sensible to these values that should be properly evaluated. This is the reason why we first perform image fitting in order to set them as starting parameters for the visibilities.

- **varypar**: this key determines which parameters are kept fixed during the fitting.

Since *uvmodelfit* takes the flux density as input, for the line fitting we need to derive it from the integrated flux resulting from the moment 0 fitting. In order to do that we divide the integrated flux reported in the top panel of Table 3.7 by the FWHM of the line reported in Table 3.4.

We also need to calculate the visibility channels contained in the line range defined as $v_0 \pm$ FWHM in the previous section, since this has been obtained fitting the image spectrum composed of binned channels (the velocity widths Δv are reported in Table 3.2). Thus we need to find out which native channels (240 for each spw) correspond to the image channels. The native channels numbering is not along frequency (and thus velocity), but always points towards the central frequency of the band. Thus the channels of spws 2 and 3 increase with frequency, whereas the channels of spws 0 and 1 decrease. The channels of the images, instead, always decrease with frequency. We need to account for this discrepancy for those lines detected in spws 0 and 1, such as the case of XID 34 and XID 403. The image channels containing the $v_0 \pm$ FWHM range and reported in the last column of Table 3.4 can be easily converted in two visibility channels $c_1^{vis'}$ and $c_2^{vis'}$ by a simple proportion taking into account their total number. For XID 490, whose line is contained in spw 3 (thus the native channels increase with the image channels) these two correspond to the native channels containing the line, named c_1^{vis} and c_2^{vis}. For XID 34 and XID 403 the lines belong respectively to spw 1 and spw 0, so the native channels decrease as the image channels increase. In this case to properly compute c_1^{vis} and c_2^{vis} we need to subtract $c_1^{vis'}$ and $c_2^{vis'}$ from the very last native channel, the 239^{th}: $c_1^{vis} = 239 - c_2^{vis'}$, $c_2^{vis} = 239 - c_1^{vis'}$.

We report the channel ranges in Table 3.8. For XID 490 we consider the total channel range spanning from the first channel of the blue component to the last channel of the red component.

Finally, we perform the visibility fitting both for line and continuum emissions. We initially perform a fit letting all the parameters free in order to check whether the central position of the Gaussian matches that derived from the image fitting. Since they are within 1σ from the offset, we rerun a second fit keeping fixed the position (i.e. the east and north offset) in order

XID	Spw	Image Channels	Native Channels
34	1	36–56	99–149
403	0	0–6	195–232
490	3	68–94	148–205

Table 3.8: Spws, image channels range and native channels range containing the lines. Native channel width is 7.812 MHz; the image channel widths (in velocity) are 40 km/s, 120 km/s and 40 km/s for XID 34, XID 403 and XID 490, respectively.

to reduce the uncertainties related to the flux densities and the sizes. Final fitting results are reported in Table 3.9.

CO line

XID	Flux density (mJy)	East offset (arcsec)	North offset (arcsec)	Major axis (arcsec)	Axial ratio	Position angle (deg)
34	1.5 ± 0.1	0.21 ± 0.02	0.12 ± 0.02	0.38 ± 0.04	0.6 ± 0.2	-35 ± 13
403	0.7 ± 0.1	< 0.02	-0.20 ± 0.05	0.46 ± 0.13	0.6 ± 0.3	-46 ± 30
490	1.01 ± 0.07	0.12 ± 0.01	-0.24 ± 0.01	0.26 ± 0.04	0.5 ± 0.2	-42 ± 16

Dust Continuum

XID	Flux density (mJy)	East offset (arcsec)	North offset (arcsec)	Major axis (arcsec)	axial ratio	Position angle (deg)
34	0.23 ± 0.02	0.25 ± 0.03	0.08 ± 0.02	0.34 ± 0.07	0.6 ± 0.3	-75 ± 23
403	0.41 ± 0.02	0.09 ± 0.01	-0.17 ± 0.01	0.27 ± 0.03	0.6 ± 0.2	70 ± 13
490	0.19 ± 0.02	0.05 ± 0.01	-0.20 ± 0.01	0.17 ± 0.05	–	78 ± 21

Table 3.9: Final visibilities fitting results for each detected source relative to CO line transition (top) and continuum (bottom). Note that for XID 490 axial ratio could not be estimated for the continuum.

For what concerns the dust, the continuum axial ratio of XID 490 is consistent with 0. This is attributed to the very small size of the component that cannot be resolved in the minor axis direction. However, at least the major axis has been resolved, which represents an improvement with respect to image fitting showing one of the advantages mentioned at the beginning of this chapter in fitting directly the visibilities, i.e. obtaining sizes even in those sources that are not or barely resolved in the images.

Chapter 4

Results and discussion

In this chapter we use the angular sizes and fluxes obtained from our fits and measurements to calculate the physical sizes and masses of both the dust and molecular gas components. We exploit these quantities to derive the column density towards the nucleus assuming different geometries for the gas distribution: for all the sources we will examine the spherical case which is the simplest and most conservative assumption. In addition, for XID 403 and XID 490 (that show signatures of a rotating structure), we consider a more realistic rotating disk model, from which we extract the column density and inclination angle with respect to the line of sight assuming that the scale–heights of the dust and gas components are the same. We recall the adopted ΛCDM cosmology: $H_0 = 69.6$, $\Omega_M = 0.286$, $\Omega_\Lambda = 0.714$ (Wright, 2006).

4.1 Physical dimensions of the sources

Given the source redshift and the assumed cosmology we report in Table 4.1 the corresponding angular scale and luminosity distance for all sources in the sample.

XID	z	kpc/"	luminosity distance (Mpc)
262	3.666	7.349	32981.4
412	3.700	7.319	33347.1
34	2.937	7.904	25268.3
403	4.755	6.574	44909.9
546	3.064	7.806	26592.9
490	2.578	8.170	21575.1

Table 4.1: X-ray ID (Xue et al., 2011), angular scale (in kpc per arcsec) and luminosity distance for each source at the given redshift.

For what concerns the three detected sources, we have obtained the angular size of the major axis and the axial ratio from the visibility fitting

(i.e., the FWHM of the major axis and the axial ratio of the 2–D Gaussian fitted to the sources). Thus, we need to derive their minor axis with the proper error propagation. Despite the estimates of the major axis a and the axial ratio $R = b/a$ (being b the minor axis) are probably correlated during visibility fitting, for simplicity in the following we will assume that they are uncorrelated during the error propagation. Since the errors are largely dominated by the uncertainties on R, this assumption will not significantly affect the final results.

We recall that for a function $f(x_1, ..., x_n)$, linear in the $x_1, ..., x_n$ variables, the uncorrelated error propagation is:

$$\sigma_f = \sqrt{\sum_{i=1}^{N} \left(\frac{\partial f(x_1, ..., x_n)}{\partial x_i} \right)^2 \sigma_i^2} \tag{4.1}$$

where x_i and σ_i are the i–th variable and its associated error.

For XID 490, R of continuum could not be estimated either from the visibilities or from the image fitting (Table 3.9). However, from the images we have obtained the major and minor axes size convoluted with the clean beam. Although this convolution may significantly affect the value of a and b, it does not affect their ratio because the beam is nearly circular, thus the convolution just increases by the same factor the size in both directions. Hence, for XID 490, we assume the value of R derived from the convolved a and b, i.e. $R = 0.8$. As uncertainty we cannot assume the one propagated from these axes obtained by the image fitting, because the error of R derived from the visibility fitting is generally larger, as visible from the fits of the other sources in Table 3.9. These (relative) errors span the range 30%–50%. Thus, using a conservative approach, we assign a relative errorof 50% to R of XID 490, corresponding to the maximum error obtained from the other fits.

For the undetected sources (XID 262, XID 412 and XID 546) we assume a typical physical size. Several analyses have shown that this kind of objects have all comparable sizes (e.g. Swinbank et al., 2010; Tacconi et al., 2008). In addition, the mean redshift $z = 3.42$ of the detected sources is similar to that of the undetected ones ($z = 3.47$), thus we may expect that they have a similar size. Hence, we assume as the typical dimension of the undetected objects the mean of the detected ones. We still use a conservative approach assigning a 30% relative error to a and 50% to b, corresponding to the maximum uncertainties obtained from the visibility fits. In Table 4.2 the physical sizes of each source are reported for both the molecular gas and dust components.

Molecular gas		
XID	Major axis (kpc)	Minor axis (kpc)
34	3.0 ± 0.3	1.8 ± 0.6
403	3.0 ± 0.9	2 ± 1
490	2.1 ± 0.3	1.1 ± 0.5
262, 412, 546	2.7 ± 0.8	1.6 ± 0.8

Dust		
XID	Major axis (kpc)	Minor axis (kpc)
34	2.7 ± 0.5	1.6 ± 0.9
403	1.8 ± 0.2	1.1 ± 0.4
490	1.4 ± 0.4	1.0 ± 0.7
262, 412, 546	2.0 ± 0.6	1.2 ± 0.6

Table 4.2: Physical dimension (i.e. the physical size corresponding to the FWHM) of the ellipsoidal Gaussian fit for molecular gas (top) and dust (bottom) component. Since XID 490 dust axial ratio could not be estimated, minor axis has been calculated from the convoluted major and minor axial ratio of the image fit. For undetected sources (XID 262, XID 412 and XID 546) we assume the average size of the three detected objects. The uncertainties on the minor axis of XID 490 dust component and of both dust and molecular gas components of the undetected sources correspond to 50%, while the uncertainty related to the major axis of the undetected sources is 30%. Following a conservative approach, these errors have been set equal to the maximum relative errors of the visibility fits of the detected sources.

4.2 CO luminosity and mass

We estimate the CO luminosity from the integrated flux of the line (Table 3.9). We express the line luminosity as the areal integrated source brightness temperature L'_{line} in units of K km s^{-1} pc^2 (Carilli and Walter, 2013), since it is commonly used in the CO luminosity to the molecular gas mass conversion; it can be calculated by means of the well known relation from Solomon et al. (1992):

$$L'_{CO} = 3.25 \cdot 10^7 \left(\frac{\nu_{obs}}{\mathrm{GHz}}\right)^{-2} (1+z)^{-3} \left(\frac{D_L}{\mathrm{Mpc}}\right)^2 \left(\frac{F_{CO}}{\mathrm{Jy\ km\ s^{-1}}}\right) \mathrm{K\ km\ s^{-1}\ pc^2}$$

where ν_{obs} is the observed frequency, D_L is the luminosity distance and F_{CO} is the integrated flux of the line. We only considered the error on the flux since it is significantly larger than the uncertainty on the other quantities. It can be useful to have also luminosities L_{CO} expressed in c.g.s. units; we can convert L'_{CO} by the relation:

$$L_{CO} = 1.15 \cdot 10^{23} \left(\frac{\nu_{rest}}{\text{GHz}}\right)^3 \left(\frac{L'_{CO}}{\text{K km s}^{-1}\ \text{pc}^2}\right) \text{ erg/s}$$

where ν_{rest} is the rest frequency of the considered line.

As shown in Table 3.9, the fits return the fluxes in unit of Jy, so we need to multiply it by the width of the line in order to calculate the integrated fluxes in Jy km s^{-1}, required to estimate L'_{CO}. As line width we assume the FWHM with its uncertainty estimated through the Gaussian line fitting performed in Section 3.4 and reported in Table 3.4. For XID 490 we found a double–peaked line, which is a common feature of a rotating gas disk; in this case we calculate the total integrated flux by multiplying the flux density by the sum of the two line widths derived from the two Gaussian components of the fit. Indicating the blue–shifted line FWHM with LW_B (that is 474 ± 67 km/s) and red–shifted line FWHM with LW_R (that is 162 ± 27 km/s), the total FWHM for XID 490 will be $LW_{tot} = LW_B + LW_R = 636$ km/s with propagated uncertainty $\sigma_{LW_{tot}} = \sqrt{\sigma^2_{LW_B} + \sigma^2_{LW_R}} = 72$ km/s.

For the undetected sources we assume an upper limit to the flux density equal to 3 times the rms value measured from the peak channel reported in Table 3.3; as line width we consider a typical value of 400 km/s (e.g Carilli and Walter, 2013).

We call F_{CO} the integrated flux in Jy km s^{-1}, F the flux density in Jy, and Δv the line width in km/s. Thus, we can write:

$$F_{CO} = \left(\frac{F}{\text{Jy}}\right)\left(\frac{\Delta v}{\text{km/s}}\right) \text{ Jy km s}^{-1}$$

Table 4.3 reports the values found for the integrated line flues and the corresponding luminosities L'_{CO} and L_{CO}.

XID	CO	F_{int} (Jy km s^{-1})	L'_{CO} (10^9 K km s^{-1} pc^2)	L_{CO} (10^{40} erg/s)
262	6–5	< 0.32	< 5	< 19
412	6-5	< 0.31	< 5	< 19
34	5–4	0.55 ± 0.06	9 ± 1	19 ± 2
403	7–6	0.22 ± 0.06	4 ± 1	20 ± 6
546	5–4	< 0.33	< 6	< 13
490	4–3	0.64 ± 0.08	13 ± 2	14 ± 2

Table 4.3: Integrated flux F_{int} and both L'_{CO} and L_{CO} luminosities for each observed transition (reported in the second column) for the three detected sources.

We obtained L'_{CO} for the observed transitions. However, in order to estimate the masses we need the CO(1–0) luminosity, since the most common and studied conversion factor between CO luminosity and H_2 mass α_{CO} is related to the luminosity of this transition, as most of the molecular hydrogen

is traced by low–excited CO. Converting L'_{a-b} (luminosity of the transition between the two generic rotational energy levels a and b) in L'_{1-0} requires a CO Spectral Line Energy Distribution (SLED) in order to find out the ratio between the two transition luminosities. This ratio depends on the excitation level of the molecular gas, that can significantly differ for the various astronomical objects (e.g., Carilli and Walter, 2013). Historically, many sources have been classified as QSOs while others as SMGs, mainly due to the different selection techniques used; however, there is a significant overlap in their properties (Carilli and Walter, 2013). Without further precise information, we analyze separately the two classes of objects that will represent two limiting cases for our sources.

We will use L'_{a-b}/L'_{1-0} ratios reported in Table 2 of Carilli and Walter (2013), which are based on averaged values quoted on all the available literature. The ratio L'_{7-6}/L'_{1-0} for the (7–6) transition (needed for XID 403) and the ratio L'_{6-5}/L'_{1-0} for the (6–5) transition (needed for XID 262 and XID 412) are not reported, so we have extrapolated them from the CO–SLED presented in the same work, by means of the relation:

$$\frac{L'_{6-5}}{L'_{1-0}} = \frac{S_{1-0}}{S_{6-5}} \left(\frac{\nu_{r(6-5)}}{\nu_{r(1-0)}} \right)^2 \; ; \; \frac{L'_{7-6}}{L'_{1-0}} = \frac{S_{1-0}}{S_{7-6}} \left(\frac{\nu_{r(7-6)}}{\nu_{r(1-0)}} \right)^2$$

where S and ν_r are the averaged measured fluxes and the rest frequency of the two transitions. Table 4.4 summarizes the L'_{a-b}/L'_{1-0} assumed for each transition detected in our data.

XID	CO	L'_{a-b}/L'_{1-0} (SMG)	L'_{a-b}/L'_{1-0} (QSO)
490	4–3	0.46	0.87
34	5–4	0.39	0.69
546	5–4	0.39	0.69
262	6–5	0.40	0.71
412	6–5	0.40	0.71
403	7–6	0.21	0.51

Table 4.4: Ratio between (a–b) and (1–0) transition luminosity, where (a–b) is the transition reported in the second column. Two separate cases for SMGs and QSOs are reported. Note that the ratio is systematically lower for SMG: this may be attributed to the fact that the star formation in some SMG proceeds on more extended scales than in the QSO hosts (Weiß et al., 2007).

To estimate the total mass of the molecular gas, we need to assume a conversion factor α_{CO}, which also depends on the object type since it is likely a function of local ISM conditions. For the starburst nuclei of ULIRGs, Solomon et al. (1997) found an $\alpha_{CO} \sim 0.8$ $M_\odot$ (K km s^{-1} pc^2)$^{-1}$, which is a factor of ∼4 lower than what is found for the GMCs in the Milky Way (Bolatto et al., 2013). Such a low conversion factor would imply that there is more CO emission per unit molecular gas mass. Papadopoulos et al. (2012)

suggest that this is likely due to starburst activity that induces heating processes, resulting in an increase of the temperature and excitation level of the molecular gas with respect to normal galaxies. Since our sources are extremely compact and present a high SFR, we assume a conversion factor $\alpha_{CO} = 0.8\ \mathrm{M}_\odot\ (\mathrm{K\ km\ s^{-1}\ pc^2})^{-1}$ in order to estimate their molecular gas masses:

$$M_{H_2} = \left(\frac{\alpha_{CO}}{\mathrm{M}_\odot\ (\mathrm{K\ km\ s^{-1}\ pc^2})^{-1}}\right)\left(\frac{L'_{1-0}}{\mathrm{K\ km\ s^{-1}\ pc^2}}\right)\ \mathrm{M}_\odot$$

The values obtained for the CO(1–0) luminosities and molecular hydrogen masses are shown in Table 4.5.

XID	SMG SLED		QSO SLED	
	L'_{1-0}	Mass	L'_{1-0}	Mass
262	< 1.3	< 1.0	< 0.7	< 0.6
412	< 1.2	< 1.0	< 0.7	< 0.6
34	2.2 ± 0.2	1.8 ± 0.2	1.3 ± 0.1	1.0 ± 0.1
403	1.8 ± 0.5	1.4 ± 0.4	0.7 ± 0.2	0.6 ± 0.2
546	< 1.5	< 1.2	< 0.8	< 0.7
490	2.8 ± 0.4	2.2 ± 0.3	1.5 ± 0.2	1.2 ± 0.2

Table 4.5: CO(1-0) luminosities (expressed in 10^{10} K km s^{-1} pc^2) and H_2 masses (in units of $10^{10} M_\odot$) derived from two different CO SLEDs: SMG and QSO. The upper limits on the undetected sources have been obtained from a 3σ upper limit on the CO flux density and assuming a line width of 400 km/s.

The obtained masses reveal a large reservoir of gas confined in a few kiloparsec region, in agreement with the literature in the same redshift range (e.g. Carilli and Walter, 2013; Bothwell et al., 2013). Furthermore, Walter et al. (2004) show that sources with these masses and sizes could be observed up to a redshift $\gtrsim 6$. Gas masses derived assuming a QSO SLED are systematically lower than using a SMG SLED: QSO SLEDs indeed feature higher L'_{a-b}/L'_{1-0} ratios which then return lower L'_{1-0}.

4.3 Geometrical models and column density

We firstly present a spherical model for every source, which is the simplest assumption because it is symmetrical in any direction and independent on the inclination angle. However, this model likely underestimates the source density, since it distributes the mass on a larger volume than models based on more compact and realistic geometries (e.g., disk–like). Since we cannot infer anything about the geometry of the undetected sources, this simple spherical model is the only one that we present for them. Although XID 34 shows a gradient in the velocity field that could be associated to a rotating

structure, this source also presents an irregular gas distribution and a significant velocity dispersion over a region that comprises almost all the source emission (see moments in Figure 3.6), coupled with an anomalous shift of the CO(5–4) line with respect to the rest–frame frequency (Figure 3.4). The peculiar properties (that we will discuss in Section 4.5) of XID 34 do not allow us to unambiguously assess anything about its geometry, thus even for this source the spherical model will be the only one considered.

For XID 403 and XID 490 we can adopt a more realistic and compact geometry, that is a rotating disk with a constant scale height along the radius. Indications of a rotating system for XID 490 come from the observed velocity gradient, that is clearly distributed along a defined direction, and from the observed velocity dispersion, that is concentrated in the innermost region of the source (moments 1 and 2, Figure 3.6). Furthermore, the line shape shows a double–peaked feature ascribed to the Doppler effect, as shown in Figure 3.4. In addition, we have extracted the moment 0 (i.e., total flux of the line) separately for both the red and blue–shifted components of the line, at three different level of resolutions (from the lowest to the highest, the Briggs weighting parameter has been set equal to 1, 0.5, 0). The images are reported in Figure 4.1. The higher the resolution the more the two regions appear spatially separated: in the highest resolution images the separation is at least equal to the beam width in the same direction, showing that the blue and red–shifted peaks actually correspond to two different emitting regions moving in opposite directions with respect to the observer.

For XID 403 it would be more critical to securely assess the presence of a rotating system, because it does not feature a double–peaked line in the spectrum (Figure 3.4) and the low SNR per channel (< 5 in the peak). However, the velocity maps suggest the presence of a differential kinematic structure in one direction, at least with a beam separation between the red and blue–shifted region, and the velocity dispersion is confined in a relatively small region concentrated at the center of the source (moments 1 and 2, Figure 3.6). In addition, De Breuck et al. (2014), using ALMA data with a resolution of $\sim$0.5", demonstrated that the [C_{II}] emission is well described by a rotating disk model, whose position angle is consistent with that of this work (Figure 4.2).

4.3.1 The case of a sphere

We firstly consider a simple sphere as geometric model (Figure 4.3), from which we extract the gas density and column density. We fit this model for every detected and undetected source. For the former class we derive a value of the column density, whereas for the latter we derive an upper limit. As diameter of the source (named d in the following) we considered the mean value between the major and minor axes of the Gaussian ellipse fit, reported in the top panel of Table 4.2. The associated error is the error of the mean,

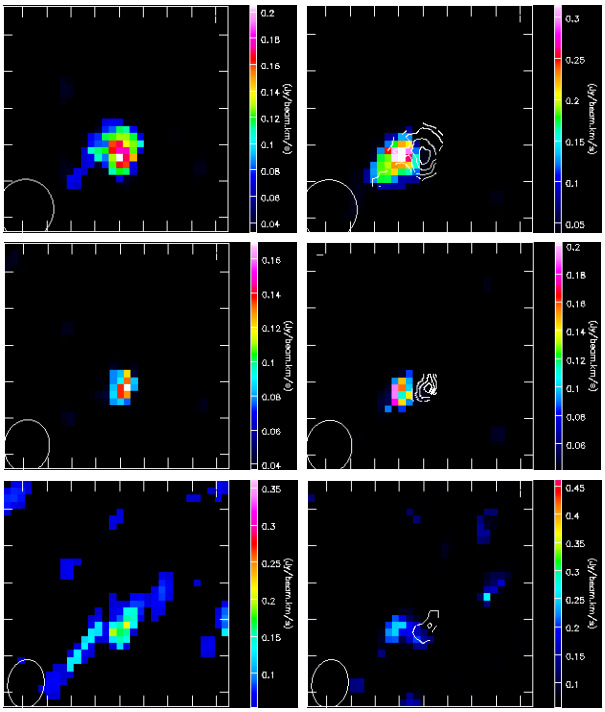

Figure 4.1: Moment 0 (integrated flux over the line) for the red (images on the left column) and blue (images on the right column) shifted component of the CO line of XID 490. On the blue–shifted images the contours related to the red–shifted component are reported in white. From top to bottom, the moments are reported using three different resolution: Briggs weighting equal to 1 (corresponding to the lowest resolution), 0.5, 0 (the highest resolution). The moments obtained using the Briggs weighting equal to 1 and 0.5 have been extracted from the datacube with 40 km/s of spectral resolution and are above the 3σ level with respect to the noise. Since the increase of the resolution degrades the sensitivity, for the moments with the Briggs weighting equal to 0 we rebinned the datacube to 80 km/s per channel in order to increase the SNR, and the threshold of the images has been lowered to 2σ above the rms. The white ellipse is the beam, whose size decreases as the resolution increases. The size of each image is ∼2.7" on a side.

that is $\sigma/\sqrt{2}$, where σ is the standard deviation.

We firstly calculate the volume V of the sources as:

$$V = \frac{\pi}{6}\left(\frac{d}{\mathrm{kpc}}\right)^3 \mathrm{kpc}^3$$

from which we can derive the gas density by using the mass reported in Table 4.5. In order to obtain the number density of the atomic hydrogen, we further divide by the H mass, approximated to the mass of proton $m_p = 1.67 \cdot 10^{-24}$ g:

$$n = \frac{1}{m_p}\left(\frac{M_{H_2}}{\mathrm{g}}\right)\left(\frac{V}{\mathrm{cm}^3}\right)^{-1} \mathrm{g\ cm}^{-3}$$

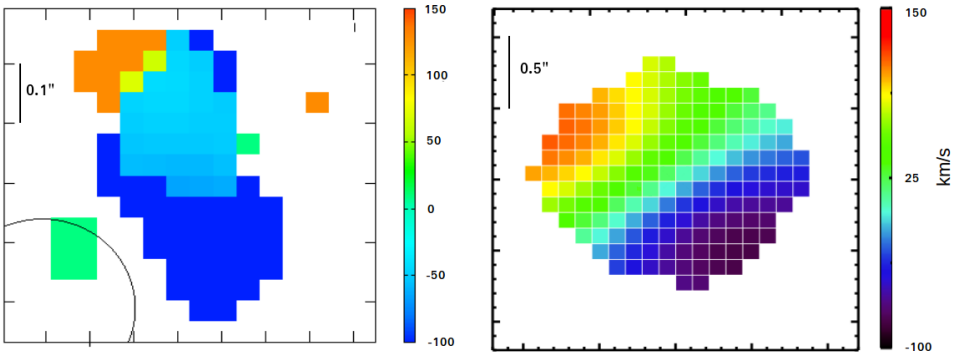

Figure 4.2: Velocity map of the CO(7–6) line from the datacube extracted in Section 3.1 (left) and velocity map of the rotating disk model fitting the [CII] emission performed by De Breuck et al. (2014) (right) of XID 403. The spectral resolution of the former datacube is 120 km/s, while that of the latter is 28.23 km/s. The angular scale is reported on the image. The black ellipse on the first image is the beam.

Since the volume is not linear in d and the density is not linear in V, Equation 4.1 cannot be used to estimate the uncertainties on these quantities; this formula, if $f(x_i)$ is not linear in the variable x_i, requires that the associated σ_i is small. Instead, the calculated diameters have a large error (that derives from the large error on the major and minor axes resulting from the fit), as well as the masses. Hence, to compute the proper uncertainties on the volume and density we use a numerical method reported in Lyons (1991). Given a general function $f(x_1, ..., x_i, ...x_n)$ of n variables x_i with associated error σ_i, we firstly compute the value f_0 in which each variable is set equal to the measured value. Then, we calculate the $2n$ functions defined as:

$$f_{i_+} = f(x_1, ..., x_i + \sigma_i, ...x_n) \ , \ f_{i_-} = f(x_1, ..., x_i - \sigma_i, ...x_n)$$

Finally, the lower and upper errors on $f(x_1, ..., x_i, ...x_n)$ (respectively indicated as σ_{f_-} and σ_{f_+}) are computed as:

$$\sigma_{f_\pm} = \sqrt{\sum_{i=1}^{n} (f_{i_\pm} - f_0)^2}$$

to estimate the 3σ upper limit on the number density (hence on column density) of the undetected sources we consider the 3σ upper limit of the masses reported in Table 4.5 and 3σ lower limit of the volume $V - 3\sigma_{V_-}$ where σ_{V_-} is computed with the aforementioned numerical method.

We are interested in estimating the column density N_H associated to the obscuration. As light path we assume the length starting from the center of the source, which in this model corresponds to the radius $d/2$ of the sphere:

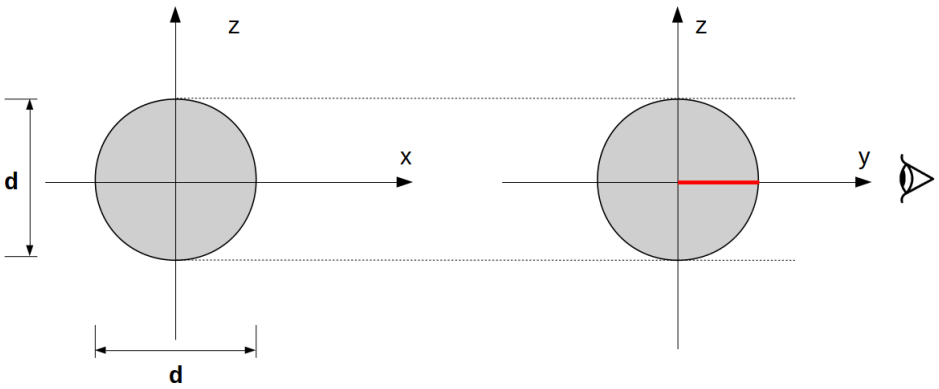

Figure 4.3: Sphere model as seen from two different positions: the plane that is perpendicular to the line of sight (i.e, the sky plane, left image) and side view (right image), where the eye symbol indicates the observer. The diameter of the source is indicated with d and corresponds to the average of the measured major and minor axis of the Gaussian ellipsoidal fit. The highlighted red line is the path considered to calculate the column density (that in this model coincides with the radius of the sphere), starting from the center of the source toward the outskirts. The two points of view are reported in order to compare this model with the following rotating disk in Figure 4.4.

$$N_H = \frac{1}{2}\left(\frac{n}{\mathrm{cm}^{-3}}\right)\left(\frac{d}{\mathrm{cm}}\right)\mathrm{cm}^{-2}$$

Number density and column density for each source and for both QSO and SMG cases are reported in Table 4.6. Due to large errors, for XID 403 we could estimate only an upper limit for the column density.

XID	SMG SLED		QSO SLED	
	n	N_H	n	N_H
262	< 148.5	< 4.0	< 83.7	< 2.2
412	< 145.5	< 3.9	< 82.0	< 2.2
34	$97.5^{+27.6}_{-40.5}$	$3.6^{+1.1}_{-1.5}$	$55.1^{+15.6}_{-22.9}$	$2.1^{+0.6}_{-0.9}$
403	$77.9^{+34.6}_{-76.0}$	$2.9^{+1.5}_{-2.8}$	$32.1^{+16.3}_{-31.1}$	$1.2^{+0.7}_{-1.1}$
546	< 170.2	< 4.6	< 96.2	< 2.6
490	$408.0^{+134.7}_{-213.3}$	$10.2^{+3.6}_{-5.5}$	$215.7^{+71.2}_{-112.7}$	$5.3^{+1.9}_{-2.9}$

Table 4.6: Number density (in units of cm^{-3}) and column density (in units of 10^{23} cm^{-2}) for the spherical model in both considered cases of SMG and QSO. The column density is estimated for a path length equal to radius of the sphere, i.e. starting from the center of the galaxy. Upper limits are given at the 3σ significance level.

The column density is from 3 to 15 times lower than that estimated from the X–ray spectral fitting performed by Circosta et al. (in prep.), except for XID 34 and XID 546. This discrepancy could be an indication that a significant part of the obscuration has to be ascribed to the torus surround-

ing the central engine. However, the spherical geometry assumption likely underestimates the density of the sources, and for a more compact geometry the two results may become more consistent with each other.

4.3.2 The case of a rotating disk

We now discuss a rotating disk geometrical model for sources XID 403 and XID 490. We consider the simple case in which the height and the radius of the disk are constant, i.e. we assume a cylindrical geometry where the sources have symmetric circular shape in the rotation plane (Figure 4.4). We aim at estimating the inclination angle and the height of the cylinder, and then derive the density and column density of the sources.

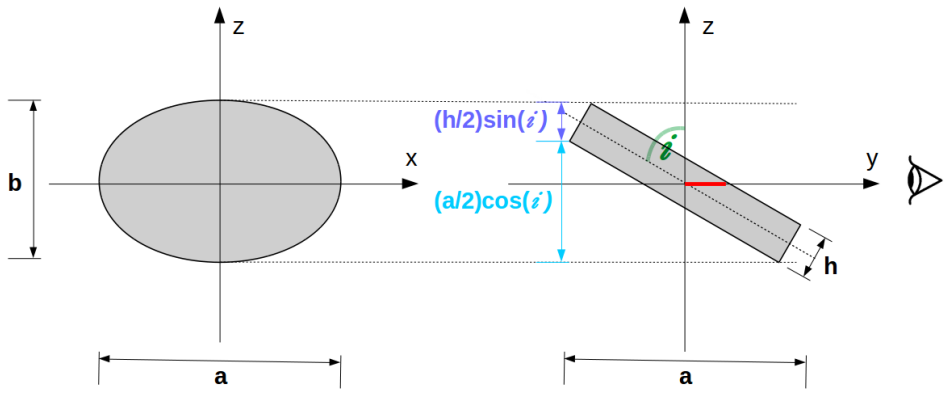

Figure 4.4: Rotating disk model as seen from two different positions: the plane that is perpendicular to line of sight (i.e, the sky plane, left image) and side view (right image), where the eye symbol indicates the observer. a and b are the major and minor axis of the Gaussian ellipsoidal fit, respectively. The inclination angle and the height of the disk are indicated as i and h, respectively. The highlighted red line is the path considered to calculate the column density, starting from the center of the source toward the outskirt and that is equal to $l = (a/2)\sin(i) + (h/2)\cos(i)$.

If we consider that the inclination angle is the same for the dust and gas components, the relations between the major and minor axes derived from the fit (Table 4.2), respectively a_D and b_D for the dust and a_G and b_G for the gas), the inclination angle i and the heights h_D (dust) and h_G gas are given by the system of equations:

$$\begin{cases} b_D = a_D \cos(i) + h_D \sin(i) \\ b_G = a_G \cos(i) + h_G \sin(i) \end{cases}$$

This system has two equations and three variable: h_D, h_G and i. Hence, we need a third condition in order to solve it. Since from Table 4.2 we note that the dust component is always confined in a region smaller than that of the gas ($a_D < a_G$ for all the sources), we can infer that likely $h_D < h_G$.

Thus, we can consider as limit case $h_D = h_G = h$, i.e. the gas and dust components have the same height. Under this assumption, the system has two sets of solutions:

$$i_{\pm} = \pm \cos^{-1}\left(\frac{b_G - b_D}{a_G - a_D}\right) \ , \ h_{\pm} = \frac{b_G - a_G \cos(i_{\pm})}{\sin(i_{\pm})}$$

For each source we consider the physically meaningful solution, i.e. the one with positive height and the corresponding inclination angle.

We can now derive the volume V of the cylinder:

$$V = \frac{\pi}{2}\left(\frac{a_G}{\mathrm{kpc}}\right)^2 \left(\frac{h}{\mathrm{kpc}}\right) \mathrm{kpc}^3$$

and the number density of the atomic hydrogen dividing the masses in Table 4.5 by the volume:

$$n = \frac{1}{m_p}\left(\frac{M_{H_2}}{\mathrm{g}}\right)\left(\frac{V}{\mathrm{cm}^3}\right)^{-1} \mathrm{g\ cm}^{-3}$$

As for the spherical model, to calculate the column density we consider a path length of the light starting from the center of the source, that in this case is $l = (a_G/2)\sin(i) + (h/2)\cos(i)$:

$$N_H = \left(\frac{n}{\mathrm{cm}^{-3}}\right)\left(\frac{l}{\mathrm{cm}}\right) \mathrm{cm}^{-2}$$

The results of the model are reported in Table 4.7. The values obtained for XID 490 are similar to those of the spherical model. The uncertainties on i, h, V n and l have been calculated using the numerical method reported in Lyons (1991), taking into account for both physical and geometrical constrains intrinsic to the model. In particular, we assumed that the dust component is confined in a region smaller than that of the gas, thus in summing and subtracting the uncertainties to the quantities during the error propagation we always have $a_D \leq a_G$ and $b_D \leq b_G$. In addition, since the minor axis should be always lower than the major axis, we constrained also $b_D \leq a_D$ and $b_G \leq a_G$. Due to the large uncertainties of both major axis and axial ratio of the Gaussian fit to the gas component (see Table 3.9), for XID 403 we report only an upper limit of the scale–height and column densities.

The derived scale–heights of the sources would imply a height-to-diameter ratio h/a of $0.38^{+0.5}_{-0.7}$ for XID 490 and <0.8 (at the 3σ level) for XID 403. The upper limit for XID 403 is consistent with a thin disk morphology. Given the large error, also the value derived for XID 490 is consistent within 1σ with a thin rotating structure. We stress that this large uncertainty, that strongly affects the determination of h, is related to the error on the inclination angle

			SMG SLED		QSO SLED	
XID	i (deg)	h (kpc)	n	N_H	n	N_H
403	-41^{+84}_{-60}	< 1.68	< 155.4	< 14.6	< 67.8	< 3.61
490	81^{+52}_{-53}	$0.8^{+0.6}_{-0.6}$	$323.1^{+265.4}_{-260.7}$	$10.9^{+10.7}_{-9.3}$	$176.2^{+145.7}_{-143.2}$	$5.9^{+5.7}_{-5.1}$

Table 4.7: Inclination angle i, heigh–scale h, number density n (in units of cm^{-3}) and column density N_H (in units of 10^{23} cm^{-2}) for the rotating disk model in both considered cases of SMG and QSO. The column density is estimated for a path length equal to $(a/2)\sin(i) + (h/2)\cos(i)$, i.e. starting from the center of the galaxy. For XID 403, the upper limit of h is given at the 1σ level and the upper limits of n and N_H are given at the 3σ level.

that can span for 105° within 1σ level of significance. More in general, the large errors on h and i make this model poorly constrained, thus it is likely that the gas is distributed in thinner systems. In addition, the model considers that the scale–heights of the gas and the dust are the same and constant over all the source radii, which may overestimate the volumes. In this case, the disk model would produce N_H values larger that the spherical model, and in turn closer to those estimated by the X–ray spectral fits.

4.3.3 Dynamical mass

We derive the dynamical masses M_{dyn} from the FWHM Δv of the CO lines obtained from the spectral fitting performed in Section 3.2 and reported in Table 3.4; for XID 490 we consider Δv equal to the mean of the blue and red–shifted component of the line, that is 323 ± 25 km/s. We derive the dynamical masses exploiting the following relation (Wang et al., 2013; Calura et al., 2014):

$$M_{dyn} \sin^2 i = 6.5 \cdot 10^4 \left(\frac{\Delta v}{\text{km s}^{-1}}\right)^2 \left(\frac{D}{\text{kpc}}\right) M_\odot$$

where i is the inclination angle with respect to the line of sight and D is the diameter of the disk, which corresponds to the measured major axis a_G in the considered disk model (see Figure 4.4). Given the large error on the inclination angle of both sources (Table 4.7), we report the quantity $M_{dyn} \sin^2 i$, leaving i as a unknown parameter. We found $M_{dyn} \sin^2 i = 1.8^{+1.7}_{-0.9} \times 10^{10}\ M_\odot$ for XID 403 and $M_{dyn} \sin^2 i = 1.4^{+0.3}_{-0.3} \times 10^{10}\ M_\odot$ for XID 490; assuming i equal to the values reported in Table 4.7, M_{dyn} are an order of magnitude lower than the values previously found for SMG at z∼2 based on the study of resolved and unresolved CO kinematics (Tacconi et al., 2008; Swinbank et al., 2010; Bothwell et al., 2013) and than the baryonic mass calculated as $M_{bar} = M_* + M_{H_2} + M_{HI}$, where M_* is the stellar mass obtained by the SED fitting (Table 1.1), M_{H_2} is the molecular gas mass derived from the CO emission in this work (Table 4.5) and M_{HI} is the atomic gas mass, assumed equal to $\sim M_{H_2}/5$ as found by Calura et al. (2014) on

the basis of IR observations of a large sample of high–redshift QSOs. The discrepancy between M_{dyn} and M_{bar} could be explained on the basis of our disk model only if a very low inclination angle ($|i| \lesssim 10°$) is assumed, but this would imply an unrealistic height–scale ($h \gtrsim 6$ kpc). Such discrepancy could be attributed to a overestimate of the stellar mass by the SED fitting or to a underestimate of Δv and D, given the sensitivity limitation of the observations. In addition, the used relation of Wang et al. (2013) assumes a ratio of 0.75 between the maximum projected circular velocity and the FWHM of the line, on the basis of C[II] observations. We stress that such discrepancy is also found for XID 403 by De Breuck et al. (2014) and Coppin et al. (2010), who have found a M_{dyn} in agreement with the value derived in this work. De Breuck et al. (2014) have assumed different inclination angles (29°, 50° and 53°), while in Coppin et al. (2010) an angle $i = 30°$ was assumed, as appropriate for randomly inclined disks in a sample of galaxies).

4.4 Dust mass and gas–to–dust conversion

We derive the mass of the dust in the optically thin regime, that is at rest–frame wavelength $\lambda > \lambda_0 = 220\ \mu m$, i.e. $\nu_0 = 1.5$ THz (Gilli et al., 2014).

The monochromatic luminosity L_ν expressed in erg s^{-1} Hz^{-1} at the rest–frame frequency ν can be written as

$$\begin{cases} L_\nu = \frac{4\pi D_L^2 S_{obs}}{1+z} \\ \\ L_\nu = 4\pi j_\nu V \end{cases}$$

where z is the redshift, D_L is the luminosity distance, S_{obs} is the flux density at the observed frequency ν_{obs}, V is the volume of the source and j_ν is the specific emissivity per unit volume (erg s^{-1} Hz^{-1} ster^{-1} cm^{-3}) that is equal to

$$j_\nu = \alpha_\nu B_\nu(T_d) = k_\nu \rho B_\nu(T_d)$$

where $B_\nu(T_d)$ is the Planck function of the dust emission at the temperature T_d, $\alpha_\nu = k_\nu \rho$ is the opacity per unit of path length (cm^{-1}), k_ν is the opacity per mass unit (g^{-1} cm^2) and $\rho = M_d/V$ is the density of the source (g cm^{-3}), with M_d indicating the total mass of the dust. The opacity per mass unit is assumed to scale with the frequency as $k_\nu = 4(\nu/1.2\ THz)^\beta$ (Draine and Li, 2007). The index β is set equal to 2.0 (e.g. Magnelli et al., 2012; Gilli et al., 2014).

Equalizing the two expressions of L_ν leads to the formula for the mass of the dust in the optically thin regime:

$$\frac{4\pi D_L^2 S_{obs}}{1+z} = 4\pi k_\nu \frac{M_d}{V} B_\nu(T_d) V$$

$$M_d = \frac{D_L^2 S_{obs}}{k_\nu B_\nu(T_d)(1+z)}$$

The measured flux density S_{obs} is set equal to that reported in the bottom panel of Table 3.9 for the detected sources and equal to 3 times the rms value measured on the peak channel reported in Table 3.3 for the undetected sources, in order to obtain an upper limt. The rest–frame frequency $\nu = \nu_{obs}(1+z)$ is computed considering as ν_{obs} the median observed frequency of the spws in which the imaging and fitting of the continuum have been performed. The temperatures T_d of the dust has been derived from the SED fitted with a single component modified black body $S_\nu \propto B_\nu(T_d)(1-e^{-\tau_\nu})$ by means of the code developed by Feltre et al. (2012), see also Circosta et al. (in prep.). The fiducial error associated with such temperatures is of the order of $\approx \pm 5$ K. The results are reported in Table 4.8.

XID	ν_{rest} (GHz)	T (K)	M_d (10^8 $M_\odot$)
262	138.7	71	< 1.0
412	138.7	80	< 0.9
34	142.7	55	4.9 ± 0.7
403	132.7	65	4.8 ± 0.5
546	132.1	65	< 1.5
490	136.3	69	4.2 ± 0.5

Table 4.8: Rest frequency (calculated as $\nu_{rest} = \nu_{obs}(1+z)$ where ν_{obs} is the median observed frequency for the continuum emission), dust temperature T (derived from the SED fitting, with a fiducial associated error of $\approx \pm 5$ K) and mass of the dust M_d for each source. The upper limits on the masses are given at 3σ level.

To estimate the gas mass from the continuum luminosity, we exploit the relation between the luminosity of the CO(1–0) transition L'_{1-0} and the luminosity at 850 μm ($\approx$ 353 GHz) $L_{850\mu m}$ found by Scoville et al. (2016), and valid for normal star formation galaxies, local ULIRGs and SMGs:

$$L'_{1-0} = 3.02 \times 10^{-21} \left(\frac{L_{850\mu m}}{\text{erg s}^{-1}\ \text{Hz}^{-1}} \right)\ \text{K km s}^{-1}\ \text{pc}^2$$

$L_{850\mu m}$ can be derived by the flux density at 850 μm $S_{850\mu m}$:

$$L_{850\mu m} = 4\pi D_L^2 S_{850\mu m}$$

Thus, we firstly need to rescale the measured flux densities S_{obs} (at $\lambda \approx$ 2.1 mm) to $S_{850\mu m}$. We assume a modified black body law in the optically thin regime $S_\nu \propto B_\nu(T_d)(1-e^{-\tau}) \approx B_\nu(T_d)\tau_\nu$ where $\tau_\nu = (\nu/\nu_0)^\beta$ is the dust optical depth, with $\beta = 2$ and $\nu_0 = 1.5$ THz, defined as the frequency at which the dust becomes optically thick (e.g. Conley et al., 2011; Rangwala et al., 2011; Gilli et al., 2014); at this wavelength the Planck function can be

approximated by the Rayleigh–Jeans law $B_{\nu,RJ} = 2K_B T\nu^2/c^2$, thus $S_\nu \propto \nu^4$. Hence, the ratio between $S_{850\mu m}$ and the observed S_{obs} can be expressed as:

$$\frac{S_{850\mu m}}{S_{obs}} = \left(\frac{353 \text{ GHz}}{\nu_{obs}}\right)^4$$

In order to calculate the masses we still assume $\alpha_{CO} = 0.8$ M$_\odot$ (K km s^{-1} pc^2)$^{-1}$. The results are reported in Table 4.9.

XID	$S_{850\mu m}$ (μJy)	L'_{1-0} (10^{10} K km s^{-1} pc^2)	M_{H_2} (10^{10} $M_\odot$)
262	< 7	< 2.7	< 2.1
412	< 7	< 2.7	< 2.1
34	35 ± 3	8.2 ± 0.7	6.6 ± 0.6
403	17 ± 1	13.5 ± 0.7	10.8 ± 0.5
546	<13	< 3.3	< 2.6
490	52 ± 5	8.7 ± 0.9	7.0 ± 0.7

Table 4.9: Flux density at 850 μm $S_{850\mu m}$, luminosity of the CO(1–0) transition L'_{1-0} and the corresponding H_2 mass M_{H_2} derived assuming $\alpha_{CO} = 0.8$ M$_\odot$ (K km s^{-1} pc^2)$^{-1}$. The upper limits on the masses are given at 3σ.

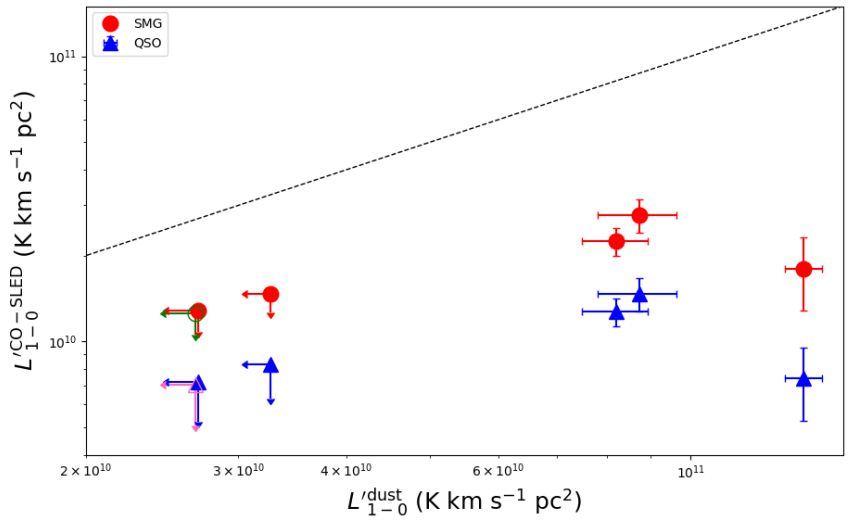

Figure 4.5: Luminosity $L'^{\rm dust}_{1-0}$ of the CO(1–0) transition derived from the dust emission vs. luminosity $L'^{\rm CO-SLED}_{1-0}$ of the CO(1–0) transition derived from the CO–SLEDs, for our sample. The CO–SLEDs are indicated as SMG (red filled circles) and QSO (blue filled triangles). For clarity, since the points of XID 412 and XID 262 are almost superimposed, for the latter we indicate the SMG CO–SLED with a green open circle and the QSO CO–SLED with an open pink triangle. The black dashed line represents the $L'^{\rm dust}_{1-0} = L'^{\rm CO-SLED}_{1-0}$ curve.

As shown in Figure 4.5, for the detected sources (XID 34, XID 403 and

XID 490), the L'_{1-0} luminosities (and thus the gas masses) obtained using the dust emission are systematically above those derived from the CO–SLEDs conversion factors (Carilli and Walter, 2013). The large scatter of the assumed CO–SLEDs would not produce such a systematic shift. Thus, this could be attributed to the fact that the relation between $L_{850\mu m}$ and L'_{1-0} found by Scoville et al. (2016) has been calibrated for SMGs at z∼2 and can vary at different redshifts. The large number of variables that affects the thermal dust emission may suggests that the relation found by Scoville et al. (2016) cannot be universally applied to this kind of objects. In addition, the formation and destruction mechanisms of the dust are currently debated and the physical condition and composition of the dust may vary significantly for the individual sources (see Calura et al., 2014). Finally, we note that the dust temperatures have been derived under the simplistic assumption of the presence of a single component, whereas the co–existence of dust a different temperatures would likely change the derived values of the flux densities (and the related L'_{1-0}).

4.5 Notes on individual sources

XID 34 is the source that features the most peculiar morphology among the sample (see the gas integrated emission and velocity map in Figure 3.6). The gradient along one direction in the velocity map suggests a differential kinematic structure, since there are two regions moving in opposite directions with respect to the line of sight, at least with a beam separation from each other. However, due to the lack of further information, this feature cannot be securely associated with a rotating disk morphology. In addition, the detected CO(4–3) line (Figure 3.5) does not feature any indication of Doppler effect, but results entirely shifted by $\sim$ 500 km/s from the rest–frame velocity corresponding to z=2.94. Since the spectroscopic redshift has been derived from the optical spectrum, we have investigated the observation of the source carried out by the Hubble Space Telescope (HST) in the V band, corresponding to the rest–frame UV emission. In Figure 4.6 we report the optical image on which the contours of continuum dust emission detected in this work have been superimposed.

The region in which the UV emission peaks is shifted by ∼0.2 arcsec from the center of the dust emission in the North direction. The possible position errors due to the astrometry are far lower than this angular distance, for both HST and ALMA images. This kind of displacement has been observed in several dusty gas–rich objects (Fu et al., 2012; Dye et al., 2015; Massardi et al., 2018) and is associated to the obscuration due to the dust: the UV emission traces the direct light of young stars that is not obscured, while the light coming from the dust–richer region is extinguished and thermally re–emitted. In this scenario, it is very likely that most of star formation

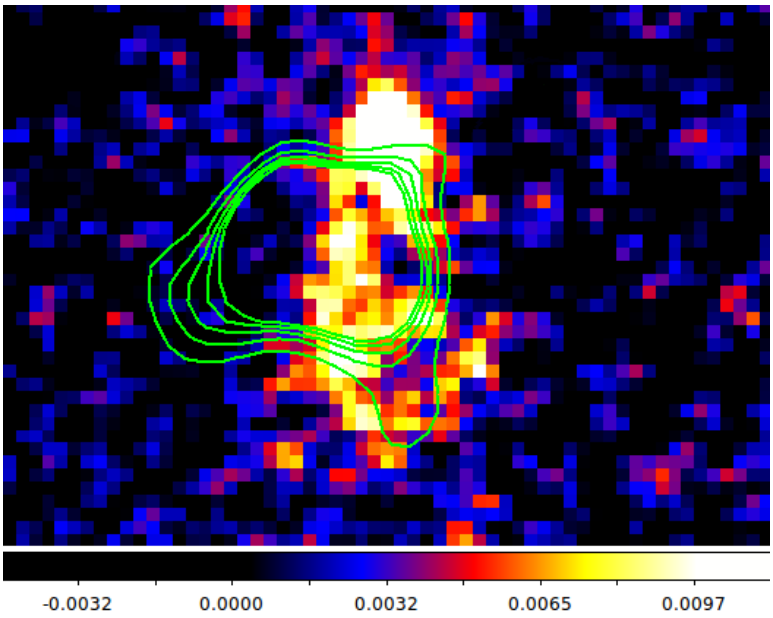

Figure 4.6: V–band ($\sim$ 600 nm) HST image of XID 34. The green contours represent the continuum emission of the dust, detected in this work. The color–scale is given in counts per second. The image size is $\sim 0.6 \times 0.9$ arcsec.

happens in the innermost dusty region but cannot be directly probed. We think that the X–ray emission associated to the AGN likely corresponds to the centroid of the ALMA dust continuum, rather than to the centroid of the region where the optical emission peaks. In addition, the displacement that we measured between the CO rest–frequency and the optical spectrum rest–frequency can be explained as an intrinsic different motion velocity between the two regions. These peculiar properties of XID 34 (irregular morphology and chaotic motion of the different components) suggest that this source may be associated with a merger structure. However, without further information, we cannot draw any definitive conclusion on its nature.

XID 403 has been studied in several works: Coppin et al. (2010) detected the CO(2–1) emission line from which they derived a gas mass $M_{gas} \simeq 1.6 \times 10^{10}\ M_{\odot}$; De Breuck et al. (2014) spatially resolved the C[II] emission from which they constrained the diameter of the continuum emission to a region < 2 kpc; Gilli et al. (2014) on the basis of the continuum emission at 1.3 mm, measured a dust mass of $M_d = 4.9 \pm 0.7 \times 10^8 M_{\odot}$ confined in a half–light radius of 0.9 ± 0.3 kpc. All these results are fully in agreement with the values derived in this work for the size (Table 4.2), gas mass (Table 4.5) and dust mass (Table 4.8).

XID 490 is one of the least studied sources in the sample. The values of L'_{1-0} obtained from the conversion of the luminosity of the observed CO(6–5) transition by means of both SMG and QSO CO–SLEDs conversion factors

are consistent with the upper limit 1.6×10^{10} K km s^{-1} pc^2 found by Perna et al. (2018) on the basis of CO(1–0) observations.

Two of three undetected sources (XID 262 and XID 412) have been observed for half of the time needed to achieve the PI requested sensitivity, and this may partially explain they were not detected. XID 546, instead, is included in the execution block that has been observed twice and for which the requested sensitivity has been reached. The original proposal of the observations of all the sample was made predicting the flux density in the ALMA band 4 ($\sim$2.1 mm) assuming a modified black–body model; this model was constrained on the basis of the available photometric data. Since the slope of this model in the Rayleigh–Jeans tail is a function of the β index for the optical depth ($S_\nu \propto \nu^{2+\beta}$), a slightly steeper index than assumed may explain why the source is not detected.

Chapter 5

Conclusions and future perspectives

Distant ($z \gtrsim 2$) SMGs trace most of the star formation and BH accretion activity during the lifetime of massive systems and represent a crucial phase in their evolution. They feature very high SFR ($\sim 10^{2-3}$ $M_{\odot}$/yr) and large reservoir of gas ($\sim 10^{10-11}$ $M_{\odot}$/yr) (e.g., Bothwell et al., 2013) and often host heavely obscured, even Compton–thick AGN (e.g, Wang et al., 2013). In addition, several supporting observational indications were found for an increasing fraction of obscured AGN from $z = 0$ to $z \approx 3$ (Vito et al., 2013, 2018). The gas consumption times attributed to both SF and BH accretion are estimated to be small, of the order of $\sim 10^{7-8}$ yr, after which the AGN direct emission is revealed. In this scenario, the brief SMG evolution phase is therefore crucial to understand the ISM contribution to the obscuration of the central engine, and its role in the host galaxy/AGN co–evolution. In addition, SMGs are among the best candidates as progenitor of CQGs, a class of quiescent galaxies that are considerably smaller and denser than local galaxy counterparts. About 1/3 of cQGs contain an AGN, whereas the non–compact star forming galaxies have a AGN fraction $< 1\%$, and this suggests that AGN feedback plays a relevant role in the evolution of these systems (Zubovas et al., 2013).

To the purpose of evaluate the host galaxy contribution to the AGN obscuration, we have selected a sample of six SMGs hosting a heavily obscured ($\log N_{H_X} > 23$) AGN in the redshift range $\sim 2.5 < z < 4.7$ in the CDF–S, for which the combination of ultra–deep Chandra observations (7 Ms) and ALMA data allowed us to address the obscuration issue from two different points of view: on the one hand the X–rays directly probe the innermost region of the sources and can be used to evaluate the intrinsic absorption to the central engine emission; on the other hand, the millimetric band is crucial to investigate the ISM properties such as mass and geometrical distribution of the gas and dust components in order to evaluate its contribution to the

obscuration.

In this work we have analyzed the millimetric emission of the CO line from different transitions and the dust continuum of these six sources, in order to derive their molecular gas and dust masses and their physical sizes; we have exploited these data to evaluate, under simple geometrical assumptions, the column densities relative of the ISM in our targets. The observations have been carried out during ALMA observing Cycle 4 in band 4 ($\sim$ 2 mm). A summary of the CO observed transitions, redshift and general properties of the sources are reported in Table 1.1.

We have reduced the raw dataset via the ALMA pipeline and performed a quality–check of the data inspecting the diagnostic plots and the visibility space.

We have performed imaging of both line and continuum; both of them were detected for three out of six sources, for which we have extracted the CO line integrated emission, velocity and velocity dispersion maps (Figure 3.6). Both the (integrated) line and continuum emissions were fitted in the brightness and visibility spaces with a 2–D Gaussian model in order to derive their flux densities and angular sizes reported in Table 3.9. In addition, we have analyzed their spectra and performed a Gaussian fit of the lines, whose properties are reported in Table 3.4. For one of these sources (XID 490) we found a clear signature of a rotating structure, given the double–peaked feature of the line. The line of XID 34 resulted shifted by $\sim$500 km/s with respect to the rest–frame velocity; this feature, coupled with the chaotic morphology and kinematics of the gas and to the comparison with the HST optical image (V–band, Figure 4.6) in which it is present a displacement between the bulk of the dust and the UV maximum emitting region of the stellar components, suggest that this source is possibly undergoing a merger.

We have converted the angular sizes of the sources in physical sizes (reported in Table 4.2), given their redshift. We have assumed for the undetected sources a size equal to the mean of that of the detected ones, assuming that these objects have all comparable size (e.g, Swinbank et al., 2010). The sources are found to be extremely compact objects, all having a major axis of the Gaussian fit $\lesssim$ 3 kpc. In addition, the dust component is contained in a region smaller ($\sim$70% on average) than that of the gas for all the sources.

We have derived the luminosities of the detected lines from the flux densities obtained from the Gaussian fit (Table 4.3); for the undetected sources we have assumed an upper limit derived from the SNR measured directly on the images. Then we have converted these luminosities in the luminosities of the CO(1–0) transition assuming two different CO SLEDs related to SMGs and QSOs, respectively (Carilli and Walter, 2013). Thus, we have derived the molecular gas mass assuming a conversion factor $\alpha_{CO} \sim$ 0.8 $M_\odot$ (K km s^{-1} $pc^2)^{-1}$ for both the considered CO(1–0) luminosities. All the sources are massive systems, having molecular gas masses of the order of $\sim 10^{10} M_\odot$ (Table 4.5). In addition, from the continuum emission we have

derived the flux density at 850 μm assuming a modified black–body model, then a second estimate of the mass of the molecular gas by means of the relation found by Scoville et al. (2016), calibrated for a gas–to–dust ratio of SMGs at z $\sim$ 2. In general we found that these masses (Table 4.9) are a factor of 1.5–10 larger than those estimated directly from the detected CO transitions. This discrepancy can probably be attributed to the large number of assumptions on the conversion factors used in both the methods. From the continuum emission we have also derived the mass of the dust, assuming a modified black–body law in the optically thin regime. We found that the mass of the dust is of the order of $\sim 10^8$ $M_\odot$ for all the sources (Table 4.8). Finally we also derived the inclination angle–dependent dynamical masses for XID 403 and XID 490, whose values are of the order of $10^{10} M_\odot$. These masses are one order of magnitude lower than the sum of stellar and gas mass. This discrepancy has been previously reported in other works for XID 403 assuming different inclination angles (Coppin et al., 2010; De Breuck et al., 2014); we note that due to the large uncertainty on the source geometry and size it is not possible to determine at which distance from the galaxy center the rotation velocity peaks. The relation used in this work to estimate the dynamical mass was found by Wang et al. (2013) assuming a ratio of 0.75 between the maximum projected circular velocity and the FWHM of the line, on the basis of C[II] observations, but this ratio can likely vary for the molecular gas and for different detected lines. In addition, such discrepancy could be attributed to a overestimate of the stellar mass by the SED fitting or to a underestimate of Δv and D because, given the sensitivity limitation of the observations, we could miss the low–brightness region in the outskirts of the sources.

We have assumed a simple spherical model for all the sources and derived densities and column densities for the detected sources and upper limits for the undetected ones (Table 4.6). Then, since for XID 403 and XID 490 we have enough indications of rotating structures, we have tested a more realistic model consisting in a rotating disk with constant scale–height. We have assumed a limit condition in which the scale–heights of the gas and dust components are equal and derived the inclination angle, the scale–height, density and column density of the two sources (Table 4.7). The column densities $N_{H_{ISM}}$ obtained from the adopted models vs. the column densities obtained by the X–ray spectra fitting N_{H_X} are shown in Figure 5.1.

For the spherical model, the values of $N_{H_{ISM}}$ are generally lower than N_{H_X} by a factor from $\sim$ 3 (for XID 490) to 5 (for XID 403) considering the SMG CO–SLED, and by a factor from $\sim$ 7 (for XID 490) to 15 (for XID 403) considering the QSO CO–SLED, except for XID 34 (for which both the values related to the SMG CO–SLED and QSO CO–SLED are in agreement with N_{H_X} at the 1σ level) and XID 546 (whose upper limit for to the SMG CO–SLED is consistent with N_{H_X}). The rotating disk model, tested for XID 490 and XID 403, features values of $N_{H_{ISM}}$ similar to those of the spheri-

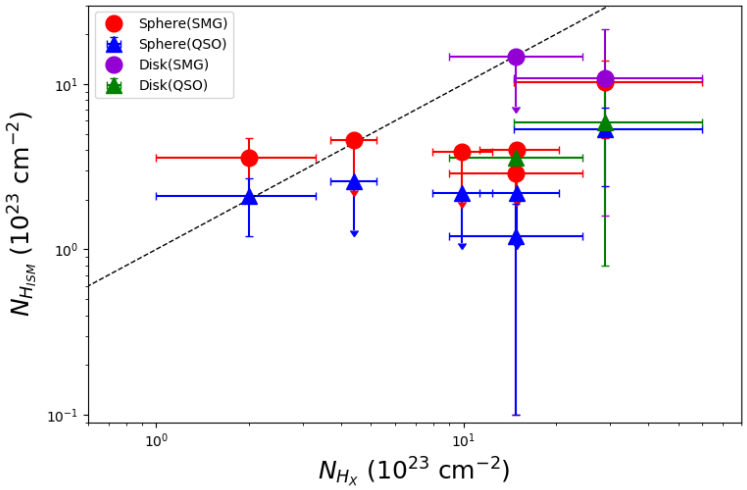

Figure 5.1: Column densities of all the sources for the considered geometries and CO–SLEDs conversion factors between the detected emission line luminosity and the CO(1–0) transition luminosity. In case of spherical geometry, the values related to the SMG CO–SLED and the QSO CO–SLED are indicated by the red circles and blue triangles, respectively. For XID 403 and XID 490 we have also tested a rotating disk geometry, whose column densities (upper limits for XID 403 and values for XID 490) are indicated by the purple circles and green triangles for the the SMG CO–SLED and the QSO CO–SLED, respectively. The black dashed line represent the $N_{H_X} = N_{H_{ISM}}$ curve. The error bars correspond to the 1σ significance level, while the upper limits are given at the 3σ level.

cal model for the former source and a 3σ upper limit compatible with N_{H_X} for the latter. However, the large uncertainties on the inclination angle and the scale–height make the disk model poorly constrained, and the obtained values of $N_{H_{ISM}}$ can significantly vary even due to a slight variation of the inclination angle. We stress that the uncertainties that strongly affect our results are due to the errors on quantities originally derived from the fits. In particular, the major axis and the axial ratio of the Gaussian fitting feature errors up to 30% and 50%, respectively. Thus, most of the uncertainty on the densities and column densities is strictly related to the uncertainty on the angular dimension of the sources, which reflects the limit of the resolution of the observations. In future, observations at better resolution (< 0.1 arcsec) and higher sensitivity of these sources (or other similar detected in other fields) would drastically reduce the uncertainties on the physical quantities derived in this work and would provide better constrains the assumed geometry models. However, despite the uncertainties, we conclude that the host galaxy can substantially contribute to the obscuration of the AGN.

Our results also show that a SMG CO–SLED is, on average, more successful than a QSO CO–SLED in explaining the obscuration in terms of the host galaxy contribution. We note that for XID 403 other two CO transition

lines at very different excitation levels have been previously detected: CO(2–1) by Coppin et al. (2010) and CO(12–11) by Nagao et al. (2012). Coupling this measurements with our CO(7–6) detection would allow us to build a rough CO–SLED to investigate the properties of the excited molecular gas of this source, and eventually evaluate if the general SMG CO–SLED derived by Carilli and Walter (2013) suits the gas physical conditions of the gas in obscured AGN up to z$\sim$4.7.

Finally, the vigorous SF and the large reservoir of gas confined in a relatively small region found for our sources are fully in agreement with the hypothesis that this class of objects is the best candidate progenitor of cQGs.

Appendix A

Total field of view images

In this Appendix we report approximately the total field of view images relative to the peak emission channel of CO line (Figure A.1) and the continuum emission (Figure A.2). Note that for XID 490 two images are reported for the CO emission, given the double–peaked feature of the line.

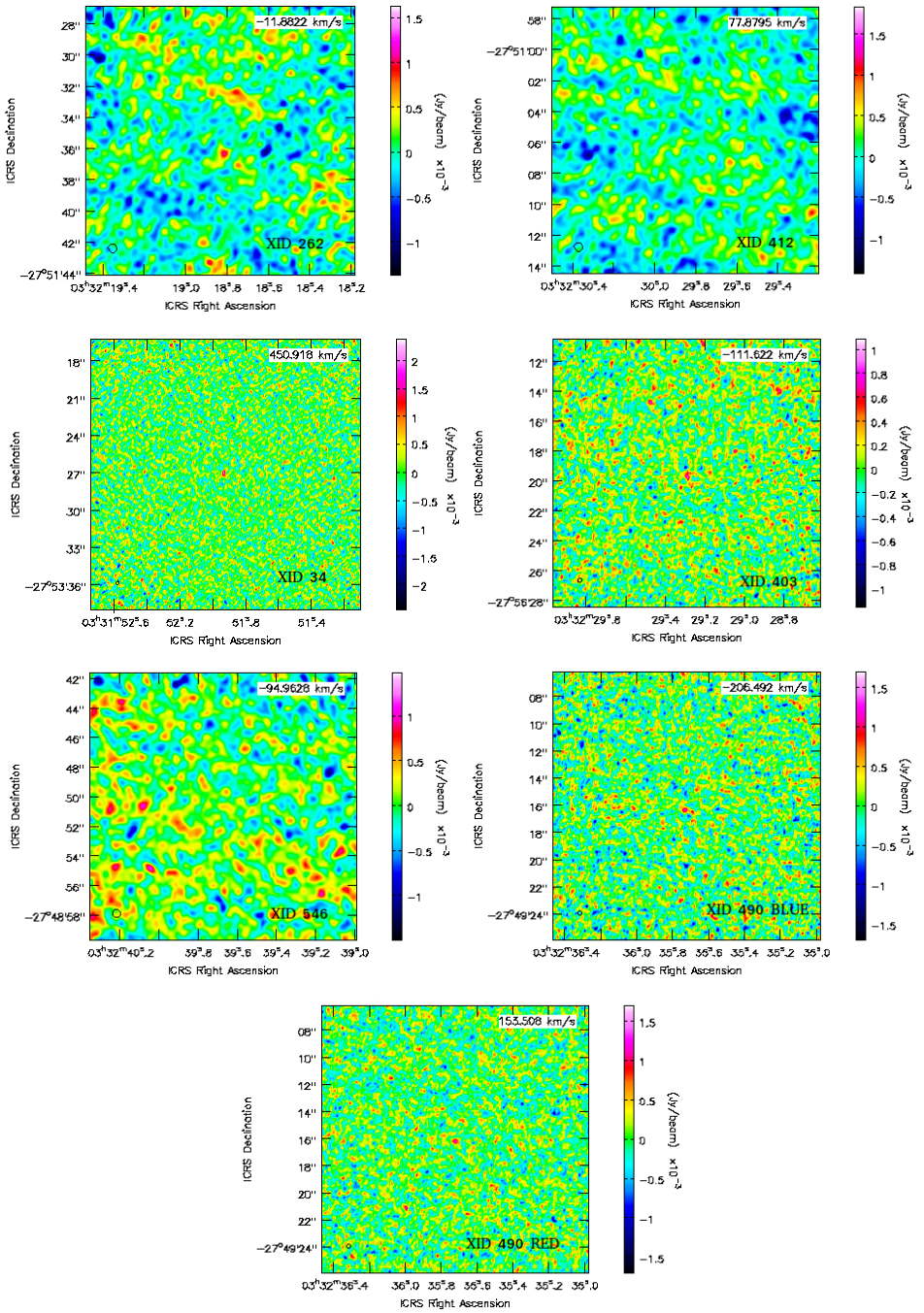

Figure A.1: Total field of view of the peak channel of the datacube for each source. Source ID and the velocity corresponding to the center of the channel are reported on the image. The black ellipse in the left bottom corner is the clean beam. Note that for XID 490 two images are shown: XID 490 BLUE and XID 490 RED respectively correspond to the blue–shifted and red–shifted peaks.

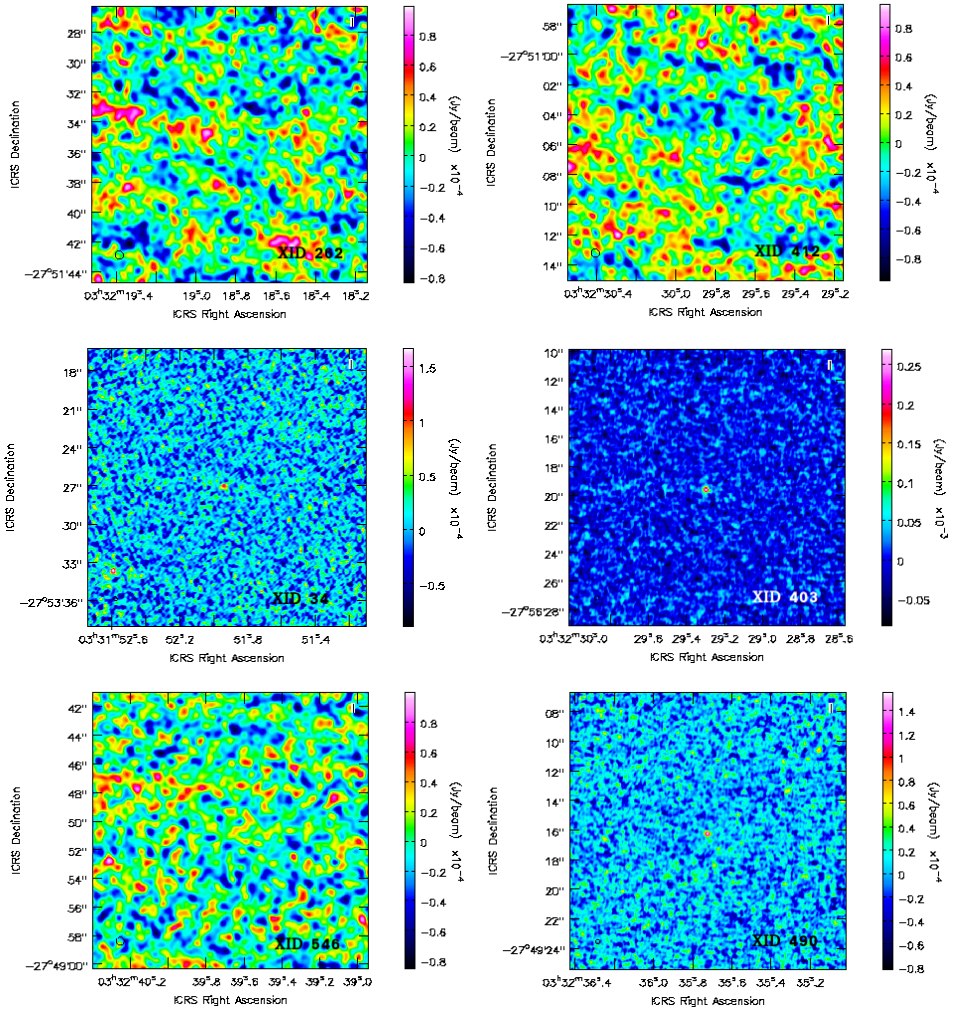

Figure A.2: Images of the Total field of view of the continuum emission. Source ID is reported on the images. The black ellipse in the left bottom corner is the clean beam.

Appendix B

Example of an X–ray spectrum and IR SED: XID 490 at z=2.578

In this Appendix we report as an example the X–ray spectrum and IR SED of the source XID 490, in Figure B.1 and Figure B.2, respectively. The fits of both are taken from Circosta et al. (in prep.) and their components are described in the captions of the figures.

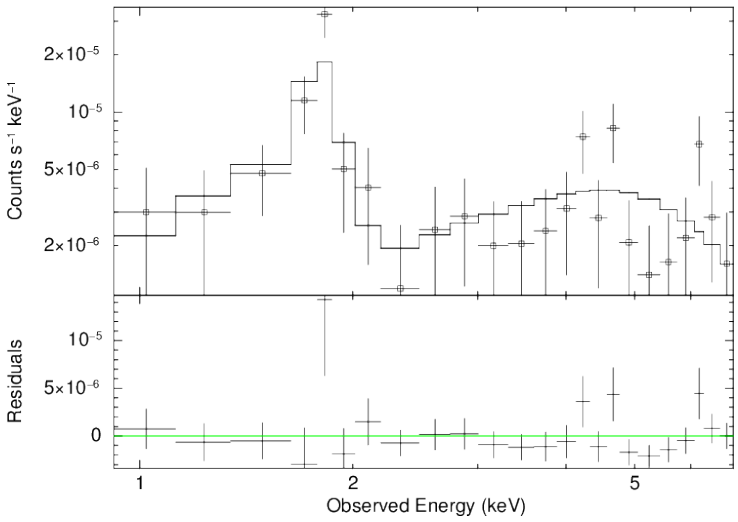

Figure B.1: X–ray spectrum of XID 490. The fitting (indicated by the black solid line) is relative to the MYtorus model (Murphy and Yaqoob, 2009), that self-consistently takes into account photoelectric absorption, Compton scattering, cold reflection and fluorescent emission in a fixed toroidal geometry. In the bottom panel the residuals of the fit are shown. From Circosta et al. (in prep.).

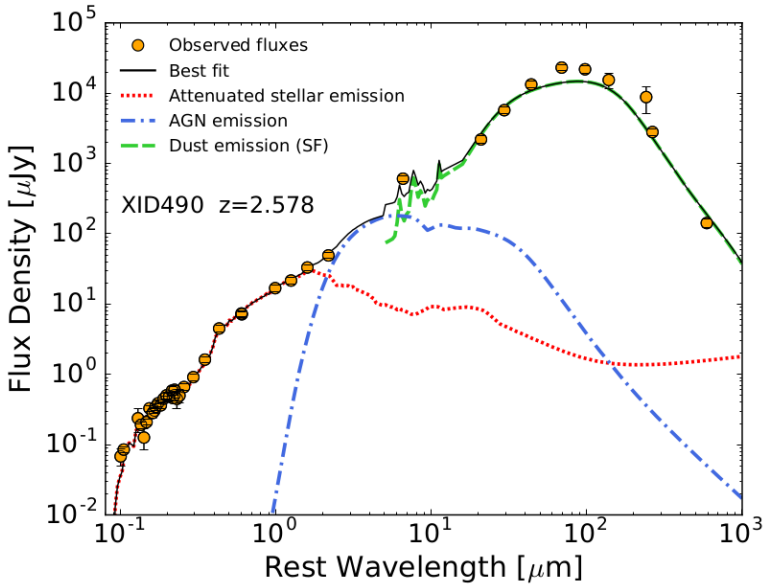

Figure B.2: IR SED of XID 490. The photometric data used for the SED fitting (yellow filled circles) were taken from the Rainbow Cosmological Surveys Database (https://rainbowx.fis.ucm.es/Rainbow_Database/Home.html). The data were modeled using the SED fitting code originally presented by Fritz et al. (2006) and improved by Feltre et al. (2012), that includes three components: stellar emission (modeled by means of SSPs) indicated by the red dotted line, the reprocessed emission of the dusty torus surrounding the AGN (blue dash–dotted line), and emission by the cold dust of the host galaxy, heated by starburst activity (green dashed line). The total fit is indicated by the black solid line. From Circosta et al. (in prep.).

Bibliography

Alexander, D. M., Bauer, F. E., Chapman, S. C., Smail, I., Blain, A. W., Brandt, W. N. and Ivison, R. J. (2005), 'The X-Ray Spectral Properties of SCUBA Galaxies', *ApJ* **632**, 736–750.

Antonucci, R. (1993), 'Unified models for active galactic nuclei and quasars', *ARA&A* **31**, 473–521.

Asayama, S., Biggs, A., De Gregorio, I., Dent, B., Di Francesco, J., Fomalont, E., Hales, A., Hibbard, J., Marconi, G., Kameno, S., Vila Vilaro, B., Villard, E. and F., S. (2017), *ALMA Cycle 5 Technical Handbook*, Vol. 1, ALMA Partnership.

Barger, A. J., Cowie, L. L., Sanders, D. B., Fulton, E., Taniguchi, Y., Sato, Y., Kawara, K. and Okuda, H. (1998), 'Submillimetre-wavelength detection of dusty star-forming galaxies at high redshift', *Nature* **394**, 248–251.

Barro, G., Faber, S. M., Pérez-González, P. G., Koo, D. C., Williams, C. C., Kocevski, D. D., Trump, J. R., Mozena, M., McGrath, E., van der Wel, A., Wuyts, S., Bell, E. F., Croton, D. J., Ceverino, D., Dekel, A., Ashby, M. L. N., Cheung, E., Ferguson, H. C., Fontana, A., Fang, J., Giavalisco, M., Grogin, N. A., Guo, Y., Hathi, N. P., Hopkins, P. F., Huang, K.-H., Koekemoer, A. M., Kartaltepe, J. S., Lee, K.-S., Newman, J. A., Porter, L. A., Primack, J. R., Ryan, R. E., Rosario, D., Somerville, R. S., Salvato, M. and Hsu, L.-T. (2013), 'CANDELS: The Progenitors of Compact Quiescent Galaxies at z ˜ 2', *ApJ* **765**, 104.

Barro, G., Faber, S. M., Pérez-González, P. G., Pacifici, C., Trump, J. R., Koo, D. C., Wuyts, S., Guo, Y., Bell, E., Dekel, A., Porter, L., Primack, J., Ferguson, H., Ashby, M. L. N., Caputi, K., Ceverino, D., Croton, D., Fazio, G. G., Giavalisco, M., Hsu, L., Kocevski, D., Koekemoer, A., Kurczynski, P., Kollipara, P., Lee, J., McIntosh, D. H., McGrath, E., Moody, C., Somerville, R., Papovich, C., Salvato, M., Santini, P., Tal, T., van der Wel, A., Williams, C. C., Willner, S. P. and Zolotov, A. (2014), 'CANDELS+3D-HST: Compact SFGs at z ˜ 2-3, the Progenitors of the First Quiescent Galaxies', *ApJ* **791**, 52.

Beckmann, V. and Shrader, C. R. (2012), *Active Galactic Nuclei*.

Bianchi, S., Maiolino, R. and Risaliti, G. (2012), 'AGN Obscuration and the Unified Model', *Advances in Astronomy* **2012**, 782030.

Blain, A. W., Smail, I., Ivison, R. J., Kneib, J.-P. and Frayer, D. T. (2002), 'Submillimeter galaxies', *Physics Reports* **369**, 111–176.

Bolatto, A. D., Wolfire, M. and Leroy, A. K. (2013), 'The CO-to-H_2 Conversion Factor', *ARAA* **51**, 207–268.

Bothwell, M. S., Smail, I., Chapman, S. C., Genzel, R., Ivison, R. J., Tacconi, L. J., Alaghband-Zadeh, S., Bertoldi, F., Blain, A. W., Casey, C. M., Cox, P., Greve, T. R., Lutz, D., Neri, R., Omont, A. and Swinbank, A. M. (2013), 'A survey of molecular gas in luminous sub-millimetre galaxies', *MNRAS* **429**, 3047–3067.

Briggs, D. S. (1995), 'American Astronomical Society Meeting Abstracts', *Bulletin of the American Astronomical Society* **27**, 1444.

Burtscher, L., Meisenheimer, K., Tristram, K. R. W., Jaffe, W., Hönig, S. F., Davies, R. I., Kishimoto, M., Pott, J.-U., Röttgering, H., Schartmann, M., Weigelt, G. and Wolf, S. (2013), 'A diversity of dusty AGN tori. Data release for the VLTI/MIDI AGN Large Program and first results for 23 galaxies', *A&A* **558**, A149.

Calura, F., Gilli, R., Vignali, C., Pozzi, F., Pipino, A. and Matteucci, F. (2014), 'The dust content of QSO hosts at high redshift', *MNRAS* **438**, 2765–2783.

Carilli, C. L. and Walter, F. (2013), 'Cool Gas in High-Redshift Galaxies', *ARAA* **51**, 105–161.

Cassata, P., Giavalisco, M., Guo, Y., Renzini, A., Ferguson, H., Koekemoer, A. M., Salimbeni, S., Scarlata, C., Grogin, N. A., Conselice, C. J., Dahlen, T., Lotz, J. M., Dickinson, M. and Lin, L. (2011), 'The Relative Abundance of Compact and Normal Massive Early-type Galaxies and Its Evolution from Redshift z = 2 to the Present', *ApJ* **743**, 96.

Chapman, S. C., Blain, A. W., Smail, I. and Ivison, R. J. (2005), 'A Redshift Survey of the Submillimeter Galaxy Population', *ApJ* **622**, 772–796.

Chen, C.-C., Smail, I., Swinbank, A. M., Simpson, J. M., Ma, C.-J., Alexander, D. M., Biggs, A. D., Brandt, W. N., Chapman, S. C., Coppin, K. E. K., Danielson, A. L. R., Dannerbauer, H., Edge, A. C., Greve, T. R., Ivison, R. J., Karim, A., Menten, K. M., Schinnerer, E., Walter, F., Wardlow, J. L., Weiß, A. and van der Werf, P. P. (2015), 'An ALMA Survey of Submillimeter Galaxies in the Extended Chandra Deep Field South: Near-infrared Morphologies and Stellar Sizes', *ApJ* **799**, 194.

Chiaberge, M., Capetti, A. and Celotti, A. (2000), 'The HST view of the FR I / FR II dichotomy', *A&A* **355**, 873–879.

Ciesla, L., Charmandaris, V., Georgakakis, A., Bernhard, E., Mitchell, P. D., Buat, V., Elbaz, D., LeFloc'h, E., Lacey, C. G., Magdis, G. E. and Xilouris, M. (2015), 'Constraining the properties of AGN host galaxies with spectral energy distribution modelling', *A&A* **576**, A10.

Cimatti, A., Cassata, P., Pozzetti, L., Kurk, J., Mignoli, M., Renzini, A., Daddi, E., Bolzonella, M., Brusa, M., Rodighiero, G., Dickinson, M., Franceschini, A., Zamorani, G., Berta, S., Rosati, P. and Halliday, C. (2008), 'GMASS ultradeep spectroscopy of galaxies at z ˜ 2. II. Superdense passive galaxies: how did they form and evolve?', *A&A* **482**, 21–42.

Circosta, C., Vignali, C., Gilli, R., Feltre, A. and F., V. (in prep.), 'Heavily obscured active galactic nuclei in the 7 Ms CDF–S: X–ray obscuration by the host galaxy', *A&A* .

Comastri, A., Ranalli, P., Iwasawa, K., Vignali, C., Gilli, R., Georgantopoulos, I., Barcons, X., Brandt, W. N., Brunner, H., Brusa, M., Cappelluti, N., Carrera, F. J., Civano, F., Fiore, F., Hasinger, G., Mainieri, V., Merloni, A., Nicastro, F., Paolillo, M., Puccetti, S., Rosati, P., Silverman, J. D., Tozzi, P., Zamorani, G., Balestra, I., Bauer, F. E., Luo, B. and Xue, Y. Q. (2011), 'The XMM Deep survey in the CDF-S. I. First results on heavily obscured AGN', *A&A* **526**, L9.

Condon, J. J. (1997), 'Errors in Elliptical Gaussian FITS', *pASP* **109**, 166–172.

Conley, A., Cooray, A., Vieira, J. D., González Solares, E. A., Kim, S., Aguirre, J. E., Amblard, A., Auld, R., Baker, A. J., Beelen, A., Blain, A., Blundell, R., Bock, J., Bradford, C. M., Bridge, C., Brisbin, D., Burgarella, D., Carpenter, J. M., Chanial, P., Chapin, E., Christopher, N., Clements, D. L., Cox, P., Djorgovski, S. G., Dowell, C. D., Eales, S., Earle, L., Ellsworth-Bowers, T. P., Farrah, D., Franceschini, A., Frayer, D., Fu, H., Gavazzi, R., Glenn, J., Griffin, M., Gurwell, M. A., Halpern, M., Ibar, E., Ivison, R. J., Jarvis, M., Kamenetzky, J., Krips, M., Levenson, L., Lupu, R., Mahabal, A., Maloney, P. D., Maraston, C., Marchetti, L., Marsden, G., Matsuhara, H., Mortier, A. M. J., Murphy, E., Naylor, B. J., Neri, R., Nguyen, H. T., Oliver, S. J., Omont, A., Page, M. J., Papageorgiou, A., Pearson, C. P., Pérez-Fournon, I., Pohlen, M., Rangwala, N., Rawlings, J. I., Raymond, G., Riechers, D., Rodighiero, G., Roseboom, I. G., Rowan-Robinson, M., Schulz, B., Scott, D., Scott, K., Serra, P., Seymour, N., Shupe, D. L., Smith, A. J., Symeonidis, M., Tugwell, K. E., Vaccari, M., Valiante, E., Valtchanov, I., Verma, A., Viero, M. P., Vigroux, L., Wang, L., Wiebe, D., Wright, G., Xu, C. K., Zeimann, G., Zemcov, M.

and Zmuidzinas, J. (2011), 'Discovery of a Multiply Lensed Submillimeter Galaxy in Early HerMES Herschel/SPIRE Data', *ApJl* **732**, L35.

Coppin, K. E. K., Chapman, S. C., Smail, I., Swinbank, A. M., Walter, F., Wardlow, J. L., Weiss, A., Alexander, D. M., Brandt, W. N., Dannerbauer, H., De Breuck, C., Dickinson, M., Dunlop, J. S., Edge, A. C., Emonts, B. H. C., Greve, T. R., Huynh, M., Ivison, R. J., Knudsen, K. K., Menten, K. M., Schinnerer, E. and van der Werf, P. P. (2010), 'Detection of molecular gas in a distant submillimetre galaxy at z = 4.76 with Australia Telescope Compact Array', *MNRAS* **407**, L103–L107.

Cowley, W. I., Lacey, C. G., Baugh, C. M. and Cole, S. (2015), 'Simulated observations of sub-millimetre galaxies: the impact of single-dish resolution and field variance', *MNRAS* **446**, 1784–1798.

Davé, R., Finlator, K., Oppenheimer, B. D., Fardal, M., Katz, N., Kereš, D. and Weinberg, D. H. (2010), 'The nature of submillimetre galaxies in cosmological hydrodynamic simulations', *MNRAS* **404**, 1355–1368.

De Breuck, C., Williams, R. J., Swinbank, M., Caselli, P., Coppin, K., Davis, T. A., Maiolino, R., Nagao, T., Smail, I., Walter, F., Weiß, A. and Zwaan, M. A. (2014), 'ALMA resolves turbulent, rotating [CII] emission in a young starburst galaxy at z = 4.8', *A&A* **565**, A59.

Di Matteo, T., Quataert, E., Allen, S. W., Narayan, R. and Fabian, A. C. (2000), 'Low-radiative-efficiency accretion in the nuclei of elliptical galaxies', *MNRAS* **311**, 507–521.

Draine, B. T. and Li, A. (2007), 'Infrared Emission from Interstellar Dust. IV. The Silicate-Graphite-PAH Model in the Post-Spitzer Era', *ApJ* **657**, 810–837.

Dunlop, J. S., McLure, R. J., Biggs, A. D., Geach, J. E., Michałowski, M. J., Ivison, R. J., Rujopakarn, W., van Kampen, E., Kirkpatrick, A., Pope, A., Scott, D., Swinbank, A. M., Targett, T. A., Aretxaga, I., Austermann, J. E., Best, P. N., Bruce, V. A., Chapin, E. L., Charlot, S., Cirasuolo, M., Coppin, K., Ellis, R. S., Finkelstein, S. L., Hayward, C. C., Hughes, D. H., Ibar, E., Jagannathan, P., Khochfar, S., Koprowski, M. P., Narayanan, D., Nyland, K., Papovich, C., Peacock, J. A., Rieke, G. H., Robertson, B., Vernstrom, T., Werf, P. P. v. d., Wilson, G. W. and Yun, M. (2017), 'A deep ALMA image of the Hubble Ultra Deep Field', *MNRAS* **466**, 861–883.

Dye, S., Furlanetto, C., Swinbank, A. M., Vlahakis, C., Nightingale, J. W., Dunne, L., Eales, S. A., Smail, I., Oteo, I., Hunter, T., Negrello, M., Dannerbauer, H., Ivison, R. J., Gavazzi, R., Cooray, A. and van der Werf, P. (2015), 'Revealing the complex nature of the strong gravitationally lensed

system H-ATLAS J090311.6+003906 using ALMA', *MNRAS* **452**, 2258–2268.

Fabian, A. C., Lohfink, A., Kara, E., Parker, M. L., Vasudevan, R. and Reynolds, C. S. (2015), 'Properties of AGN coronae in the NuSTAR era', *MNRAS* **451**, 4375–4383.

Fanaroff, B. L. and Riley, J. M. (1974), 'The morphology of extragalactic radio sources of high and low luminosity', *MNRAS* **167**, 31P–36P.

Feltre, A., Hatziminaoglou, E., Fritz, J. and Franceschini, A. (2012), 'Smooth and clumpy dust distributions in AGN: a direct comparison of two commonly explored infrared emission models', *MNRAS* **426**, 120–127.

Fritz, J., Franceschini, A. and Hatziminaoglou, E. (2006), 'Revisiting the infrared spectra of active galactic nuclei with a new torus emission model', *MNRAS* **366**, 767–786.

Fu, H., Jullo, E., Cooray, A., Bussmann, R. S., Ivison, R. J., Pérez-Fournon, I., Djorgovski, S. G., Scoville, N., Yan, L., Riechers, D. A., Aguirre, J., Auld, R., Baes, M., Baker, A. J., Bradford, M., Cava, A., Clements, D. L., Dannerbauer, H., Dariush, A., De Zotti, G., Dole, H., Dunne, L., Dye, S., Eales, S., Frayer, D., Gavazzi, R., Gurwell, M., Harris, A. I., Herranz, D., Hopwood, R., Hoyos, C., Ibar, E., Jarvis, M. J., Kim, S., Leeuw, L., Lupu, R., Maddox, S., Martínez-Navajas, P., Michałowski, M. J., Negrello, M., Omont, A., Rosenman, M., Scott, D., Serjeant, S., Smail, I., Swinbank, A. M., Valiante, E., Verma, A., Vieira, J., Wardlow, J. L. and van der Werf, P. (2012), 'A Comprehensive View of a Strongly Lensed Planck-Associated Submillimeter Galaxy', *ApJ* **753**, 134.

Gallagher, S. C., Abado, M. M., Everett, J. E., Keating, S. and Deo, R. P. (2013), 'Why a Windy Torus?', *ArXiv e-prints* .

Ghisellini, G. (2016), 'The Blazar Sequence 2.0', *Galaxies* **4**, 36.

Gilli, R., Comastri, A. and Hasinger, G. (2007), 'The synthesis of the cosmic X-ray background in the Chandra and XMM-Newton era', *A&A* **463**, 79–96.

Gilli, R., Norman, C., Vignali, C., Vanzella, E., Calura, F., Pozzi, F., Massardi, M., Mignano, A., Casasola, V., Daddi, E., Elbaz, D., Dickinson, M., Iwasawa, K., Maiolino, R., Brusa, M., Vito, F., Fritz, J., Feltre, A., Cresci, G., Mignoli, M., Comastri, A. and Zamorani, G. (2014), 'ALMA reveals a warm and compact starburst around a heavily obscured supermassive black hole at z = 4.75', *A&A* **562**, A67.

Gruppioni, C., Pozzi, F., Zamorani, G. and Vignali, C. (2011), 'Modelling galaxy and AGN evolution in the infrared: black hole accretion versus star formation activity', *MNRAS* **416**, 70–86.

Haas, M. (2003), Luminous dust emission in active galaxies as seen by ISO, *in* C. Gry, S. Peschke, J. Matagne, P. Garcia-Lario, R. Lorente and A. Salama, eds, 'Exploiting the ISO Data Archive. Infrared Astronomy in the Internet Age', Vol. 511 of *ESA Special Publication*, p. 257.

Hainline, L. J., Blain, A. W., Smail, I., Alexander, D. M., Armus, L., Chapman, S. C. and Ivison, R. J. (2011), 'The Stellar Mass Content of Submillimeter-selected Galaxies', *ApJ* **740**, 96.

Harrison, C. (2014), Observational constraints on the influence of active galactic nuclei on the evolution of galaxies, PhD thesis, Durham University.

Häussler, B., McIntosh, D. H., Barden, M., Bell, E. F., Rix, H.-W., Borch, A., Beckwith, S. V. W., Caldwell, J. A. R., Heymans, C., Jahnke, K., Jogee, S., Koposov, S. E., Meisenheimer, K., Sánchez, S. F., Somerville, R. S., Wisotzki, L. and Wolf, C. (2007), 'GEMS: Galaxy Fitting Catalogs and Testing Parametric Galaxy Fitting Codes: GALFIT and GIM2D', *ApJs* **172**, 615–633.

Hayward, C. C., Kereš, D., Jonsson, P., Narayanan, D., Cox, T. J. and Hernquist, L. (2011), 'What Does a Submillimeter Galaxy Selection Actually Select? The Dependence of Submillimeter Flux Density on Star Formation Rate and Dust Mass', *ApJ* **743**, 159.

Hazard, C., Mackey, M. B. and Shimmins, A. J. (1963), 'Investigation of the Radio Source 3C 273 By The Method of Lunar Occultations', *Nature* **197**, 1037–1039.

Hickox, R. C., Wardlow, J. L., Smail, I., Myers, A. D., Alexander, D. M., Swinbank, A. M., Danielson, A. L. R., Stott, J. P., Chapman, S. C., Coppin, K. E. K., Dunlop, J. S., Gawiser, E., Lutz, D., van der Werf, P. and Weiß, A. (2012), 'The LABOCA survey of the Extended Chandra Deep Field-South: clustering of submillimetre galaxies', *MNRAS* **421**, 284–295.

Hodge, J. A., Carilli, C. L., Walter, F., de Blok, W. J. G., Riechers, D., Daddi, E. and Lentati, L. (2012), 'Evidence for a Clumpy, Rotating Gas Disk in a Submillimeter Galaxy at z = 4', *ApJ* **760**, 11.

Hodge, J. A., Karim, A., Smail, I., Swinbank, A. M., Walter, F., Biggs, A. D., Ivison, R. J., Weiss, A., Alexander, D. M., Bertoldi, F., Brandt, W. N., Chapman, S. C., Coppin, K. E. K., Cox, P., Danielson, A. L. R., Dannerbauer, H., De Breuck, C., Decarli, R., Edge, A. C., Greve, T. R.,

Knudsen, K. K., Menten, K. M., Rix, H.-W., Schinnerer, E., Simpson, J. M., Wardlow, J. L. and van der Werf, P. (2013), 'An ALMA Survey of Submillimeter Galaxies in the Extended Chandra Deep Field South: Source Catalog and Multiplicity', *ApJ* **768**, 91.

Hodge, J. A., Swinbank, A. M., Simpson, J. M., Smail, I., Walter, F., Alexander, D. M., Bertoldi, F., Biggs, A. D., Brandt, W. N., Chapman, S. C., Chen, C. C., Coppin, K. E. K., Cox, P., Dannerbauer, H., Edge, A. C., Greve, T. R., Ivison, R. J., Karim, A., Knudsen, K. K., Menten, K. M., Rix, H.-W., Schinnerer, E., Wardlow, J. L., Weiss, A. and van der Werf, P. (2016), 'Kiloparsec-scale Dust Disks in High-redshift Luminous Submillimeter Galaxies', *ApJ* **833**, 103.

Hopkins, A. M. and Beacom, J. F. (2006), 'On the Normalization of the Cosmic Star Formation History', *ApJ* **651**, 142–154.

Hopkins, P. F. (2008), A physical model for the fueling and evolution of quasars in galaxy mergers, PhD thesis, Harvard University.

Hughes, D. H., Serjeant, S., Dunlop, J., Rowan-Robinson, M., Blain, A., Mann, R. G., Ivison, R., Peacock, J., Efstathiou, A., Gear, W., Oliver, S., Lawrence, A., Longair, M., Goldschmidt, P. and Jenness, T. (1998), 'High-redshift star formation in the Hubble Deep Field revealed by a submillimetre-wavelength survey', *Nature* **394**, 241–247.

Ichimaru, S. (1977), 'Bimodal behavior of accretion disks - Theory and application to Cygnus X-1 transitions', *Apj)* **214**, 840–855.

Ikarashi, S., Ivison, R. J., Caputi, K. I., Aretxaga, I., Dunlop, J. S., Hatsukade, B., Hughes, D. H., Iono, D., Izumi, T., Kawabe, R., Kohno, K., Lagos, C. D. P., Motohara, K., Nakanishi, K., Ohta, K., Tamura, Y., Umehata, H., Wilson, G. W., Yabe, K. and Yun, M. S. (2015), 'Compact Starbursts in z $\sim$ 3-6 Submillimeter Galaxies Revealed by ALMA', *ApJ* **810**, 133.

Ivison, R. J., Swinbank, A. M., Smail, I., Harris, A. I., Bussmann, R. S., Cooray, A., Cox, P., Fu, H., Kovács, A., Krips, M., Narayanan, D., Negrello, M., Neri, R., Peñarrubia, J., Richard, J., Riechers, D. A., Rowlands, K., Staguhn, J. G., Targett, T. A., Amber, S., Baker, A. J., Bourne, N., Bertoldi, F., Bremer, M., Calanog, J. A., Clements, D. L., Dannerbauer, H., Dariush, A., De Zotti, G., Dunne, L., Eales, S. A., Farrah, D., Fleuren, S., Franceschini, A., Geach, J. E., George, R. D., Helly, J. C., Hopwood, R., Ibar, E., Jarvis, M. J., Kneib, J.-P., Maddox, S., Omont, A., Scott, D., Serjeant, S., Smith, M. W. L., Thompson, M. A., Valiante, E., Valtchanov, I., Vieira, J. and van der Werf, P. (2013), 'Herschel-ATLAS: A Binary HyLIRG Pinpointing a Cluster of Starbursting Protoellipticals', *ApJ* **772**, 137.

Jaffe, D. T., Marsh, J. P. and Tokunaga, A. (2004), Near-IR Excesses and Spectral Energy Distributions for Class II YSO's in Ophiuchus, *in* 'American Astronomical Society Meeting Abstracts', Vol. 36 of *Bulletin of the American Astronomical Society*, p. 1568.

Karim, A., Swinbank, A. M., Hodge, J. A., Smail, I. R., Walter, F., Biggs, A. D., Simpson, J. M., Danielson, A. L. R., Alexander, D. M., Bertoldi, F., de Breuck, C., Chapman, S. C., Coppin, K. E. K., Dannerbauer, H., Edge, A. C., Greve, T. R., Ivison, R. J., Knudsen, K. K., Menten, K. M., Schinnerer, E., Wardlow, J. L., Weiß, A. and van der Werf, P. (2013), 'An ALMA survey of submillimetre galaxies in the Extended Chandra Deep Field South: high-resolution 870 μm source counts', *MNRAS* **432**, 2–9.

Kellermann, K. I., Sramek, R., Schmidt, M., Shaffer, D. B. and Green, R. (1989), 'VLA observations of objects in the Palomar Bright Quasar Survey', *AJ* **98**, 1195–1207.

Lacey, C. G., Baugh, C. M., Frenk, C. S., Benson, A. J., Bower, R. G., Cole, S., Gonzalez-Perez, V., Helly, J. C., Lagos, C. D. P. and Mitchell, P. D. (2016), 'A unified multiwavelength model of galaxy formation', *MNRAS* **462**, 3854–3911.

Lapi, A., Pantoni, L., Zanisi, L., Shi, J., Mancuso, C., Massardi, M., Shankar, F., Bressan, A. and Danese, L. (2018), 'The Dramatic Size and Kinematic Evolution of Massive Early-type Galaxies', *ApJ* **857**, 22.

Lapi, A., Raimundo, S., Aversa, R., Cai, Z.-Y., Negrello, M., Celotti, A., De Zotti, G. and Danese, L. (2014), 'The Coevolution of Supermassive Black Holes and Massive Galaxies at High Redshift', *ApJ* **782**, 69.

Luo, B., Brandt, W. N., Xue, Y. Q., Lehmer, B., Alexander, D. M., Bauer, F. E., Vito, F., Yang, G., Basu-Zych, A. R., Comastri, A., Gilli, R., Gu, Q.-S., Hornschemeier, A. E., Koekemoer, A., Liu, T., Mainieri, V., Paolillo, M., Ranalli, P., Rosati, P., Schneider, D. P., Shemmer, O., Smail, I., Sun, M., Tozzi, P., Vignali, C. and Wang, J.-X. (2017), 'The Chandra Deep Field-South Survey: 7 Ms Source Catalogs', *ApJs* **228**, 2.

Lyons, L. (1991), *A Practical Guide to Data Analysis for Physical Science Students*.

Magnelli, B., Lutz, D., Santini, P., Saintonge, A., Berta, S., Albrecht, M., Altieri, B., Andreani, P., Aussel, H., Bertoldi, F., Béthermin, M., Bongiovanni, A., Capak, P., Chapman, S., Cepa, J., Cimatti, A., Cooray, A., Daddi, E., Danielson, A. L. R., Dannerbauer, H., Dunlop, J. S., Elbaz, D., Farrah, D., Förster Schreiber, N. M., Genzel, R., Hwang, H. S., Ibar, E., Ivison, R. J., Le Floc'h, E., Magdis, G., Maiolino, R., Nordon, R., Oliver, S. J., Pérez García, A., Poglitsch, A., Popesso, P., Pozzi, F., Riguccini, L.,

Rodighiero, G., Rosario, D., Roseboom, I., Salvato, M., Sanchez-Portal, M., Scott, D., Smail, I., Sturm, E., Swinbank, A. M., Tacconi, L. J., Valtchanov, I., Wang, L. and Wuyts, S. (2012), 'A Herschel view of the far-infrared properties of submillimetre galaxies', *A&A* **539**, A155.

Magorrian, J., Tremaine, S., Richstone, D., Bender, R., Bower, G., Dressler, A., Faber, S. M., Gebhardt, K., Green, R., Grillmair, C., Kormendy, J. and Lauer, T. (1998), 'The Demography of Massive Dark Objects in Galaxy Centers', *AJ* **115**, 2285–2305.

Mainieri, V., Rigopoulou, D., Lehmann, I., Scott, S., Matute, I., Almaini, O., Tozzi, P., Hasinger, G. and Dunlop, J. S. (2005), 'Submillimetre detection of a high-redshift type 2 QSO', *MNRAS* **356**, 1571–1575.

Massardi, M., Enia, A. F. M., Negrello, M., Mancuso, C., Lapi, A., Vignali, C., Gilli, R., Burkutean, S., Danese, L. and Zotti, G. D. (2018), 'Chandra and ALMA observations of the nuclear activity in two strongly lensed star-forming galaxies', *A&A* **610**, A53.

Mathis, J. S., Rumpl, W. and Nordsieck, K. H. (1977), 'The size distribution of interstellar grains', *ApJ* **217**, 425–433.

Michałowski, M., Hjorth, J. and Watson, D. (2010), 'Cosmic evolution of submillimeter galaxies and their contribution to stellar mass assembly', *A&A* **514**, A67.

Michałowski, M. J., Dunlop, J. S., Cirasuolo, M., Hjorth, J., Hayward, C. C. and Watson, D. (2012), 'The stellar masses and specific star-formation rates of submillimetre galaxies', *A&A* **541**, A85.

Murphy, K. D. and Yaqoob, T. (2009), 'An X-ray spectral model for Compton-thick toroidal reprocessors', *MNRAS* **397**, 1549–1562.

Nagao, T., Maiolino, R., De Breuck, C., Caselli, P., Hatsukade, B. and Saigo, K. (2012), 'ALMA reveals a chemically evolved submillimeter galaxy at z = 4.76', *A&A* **542**, L34.

Narayanan, D., Turk, M., Feldmann, R., Robitaille, T., Hopkins, P., Thompson, R., Hayward, C., Ball, D., Faucher-Giguère, C.-A. and Kereš, D. (2015), 'The formation of submillimetre-bright galaxies from gas infall over a billion years', *Nature* **525**, 496–499.

Netzer, H. (2013), *The Physics and Evolution of Active Galactic Nuclei*.

Norman, C., Hasinger, G., Giacconi, R., Gilli, R., Kewley, L., Nonino, M., Rosati, P., Szokoly, G., Tozzi, P., Wang, J., Zheng, W., Zirm, A., Bergeron, J., Gilmozzi, R., Grogin, N., Koekemoer, A. and Schreier, E. (2002), 'A Classic Type 2 QSO', *ApJ* **571**, 218–225.

Padovani, P., Alexander, D. M., Assef, R. J., De Marco, B., Giommi, P., Hickox, R. C., Richards, G. T., Smolčić, V., Hatziminaoglou, E., Mainieri, V. and Salvato, M. (2017), 'Active galactic nuclei: what's in a name?', *A&AR* **25**, 2.

Papadopoulos, P. P., van der Werf, P., Xilouris, E., Isaak, K. G. and Gao, Y. (2012), 'The Molecular Gas in Luminous Infrared Galaxies. II. Extreme Physical Conditions and Their Effects on the X $_{co}$ Factor', *ApJ* **751**, 10.

Perna, M., Sargent, M. T., Brusa, M., Daddi, E., Feruglio, C., Cresci, G., Lanzuisi, G., Lusso, E., Comastri, A., Coogan, R. T., D'Amato, Q., Gilli, R., Piconcelli, E. and Vignali, C. (2018), 'The molecular gas content in obscured AGN at z $>$ 1', *ArXiv e-prints* .

Peterson, B. M. (1997), *An Introduction to Active Galactic Nuclei.*

Pier, E. A. and Krolik, J. H. (1992), 'Infrared spectra of obscuring dust tori around active galactic nuclei. I - Calculational method and basic trends', *ApJ* **401**, 99–109.

Pier, E. A. and Krolik, J. H. (1993), 'Infrared Spectra of Obscuring Dust Tori around Active Galactic Nuclei. II. Comparison with Observations', *ApJ* **418**, 673.

Rangwala, N., Maloney, P. R., Glenn, J., Wilson, C. D., Rykala, A., Isaak, K., Baes, M., Bendo, G. J., Boselli, A., Bradford, C. M., Clements, D. L., Cooray, A., Fulton, T., Imhof, P., Kamenetzky, J., Madden, S. C., Mentuch, E., Sacchi, N., Sauvage, M., Schirm, M. R. P., Smith, M. W. L., Spinoglio, L. and Wolfire, M. (2011), 'Observations of Arp 220 Using Herschel-SPIRE: An Unprecedented View of the Molecular Gas in an Extreme Star Formation Environment', *ApJ* **743**, 94.

Rigopoulou, D., Mainieri, V., Almaini, O., Alonso-Herrero, A., Huang, J.-S., Hasinger, G., Rieke, G., Dunlop, J. and Lehmann, I. (2009), 'Spectral energy distributions of type 2 quasi-stellar objects: obscured star formation at high redshifts', *MNRAS* **400**, 1199–1207.

Risaliti, G. (2008), Unveiling the structure of the circumnuclaear medium of AGNs through time-resolved X-ray spectroscopy, *in* S. K. Chakrabarti and A. S. Majumdar, eds, 'American Institute of Physics Conference Series', Vol. 1053 of *American Institute of Physics Conference Series*, pp. 59–62.

Risaliti, G. and Elvis, M. (2004), A Panchromatic View of AGN, *in* A. J. Barger, ed., 'Supermassive Black Holes in the Distant Universe', Vol. 308 of *Astrophysics and Space Science Library*, p. 187.

Rosario, D. J., Santini, P., Lutz, D., Shao, L., Maiolino, R., Alexander, D. M., Altieri, B., Andreani, P., Aussel, H., Bauer, F. E., Berta, S., Bongiovanni, A., Brandt, W. N., Brusa, M., Cepa, J., Cimatti, A., Cox, T. J., Daddi, E., Elbaz, D., Fontana, A., Förster Schreiber, N. M., Genzel, R., Grazian, A., Le Floch, E., Magnelli, B., Mainieri, V., Netzer, H., Nordon, R., Pérez Garcia, I., Poglitsch, A., Popesso, P., Pozzi, F., Riguccini, L., Rodighiero, G., Salvato, M., Sanchez-Portal, M., Sturm, E., Tacconi, L. J., Valtchanov, I. and Wuyts, S. (2012), 'The mean star formation rate of X-ray selected active galaxies and its evolution from z ˜ 2.5: results from PEP-Herschel', *A&A* **545**, A45.

Sanders, D. B., Soifer, B. T., Elias, J. H., Madore, B. F., Matthews, K., Neugebauer, G. and Scoville, N. Z. (1988), 'Ultraluminous infrared galaxies and the origin of quasars', *ApJ* **325**, 74–91.

Schartmann, M., Meisenheimer, K., Klahr, H., Camenzind, M., Wolf, S. and Henning, T. (2009), 'The effect of stellar feedback on the formation and evolution of gas and dust tori in AGN', *MNRAS* **393**, 759–773.

Scoville, N., Sheth, K., Aussel, H., Vanden Bout, P., Capak, P., Bongiorno, A., Casey, C. M., Murchikova, L., Koda, J., Álvarez-Márquez, J., Lee, N., Laigle, C., McCracken, H. J., Ilbert, O., Pope, A., Sanders, D., Chu, J., Toft, S., Ivison, R. J. and Manohar, S. (2016), 'ISM Masses and the Star formation Law at Z = 1 to 6: ALMA Observations of Dust Continuum in 145 Galaxies in the COSMOS Survey Field', *Apj* **820**, 83.

Seyfert, C. K. (1943), 'Nuclear Emission in Spiral Nebulae.', *ApJ* **97**, 28.

Shakura, N. I. and Sunyaev, R. A. (1973), 'Black holes in binary systems. Observational appearance.', *A&A* **24**, 337–355.

Simpson, J. M., Swinbank, A. M., Smail, I., Alexander, D. M., Brandt, W. N., Bertoldi, F., de Breuck, C., Chapman, S. C., Coppin, K. E. K., da Cunha, E., Danielson, A. L. R., Dannerbauer, H., Greve, T. R., Hodge, J. A., Ivison, R. J., Karim, A., Knudsen, K. K., Poggianti, B. M., Schinnerer, E., Thomson, A. P., Walter, F., Wardlow, J. L., Weiß, A. and van der Werf, P. P. (2014), 'An ALMA Survey of Submillimeter Galaxies in the Extended Chandra Deep Field South: The Redshift Distribution and Evolution of Submillimeter Galaxies', *ApJ* **788**, 125.

Smail, I., Chapman, S. C., Blain, A. W. and Ivison, R. J. (2004), 'The Rest-Frame Optical Properties of SCUBA Galaxies', *ApJ* **616**, 71–85.

Smail, I., Ivison, R. J. and Blain, A. W. (1997), 'A Deep Sub-millimeter Survey of Lensing Clusters: A New Window on Galaxy Formation and Evolution', *ApJl* **490**, L5–L8.

Solomon, P. M., Downes, D. and Radford, S. J. E. (1992), *ApJ* **398**, L29–L32.

Solomon, P. M., Downes, D., Radford, S. J. E. and Barrett, J. W. (1997), 'The Molecular Interstellar Medium in Ultraluminous Infrared Galaxies', *ApJ* **478**, 144–161.

Stalevski, M., Fritz, J., Baes, M., Nakos, T. and Popović, L. Č. (2012), '3D radiative transfer modelling of the dusty tori around active galactic nuclei as a clumpy two-phase medium', *MNRAS* **420**, 2756–2772.

Swinbank, A. M., Simpson, J. M., Smail, I., Harrison, C. M., Hodge, J. A., Karim, A., Walter, F., Alexander, D. M., Brandt, W. N., de Breuck, C., da Cunha, E., Chapman, S. C., Coppin, K. E. K., Danielson, A. L. R., Dannerbauer, H., Decarli, R., Greve, T. R., Ivison, R. J., Knudsen, K. K., Lagos, C. D. P., Schinnerer, E., Thomson, A. P., Wardlow, J. L., Weiß, A. and van der Werf, P. (2014), 'An ALMA survey of sub-millimetre Galaxies in the Extended Chandra Deep Field South: the far-infrared properties of SMGs', *MNRAS* **438**, 1267–1287.

Swinbank, A. M., Smail, I., Chapman, S. C., Borys, C., Alexander, D. M., Blain, A. W., Conselice, C. J., Hainline, L. J. and Ivison, R. J. (2010), 'A Hubble Space Telescope NICMOS and ACS morphological study of z $\sim$ 2 submillimetre galaxies', *MNRAS* **405**, 234–244.

Szokoly, G. P., Bergeron, J., Hasinger, G., Lehmann, I., Kewley, L., Mainieri, V., Nonino, M., Rosati, P., Giacconi, R., Gilli, R., Gilmozzi, R., Norman, C., Romaniello, M., Schreier, E., Tozzi, P., Wang, J. X., Zheng, W. and Zirm, A. (2004), 'The Chandra Deep Field-South: Optical Spectroscopy. I.', *ApJs* **155**, 271–349.

Tacconi, L. J., Genzel, R., Smail, I., Neri, R., Chapman, S. C., Ivison, R. J., Blain, A., Cox, P., Omont, A., Bertoldi, F., Greve, T., Förster Schreiber, N. M., Genel, S., Lutz, D., Swinbank, A. M., Shapley, A. E., Erb, D. K., Cimatti, A., Daddi, E. and Baker, A. J. (2008), 'Submillimeter Galaxies at z ˜ 2: Evidence for Major Mergers and Constraints on Lifetimes, IMF, and CO-H_2 Conversion Factor', *ApJ* **680**, 246–262.

Ueda, Y., Hatsukade, B., Kohno, K., Yamaguchi, Y., Tamura, Y., Umehata, H., Akiyama, M., Ao, Y., Aretxaga, I., Caputi, K., Dunlop, J. S., Espada, D., Fujimoto, S., Hayatsu, N. H., Imanishi, M., Inoue, A. K., Ivison, R. J., Kodama, T., Lee, M. M., Matsuoka, K., Miyaji, T., Morokuma-Matsui, K., Nagao, T., Nakanishi, K., Nyland, K., Ohta, K., Ouchi, M., Rujopakarn, W., Saito, T., Tadaki, K., Tanaka, I., Taniguchi, Y., Wang, T., Wang, W.-H., Yoshimura, Y. and Yun, M. S. (2018), 'ALMA 26 arcmin^2 Survey of GOODS-S at One-millimeter (ASAGAO): X-Ray AGN Properties of Millimeter-selected Galaxies', *ApJ* **853**, 24.

van der Wel, A., Franx, M., van Dokkum, P. G., Skelton, R. E., Momcheva, I. G., Whitaker, K. E., Brammer, G. B., Bell, E. F., Rix, H.-W., Wuyts, S., Ferguson, H. C., Holden, B. P., Barro, G., Koekemoer, A. M., Chang, Y.-Y., McGrath, E. J., Häussler, B., Dekel, A., Behroozi, P., Fumagalli, M., Leja, J., Lundgren, B. F., Maseda, M. V., Nelson, E. J., Wake, D. A., Patel, S. G., Labbé, I., Faber, S. M., Grogin, N. A. and Kocevski, D. D. (2014), '3D-HST+CANDELS: The Evolution of the Galaxy Size-Mass Distribution since z = 3', *ApJ* **788**, 28.

Vito, F., Brandt, W. N., Yang, G., Gilli, R., Luo, B., Vignali, C., Xue, Y. Q., Comastri, A., Koekemoer, A. M., Lehmer, B. D., Liu, T., Paolillo, M., Ranalli, P., Schneider, D. P., Shemmer, O., Volonteri, M. and Wang, J. (2018), 'High-redshift AGN in the Chandra Deep Fields: the obscured fraction and space density of the sub-L_* population', *MNRAS* **473**, 2378–2406.

Vito, F., Gilli, R., Vignali, C., Brandt, W. N., Comastri, A., Yang, G., Lehmer, B. D., Luo, B., Basu-Zych, A., Bauer, F. E., Cappelluti, N., Koekemoer, A., Mainieri, V., Paolillo, M., Ranalli, P., Shemmer, O., Trump, J., Wang, J. X. and Xue, Y. Q. (2016), 'The deepest X-ray view of high-redshift galaxies: constraints on low-rate black hole accretion', *MNRAS* **463**, 348–374.

Vito, F., Gilli, R., Vignali, C., Comastri, A., Brusa, M., Cappelluti, N. and Iwasawa, K. (2014), 'The hard X-ray luminosity function of high-redshift ($3 < z < 5$) active galactic nuclei', *MNRAS* **445**, 3557–3574.

Vito, F., Vignali, C., Gilli, R., Comastri, A., Iwasawa, K., Brandt, W. N., Alexander, D. M., Brusa, M., Lehmer, B., Bauer, F. E., Schneider, D. P., Xue, Y. Q. and Luo, B. (2013), 'The high-redshift ($z > 3$) active galactic nucleus population in the 4-Ms Chandra Deep Field-South', *MNRAS* **428**, 354–369.

Walter, F., Carilli, C., Bertoldi, F., Menten, K., Cox, P., Lo, K. Y., Fan, X. and Strauss, M. A. (2004), 'Resolved Molecular Gas in a Quasar Host Galaxy at Redshift z=6.42', *ApJl* **615**, L17–L20.

Wang, R., Wagg, J., Carilli, C. L., Walter, F., Lentati, L., Fan, X., Riechers, D. A., Bertoldi, F., Narayanan, D., Strauss, M. A., Cox, P., Omont, A., Menten, K. M., Knudsen, K. K., Neri, R. and Jiang, L. (2013), 'Star Formation and Gas Kinematics of Quasar Host Galaxies at z ˜ 6: New Insights from ALMA', *ApJ* **773**, 44.

Wardlow, J. L., Simpson, J. M., Smail, I., Swinbank, A. M., Blain, A. W., Brandt, W. N., Chapman, S. C., Chen, C.-C., Cooke, E. A., Dannerbauer, H., Gullberg, B., Hodge, J. A., Ivison, R. J., Knudsen, K. K., Scott, D.,

Thomson, A. P., Weiß, A. and van der Werf, P. P. (2018), 'An ALMA survey of CO in submillimetre galaxies: companions, triggering, and the environment in blended sources', *MNRAS* **479**, 3879–3891.

Wardlow, J. L., Smail, I., Coppin, K. E. K., Alexander, D. M., Brandt, W. N., Danielson, A. L. R., Luo, B., Swinbank, A. M., Walter, F., Weiß, A., Xue, Y. Q., Zibetti, S., Bertoldi, F., Biggs, A. D., Chapman, S. C., Dannerbauer, H., Dunlop, J. S., Gawiser, E., Ivison, R. J., Knudsen, K. K., Kovács, A., Lacey, C. G., Menten, K. M., Padilla, N., Rix, H.-W. and van der Werf, P. P. (2011), 'The LABOCA survey of the Extended Chandra Deep Field-South: a photometric redshift survey of submillimetre galaxies', *MNRAS* **415**, 1479–1508.

Weiß, A., Downes, D., Walter, F. and Henkel, C. (2007), CO Line SEDs of High-Redshift QSOs and Submm Galaxies, *in* A. J. Baker, J. Glenn, A. I. Harris, J. G. Mangum and M. S. Yun, eds, 'From Z-Machines to ALMA: (Sub)Millimeter Spectroscopy of Galaxies', Vol. 375 of *Astronomical Society of the Pacific Conference Series*, p. 25.

Wiklind, T., Conselice, C. J., Dahlen, T., Dickinson, M. E., Ferguson, H. C., Grogin, N. A., Guo, Y., Koekemoer, A. M., Mobasher, B., Mortlock, A., Fontana, A., Davé, R., Yan, H., Acquaviva, V., Ashby, M. L. N., Barro, G., Caputi, K. I., Castellano, M., Dekel, A., Donley, J. L., Fazio, G. G., Giavalisco, M., Grazian, A., Hathi, N. P., Kurczynski, P., Lu, Y., McGrath, E. J., de Mello, D. F., Peth, M., Safarzadeh, M., Stefanon, M. and Targett, T. (2014), 'Properties of Submillimeter Galaxies in the CANDELS GOODS-South Field', *ApJ* **785**, 111.

Wright, E. L. (2006), 'A Cosmology Calculator for the World Wide Web', *PASP* **118**, 1711–1715.

Xue, L., Sądowski, A., Abramowicz, M. A. and Lu, J.-F. (2011), 'Studies of Thermally Unstable Accretion Disks Around Black Holes with Adaptive Pseudospectral Domain Decomposition Method. II. Limit-cycle Behavior in Accretion Disks around Kerr Black Holes', *ApJs* **195**, 7.

Zavala, J. A., Aretxaga, I. and Hughes, D. H. (2014), 'The redshift distribution of submillimetre galaxies at different wavelengths', *MNRAS* **443**, 2384–2390.

Zubovas, K., Nayakshin, S., King, A. and Wilkinson, M. (2013), 'AGN outflows trigger starbursts in gas-rich galaxies', *MNRAS* **433**, 3079–3090.